



Universidade de Aveiro

2020

Sheila de Oliveira
Ferreira

Caracterização elétrica e biológica de dispositivos eletromecânicos de PLLA-aço inoxidável 316L para engenharia de tecido ósseo.

Electrical and biological characterization of PLLA-316L stainless steel electromechanical devices for bone tissue engineering.



Universidade de Aveiro
2020

Sheila de Oliveira
Ferreira

Caracterização elétrica e biológica de dispositivos eletromecânicos de PLLA-aço inoxidável 316L para engenharia de tecido ósseo.

Electrical and biological characterization of PLLA-316L stainless steel electromechanical devices for bone tissue engineering.

Dissertação apresentada à Universidade de Aveiro para cumprimento dos requisitos necessários à obtenção do grau de Mestre em Engenharia de Materiais, realizada sob a orientação científica da Profa. Dra. Maria Helena Figueira Vaz Fernandes, Professora Associada do Departamento de Engenharia de Materiais e Cerâmica da Universidade de Aveiro.

Dissertation presented to the University of Aveiro to fulfil the necessary requirements for the awarding of the Master's degree in Materials Engineer, carried out under the supervision of Prof. Dr. Maria Helena Figueira Vaz Fernandes, Associate Professor in the Department of Materials and Ceramics Engineering of the University of Aveiro.

“Ser abençoado é poder colher bons frutos da própria plantação.” – Ferreira, S. O.

Júri

Presidente	Professor Doutor João André da Costa Tedim Professor Auxiliar em Regime Laboral Universidade de Aveiro
Arguente Principal	Doutora Natália Braz Barroca Investigadora Doutorada (nível 1) Universidade de Aveiro
Orientadora	Professora Doutora Maria Helena Figueira Vaz Fernandes Professora Associada Universidade de Aveiro

Agradecimentos

Agradeço à Profa. Dra. Maria Helena Fernandes, à Profa. Dra. Paula Vilarinho e ao Dr. Maxim Ivanov por todo conhecimento científico e apoio ao longo desse trabalho.

A todos os integrantes do Electroceramics Group pela disponibilidade em ajudar e acolhimento. Sobretudo, à Adriana, Anna, Camila e Tatiana.

A toda equipa do DEMaC e demais colaboradores da Universidade de Aveiro pelo serviço técnico e académico. A equipa do ICBAS pela realização dos testes de citocompatibilidade. Em especial, à Profa. Dra. Ana Colette e à mestre Mariana Branquinho.

Aos amigos pelo incentivo e por tornaram a minha trajetória mais prazerosa. Aos meus pais, Damiana e Carlos, pelo cuidado e educação durante toda a minha vida. Aos meus sogros, Rosario e Francisco, pelo apoio durante minha formação. Ao meu marido, Gonçalo, pelo companheirismo. Essencialmente, a Deus por todas as bênçãos em minha vida.

Palavras-chave Aço inoxidável 316L, ácido poli L-láctico (PLLA), filmes, piezoeletricidade, silanização, osseointegração, implantes ortopédicos, citocompatibilidade, Microscopia de Força Atômica (AFM).

Resumo Os metais e suas ligas são amplamente utilizados em implantes biomédicos, mas a falta de osseointegração na interface entre o biomaterial e o tecido hospedeiro leva à não fixação mecânica e infecção. Julga-se que a osseointegração pode ser melhorada usando um revestimento à base de materiais piezoelétricos. Estes materiais geram potencial elétrico em resposta às forças mecânicas aplicadas (e vice-versa). Os osteoblastos, que são responsáveis pelo crescimento e reparação óssea, respondem ao potencial de superfície. Um excelente candidato para esta aplicação é o PLLA, que é piezoelétrico, biocompatível e biodegradável. Neste trabalho, as caracterizações elétrica e biológica de aço inoxidável 316L coberto com filmes PLLA foram realizadas através de espectroscopia de impedância, AFM e testes de citocompatibilidade com células estaminais da polpa dentária humana (hDPSCs). A adesão entre esses materiais foi garantida pelo processo de silanização dos substratos. Os filmes de PLLA também foram caracterizados através de FTIR, XRD, análise de rugosidade superficial, SEM, teste de aderência, análise de ângulo de contacto e DSC. O ensaio de viabilidade Presto BlueTM mostrou que o filme de PLLA aumentou a viabilidade celular dos substratos. O ensaio de diferenciação osteogénica revelou que o filme de PLLA aumentou o potencial osteogénico inato das células e a diferenciação osteogénica. Além disso, as imagens de SEM permitiram observar a presença de fibroblastos com morfologia normal e sua formação de camadas sobre o filme de PLLA. Portanto, pode-se concluir que o dispositivo funcional desenvolvido tem um grande potencial para aplicação na engenharia de tecido ósseo.

Keywords

Stainless steel 316L, poly (L-lactic acid) (PLLA), films piezoelectricity, silanization, osseointegration, orthopedic implants, cytocompatibility, Atomic Force Microscopy (AFM).

Abstract

Metals and their alloys are widely used in biomedical implants but the lack of osseointegration at the interface between the biomaterial and the host tissue leads to non-mechanical fixation, infection and risk of rejection. The osseointegration can be improved using a coating based on piezoelectric materials. These materials generate electrical potential in response to applied mechanical forces. The osteoblasts, which are responsible for bone growth and repair, respond to the induced surface potential. An excellent-right candidate for this application is the poly (L-lactic acid) (PLLA), a synthetic polymer that is also biocompatible and biodegradable. In this work, electrical and biological characterization of stainless steel 316L substrates covered with PLLA films were performed, using impedance spectroscopy, AFM, and cytocompatibility tests with human dental pulp stem cells (hDPSCs). The adhesion between these materials was guaranteed by using the silanization process. The PLLA films were also characterized using FTIR, XRD, surface roughness analysis, SEM, tape test, contact angle analysis, and DSC. The Presto Blue™ viability assay showed that the PLLA film increased the cell viability on the substrates. Osteogenic differentiation assay showed that PLLA film enhanced the innate osteogenic potential of the cells and the osteogenic differentiation. The SEM images allowed seeing the presence of normal morphology of fibroblast cells and its layer formation on PLLA film. Concluding, the developed functional device has a great potential for bone tissue engineering application.

CONTENTS

LIST OF FIGURES	v
LIST OF TABLES	ix
ABBREVIATIONS	x
CHAPTER I - CONTEXT AND OBJECTIVES	2
1.1 Context	2
1.2 Objectives	3
CHAPTER II - STATE OF THE ART.....	5
2.1 Bone.....	5
2.1.1 Bone remodeling	8
2.1.2 Piezoelectricity of bone	10
2.2 Piezoelectricity	11
2.2.1 Piezoelectric polymers.....	13
2.2.2 Piezoelectricity application.....	15
2.2.3 Piezoelectric coatings and osseointegration	15
2.3 Biomaterials.....	16
2.4 Bone Tissue engineering	18
Polymers for bone tissue engineering.....	18

2.5 Metallic bone implants	19
2.5.1 Stainless Steel	19
2.5.2 Titanium alloy	20
2.5.3 Cobalt-chromium alloys	21
2.5.4 Surface modification of metallic implants.....	22
2.6 Polymeric coatings on metal substrates adhesion.....	23
PLLA coating on a metallic substrate.....	24
CHAPTER III - MATERIALS AND METHODS.....	29
3.1 Materials	31
3.2 Methodologies	31
3.2.1 Thermal treatment of SS316L substrates.....	31
3.2.2 Silanization of heat-treated SS316L substrates	33
3.2.3 Poly (L-lactic acid) solution preparation	33
3.2.4 Poly (L-lactic acid) films deposition	34
3.2.5 Crystallization process of Poly (L-lactic acid) films	36
3.3 Characterization techniques.....	37
3.3.1 Fourier Transformed Infrared Spectroscopy (FTIR)	38
3.3.2 X-Ray Diffractometry (XRD)	39

3.3.3 Surface roughness analysis.....	40
3.3.4 Microstructural studies by Scanning Electron Microscopy (SEM).....	43
3.3.5 Film adhesion by Tape test.....	44
3.3.6 Contact angle analysis	47
3.3.7 Differential scanning calorimetry (DSC)	48
3.3.8 Dielectric characterization.....	49
3.3.9 Atomic force microscopy (AFM).....	51
3.3.10 Cytocompatibility tests.....	57
 CHAPTER IV - RESULTS AND DISCUSSION.....	 60
4.1 Chemical composition by Fourier Transformed Infrared Spectroscopy (FTIR).....	60
4.2 Structural analysis by X-Ray Diffraction (XRD).....	63
4.3 Morphology and microstructure by Scanning Electron Microscopy (SEM).....	65
4.4 Surface roughness analysis.....	67
4.5 Adhesion measurements by Tape test	69
4.6 Wettability and surface energy by contact angle measurements.....	70
4.7 Thermal properties by Differential scanning calorimetry (DSC).....	72
4.8 Electric properties by Impedance spectroscopy	74
4.9 Topography, electrophysical and piezoelectric properties by Atomic force microscopy (AFM).....	80

4.10 Cytocompatibility	92
CHAPTER V - CONCLUSIONS AND FUTURE WORK	99
5.1 Conclusions	99
5.2 Future work	101
BIBLIOGRAPHY	103
APPENDICES	116
Appendix A: Cytocompatibility test protocols.....	116
Appendix B: Surface roughness results.....	118
Appendix C: Contact angles results.....	119

LIST OF FIGURES

Figure 1. The structure of a long bone [21].	6
Figure 2. Compact bone [21].	7
Figure 3. Spongy bone [21].	8
Figure 4. Stages in fracture repair. (a) a fracture hematoma, (b) internal and external calli, (c) cartilage of the calli is replaced by spongy bone, and (d) compact bone replaces spongy bone and complete healing [20].	9
Figure 5. Wolff's law. (a) load application cause compression and tension in the bone, (b) positive and negative charges are formed, and (c) start of bone resorption and growth processes (based on [23]).	10
Figure 6. Piezoelectric effect explained with a simple molecular model: (a) molecule without polarization; (b) molecule subjected to an external force (F_k), resulting in polarization (P_k); and (c) the piezoelectric material subjected to an external force (F), resulting in macroscopic polarization (P) [27].	12
Figure 7. Rectangular system of piezoelectric directions (based on [29]).	13
Figure 8. Molecular structure of poly (vinylidene fluoride) (PVDF) [32].	14
Figure 9. Molecular structure of the stereoisomers of poly (lactic acid) (PLA). a) poly (L-lactic acid) (PLLA) and b) poly (D-lactic acid) (PDLA) [40].	14
Figure 10. The contact angle between a substrate and a liquid (based on [90]).	23
Figure 11. Mechanism of silanization on a metallic surface (based on [116]).	27
Figure 12. Schematically representation of the experimental process used in this work to develop PLLA coatings on functionalized SS316L substrates.	30
Figure 13. a) SS316L substrates in a ceramic boat, b) schematic representation of the thermal treatment and c) the oven used.	32
Figure 14. The heat-treated SS316L substrates in a silane solution.	33
Figure 15. Apparatus used in PLLA solution preparation.	34
Figure 16. Spin-coater used in the PLLA film deposition.	34
Figure 17. Spin coating process (based on [119]).	35
Figure 18. Stages of the spin coating process (based on [119]).	36
Figure 19. a) Crystallization of coated substrates on thermal stirrer plate and b) crystallization process schedule.	37
Figure 20. Optical diagram of FTIR [120].	38
Figure 21. The geometric arrangement of X-ray diffractometer (adapted from [120]).	40
Figure 22. Rugosimeter (based on [122]).	41

Figure 23. The measure of the thickness films on the substrate using a rugosimeter (based on [123][124]).	43
Figure 24. Structure of an SEM (adapted from [120]).	44
Figure 25. a-c) Tape test process and d) 3D printed plastic accessory.	45
Figure 26. Wettability of a liquid droplet on a solid surface (based on [126]).	47
Figure 27. Principle of DSC technique (Based on [129]).	49
Figure 28. AFM technique representation.	52
Figure 29. Van der Waals curve. Atomic Force versus probe distance from a sample (based on [131][132]).	53
Figure 30. Imaging modes representation. Atomic Force versus probe distance from a sample. (based on [131][132]).	53
Figure 31. Phase lag measure (based on [131]).	54
Figure 32. Scheme of EFM operation (based on [132]).	55
Figure 33. Scheme of KPFM operation (based on [132]).	56
Figure 34. Expansion and contraction of the sample electric domains. Polarization (P) of the piezoelectric domain is (a) parallel and (b) anti-parallel to the applied electric field (E) (based on [132][133]).	57
Figure 35. FTIR spectroscopy results of SS316L TT (black line) and SS316L TT/SIL (red line) samples. Transmittance percentage (%) as a function of wavenumber (cm^{-1}) a) from 3150 to 350 cm^{-1} , b) from 950 to 350 cm^{-1} , c) from 1500 to 800 cm^{-1} , and d) from 2500 to 1800 cm^{-1} .	61
Figure 36. FTIR spectroscopy results of SS316L TT/SIL/PLLA samples. Transmittance percentage (%) as a function of wavenumber (cm^{-1}) a) from 3150 to 350 cm^{-1} , b) from 3100 to 2800 cm^{-1} , c) from 1900 to 1250 and d) from 1250 to 850 cm^{-1} .	62
Figure 37. XRD patterns of SS316L (black line), SS316L TT (red line) SS316L TT/SIL/PLLA (blue line) samples. Diffraction peak intensity (a.u) as a function of the diffraction angle (2θ degree).	65
Figure 38. Micrographs of SS316L TT/SIL/PLLA samples with different magnifications: a) 100x, b) 500x and c) 1000x.	66
Figure 39. The relative frequency in function of spherulite diameter (μm) of 628 spherulites from the SS316L TT/SIL/PLLA samples.	66
Figure 40. Arithmetic mean roughness (R_A) and mean roughness depth (R_Z) for each sample as mean \pm standard desviation. Differences were considered statistically	

significant at $p \leq 0.05$, and expressed by * ($0.01 < p \leq 0.05$), ** ($0.001 < p \leq 0.01$), *** ($0.0001 < p \leq 0.001$) and **** ($p \leq 0.0001$).	68
Figure 41. Micrographs of SS316L TT/SIL/PLLA samples after tape test with different magnifications: a) 100x, b) 500x and c) 1000x.	70
Figure 42. Heat flow (J/s.g) as a function of the temperature ($^{\circ}\text{C}$) by DSC of the PLLA film.	72
Figure 43. The specific enthalpy of fusion (J/g) of the PLLA film (ΔH_f).	73
Figure 44. Relative permittivity (ϵ_r) as a function of a) frequency and b) temperature.	76
Figure 45. Dielectric loss tangent ($\tan(\delta)$) as a function of a) frequency and b) temperature.	77
Figure 46. AC Resistivity (ρ) as a function of a) frequency and b) temperature.	79
Figure 47. (a) AFM topography scan image of PLLA film and (b) corresponding cross-section profile.	81
Figure 48. AFM topography and phase scan images acquired on different areas of the PLLA film: (a-b) in the vicinity of the substrate, (c-d) several μm from the substrate, and (e-f) at a significant distance from the substrate.....	82
Figure 49. AFM scan images of spherulite structure: a-b) morphology, c-d) grain boundary and e-f) fibril structure.....	84
Figure 50. Electrostatic Force Microscopy scan images of PLLA film: (a) topography, (b) 0, (c) + 5V, and (d) - 5V <i>dc</i> BV.....	86
Figure 51. KPFM scan images of the PLLA film surface: (a, c) topography, (b, d) surface potential distribution.....	87
Figure 52. PFM scan images of spherulite's grain boundary under rotation: a, d, g, j) topography, b, e, h, k) out-of-plane and c, f, i, l) in-plane responses.	88
Figure 53. PFM, EFM, and KPFM scan images: (a) topography, (b,c) out-of-plane and in-plane PFM responses of the non-poled area, (d) <i>dc</i> BV (± 40 V) poling pattern, (e-f) out-of-plane and in-plane PFM responses of the poled area, (g) electrostatic and (h) surface potential distributions.....	89
Figure 54. Cross-sections of PFM (a) out-of-plane and (b) in-plane phase images.	91
Figure 55. Corrected absorbance for different groups at every time-point (Mean \pm Standard Error). Differences were considered statistically significant at $p \leq 0.05$, and expressed by * ($0.01 < p \leq 0.05$), ** ($0.001 < p \leq 0.01$), *** ($0.0001 < p \leq 0.001$) and **** ($p \leq 0.0001$).	93

Figure 56. ARS concentration (mM) for undifferentiated and differentiated groups after 21 days (Mean \pm Standard Error). Differences were considered statistically significant at $p \leq 0.05$, and expressed by * ($0.01 < p \leq 0.05$), ** ($0.001 < p \leq 0.01$), *** ($0.0001 < p \leq 0.001$) and **** ($p \leq 0.0001$). 94

Figure 57. SEM images for the SS316L TT/SIL samples. a-c) unseeded group (no cells), d-f) seeded undifferentiated cells group, and g-i) seeded differentiated cells group. All groups were observed on different magnifications (250x, 500x, and 2500x). 95

Figure 58. SEM images for the SS316L TT/SIL/PLLA samples. a-c) unseeded group (no cells), d-f) seeded undifferentiated cells group, and g-i) seeded differentiated cells group. All groups were observed on different magnifications (250x, 500x, and 2500x). 96

LIST OF TABLES

Table I. Bone classification, features, functions and examples [20].	5
Table II. Bone cells, function and location [20].	7
Table III. Piezoelectric coatings used to improve the osseointegration of metallic substrates.	16
Table IV. Some applications of materials in medicine [57].	17
Table V. Chemical composition of SS316 and SS316L [75].	20
Table VI. Chemical composition of Ti6Al4V [76].	21
Table VII. Chemical composition of Co-Cr alloys [77].	22
Table VIII. Studies about PLLA coatings on a metallic substrate.	25
Table IX. Description of samples.	31
Table X. Surface roughness measurement conditions.	40
Table XI. Surface roughness measurement. Parameters representation.	42
Table XII. Classification of tape test results according to standard ASTM D3359 [125].	46
Table XIII. Impedance measurement conditions.	50
Table XIV. FTIR peak assignment of SS316L TT and SS316L TT/SIL samples.	61
Table XV. FTIR peak assignment of SS316L TT/SIL/PLLA samples [18][139].	63
Table XVI. XRD results. Crystallographic planes and identified compounds for SS316L, SS316L TT and SS316L TT/SIL/PLLA samples. [141][142].	64
Table XVII. Dispersive and polar parts of surface tension of water and diiodomethane [150].	71
Table XVIII. Calculated values of x and y for water and diiodomethane equation.	71

ABBREVIATIONS

AC - Alternating current

AFM - Atomic Force Microscopy

APTMS - 3-(Aminopropyl) trimethoxysilane

ARS - Alizarin Red Staining

CONTROL - Positive control group

DC - Direct current

DSC - Differential Scanning Calorimetry

E - Electric field

EFM - Electrostatic Force Microscopy

ϵ_r - Dielectric relative permittivity

FTIR - Fourier Transformed Infrared Spectroscopy

KPFM - Kelvin Probe Force Microscopy

nPTMS - n-propyl trimethoxysilane

P - Polarization

ρ - Resistivity

PFM - Piezoresponse Force Microscopy

PLLA - Poly (L-lactic acid)

R_A - Arithmetic mean roughness

R_{MAX} - Maximum roughness depth

R_Z - Mean roughness depth

SEM - Scanning Electron Microscopy

SIL - Silanization

SS - Stainless steel

$\tan(\delta)$ - Dielectric loss tangent

T_c - Crystallization temperature

T_g - Glass transition temperature

T_m - Melting temperature

TT - Thermal treatment

XPS - X-ray Photoelectron Spectroscopy

XRD - X-Ray Diffractometry

CHAPTER I
CONTEXT AND OBJECTIVES

CHAPTER I - CONTEXT AND OBJECTIVES

1.1 Context

The bone has a fundamental role in animal locomotion; it ensures that the skeleton can support heavy loads and cyclic efforts. It also protects delicate internal organs. This tissue has a high regenerative capacity in small-size defects, especially in the young population. However, in severe fractures, due to bone defects after resection of tumors and as a consequence of population aging, surgical interventions and the use of a bone substitute are needed [1][2].

Metals and their alloys are widely used in the production of biomedical implants. Titanium is bioinert (i.e., does not cause an inflammatory reaction), stainless steel, and cobalt-chromium alloys are biotolerated (i.e., may cause inflammatory reactions in the long run) [2]. Most metals have good mechanical properties and acceptable biocompatibility for the application. Despite this, the lack of osseointegration at the interface between the implants and the host tissue leads to non-mechanical fixation and infection. Consequently, the rate of failure and implant rejection becomes high [3].

Currently, several studies are addressing the coating of metals, to increase the osseointegration of orthopedic implants. Some examples of coatings are: calcium phosphates (CaP), bioactive glass (BG), zirconium titanate ($ZrTiO_4$) and hydroxyapatite (HA) [4]–[8]. Bones are piezoelectric due to the piezoelectric properties of collagen fibrils and hydroxyapatite crystals present in bone [9][10][11]. Thus, the osseointegration can be significantly improved using a piezoelectric material coating on a metal implant. The piezoelectric material generates electrical potential when a force is applied (and vice – versa), thus attracting osteoblasts responsible for bone growth and repair. A good candidate for this application is the poly (L-lactic acid) (PLLA), which, besides being a piezoelectric material, is a biocompatible and biodegradable material [12]–[14].

The study by Barroca, N. *et al.* [14], about non-poled and poled PLLA films by corona poling and piezoresponse force microscopy (PFM), demonstrated the ability of PLLA to improve the adhesion, spreading and proliferation of bone-like cells. However, the adhesion between organic and inorganic materials is a challenge to be overcome because of their physical and chemical differences. The success of this adhesion depends on the material and the surface treating process, such as anodizing, silanization, electromagnetic induction bonding, ultrasonic bonding, etc. [15]–[17].

The interface and adhesion of PLLA films on stainless steel substrates were studied by Adriana Magueta in her MsC thesis [18]. In this work, it was concluded that the adhesion between the metallic substrate and the polymeric coating is possible through a silanization process. Silanization is a chemical method through which the surface of a metal is covered with siloxanes, forming an intermediate layer. The goal of silanization is to form molecular bridges at the interface between the organic and inorganic materials [19].

Within this context, a further step was taken in the present work. Electrical and biological characterization of 316L stainless steel (SS316L) covered with PLLA films was studied. Using the optimal silanization time, PLLA solution concentration, the number of layers deposited and degree of crystallization previously studied by Magueta [18], we have shown that the PLLA coating works as a functional device based on its electromechanical properties relevant to tissue engineering.

1.2 Objectives

The main objective of this work was to perform electrical and biological characterization of stainless steel 316L substrates covered with PLLA films. The following specific objectives were considered:

- a) Production of SS316L covered with PLLA films using silanization for the adhesion and spin coating for deposition;
- b) Physical and chemical characterization of SS316L covered with PLLA films;
- c) Electrical characterization on SS316L covered with PLLA films;
- d) Cytocompatibility tests on SS316L covered with PLLA films.

CHAPTER II
STATE OF THE

CHAPTER II - STATE OF THE ART

2.1 Bone

The primary use of the devices develop and studied in this work is for bone application, so, the understanding of bone functions, structure and composition is necessary.

The skeletal system is composed of bones and cartilage. It performs critical functions for the human body such as to support the body, to facilitate movement, to protect internal organs, to produce blood cells, and store and release minerals and fat. The bone can be classified according to its shape, as shown in Table I [20].

Table I. Bone classification, features, functions and examples [20].

Bone classification	Features	Function(s)	Examples
Long	Cylinder-like shape, longer than it is wide.	Leverage.	Femur, tibia, fibula, metatarsals, humerus, ulna, radius, metacarpals, phalanges.
Short	Cube-like shape, approximately equal in length, width, and thickness.	Provide stability, support, while allowing for some motion.	Carpals, tarsals.
Flat	Thin and curved.	Points of attachment for muscles; protectors of internal organs.	Sternum, ribs, scapulae, cranial bones.
Irregular	Complex shape.	Protect internal organs.	Vertebrae, facial bones.
Sesamoid	Small and round; embedded in tendons.	Protect tendons from compressive forces.	Patellae.

The structure of a long bone is represented in Figure 1. Each long bone is divided into two parts: diaphysis in the central shaft and epiphyses in two ends. The diaphysis consists of compact bone and medullary cavity with a thinner connective tissue membrane called endosteum. Compact bone has repeating units called osteons, which are concentric rings of lamellae. The epiphysis consists of spongy bone and a thin layer of articular cartilage covering the place where the bone joints with other bones. Spongy bone consists of delicate interconnecting rods or plates of the bone called trabeculae. The spaces between the trabeculae are filled with marrow and blood vessels [20][21].

An epiphyseal plate is a place where bone grows in length and when the bone growth stops. The cartilage of each epiphyseal plate becomes an epiphyseal line. Most of

the outer surface of a bone is covered by dense connective tissue called the periosteum, which consists of two layers and contains blood vessels and nerves [20][21].

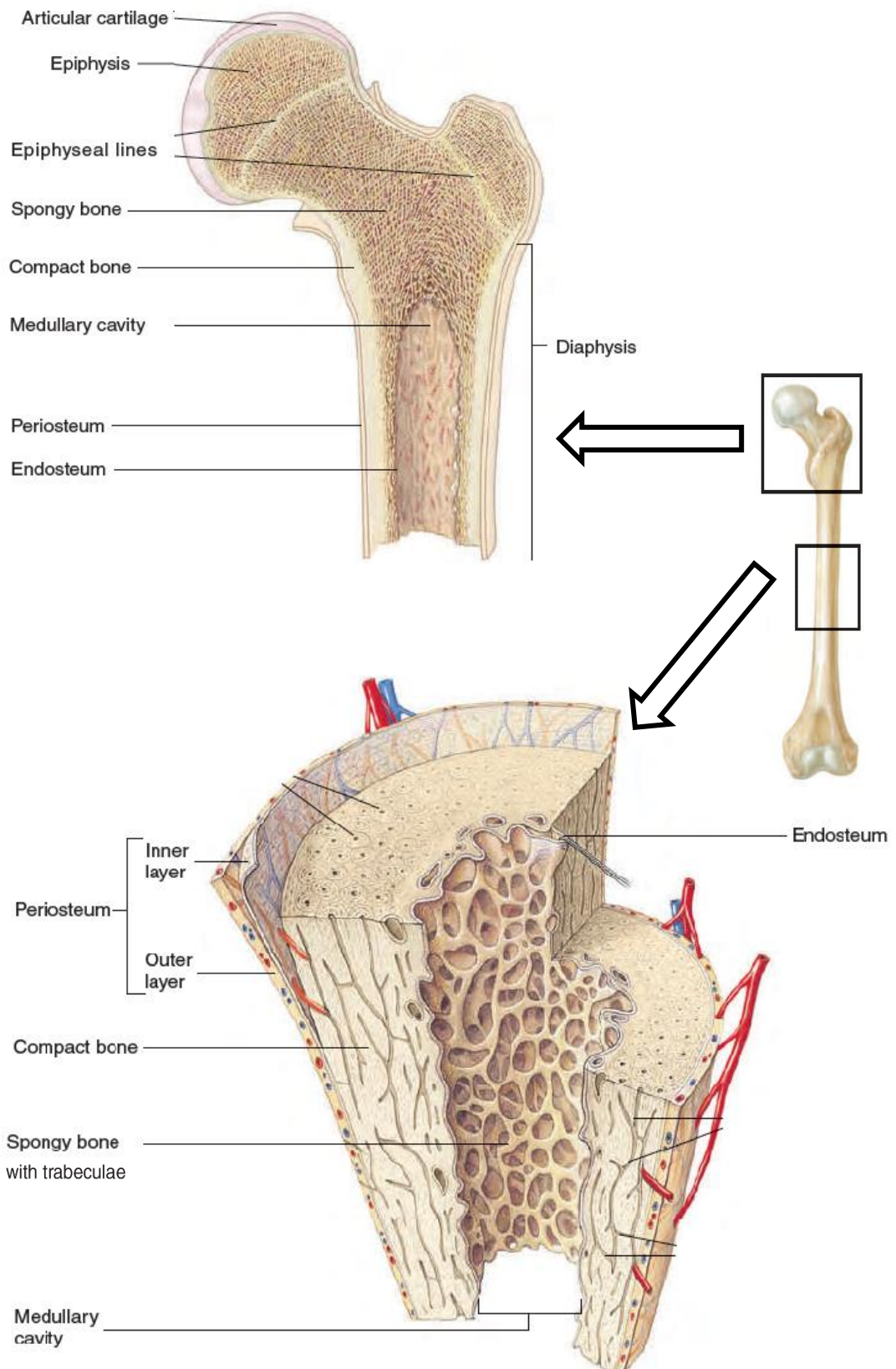


Figure 1. The structure of a long bone [21].

Although bone cells compose a small amount of the bone volume, they are crucial to the function of bones like repair and remodeling. Four types of cells are found within bone tissue: osteogenic cells, osteoblasts, osteocytes, and osteoclasts [20]. The functions and localizations of these cells can be seen in Table II.

Table II. Bone cells, function and location [20].

Cell type	Function	Location
Osteogenic cells	Develop into osteoblasts	Deep layers of the periosteum and the marrow
Osteoblasts	Bone formation	Growing portions of bone, including periosteum and endosteum
Osteocytes	Maintain the mineral concentration of the matrix	Entrapped in the matrix
Osteoclasts	Bone resorption	Bone surfaces and at sites of old, injures, or unneeded bone

Bone cells can be found in compact and in spongy bone. In compact bone, osteocytes are located in lacunae between the lamellae of each osteon. The lamellae are connected in canaliculi (Figure 1Figure 2). In spongy bone, each trabecular has several lamellae with osteocytes among them. Osteoclasts and osteoblasts are on the surface of the trabecula (Figure 3) [21].

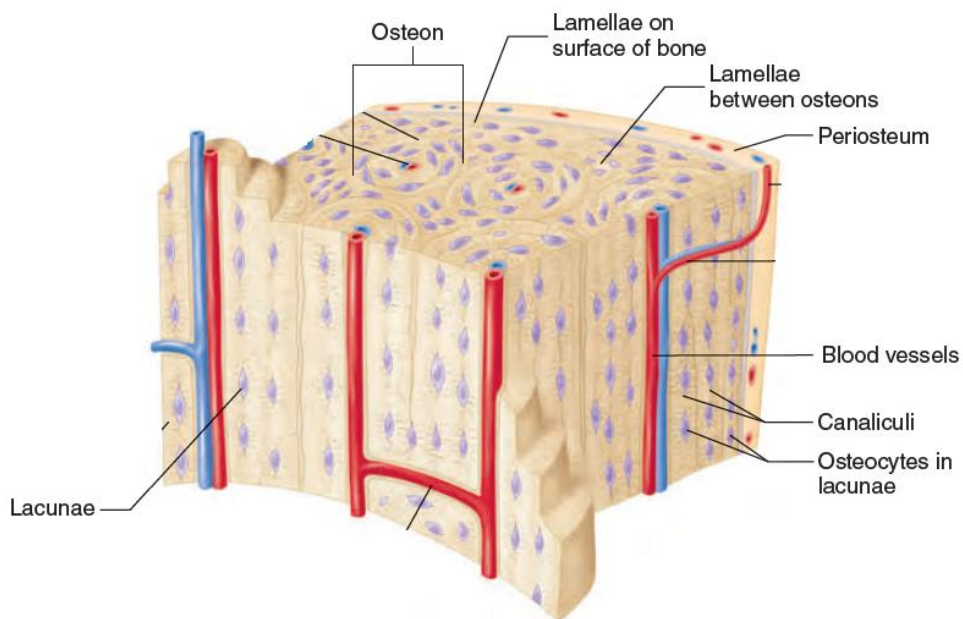


Figure 2. Compact bone [21].

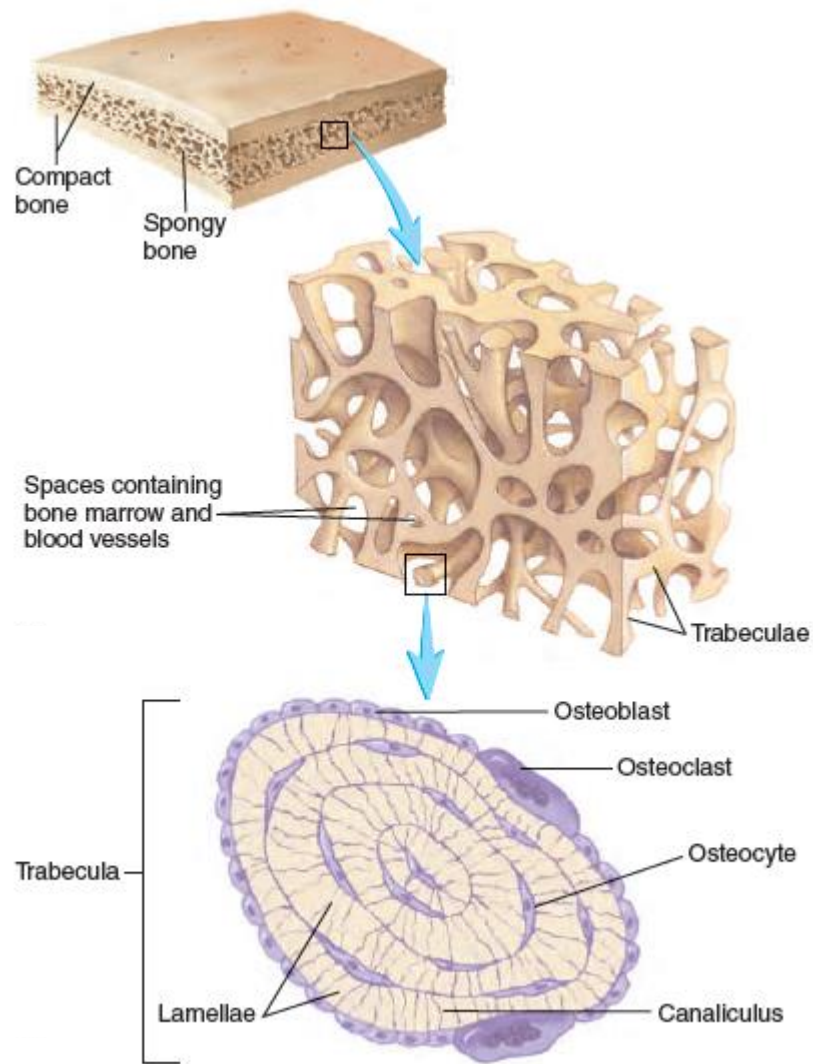


Figure 3. Spongy bone [21].

2.1.1 Bone remodeling

A long bone increases as new bone is deposited on the outer surface by osteoblasts. At the same time, bone is removed from the internal medullary surface of the bone by osteoclasts. Remodeling occurs in the whole bone and is responsible for changes in bone shape, bone growth, the adjustment of bone to stress, bone repair, and calcium regulation in body fluids [21].

When a bone is broken, the blood vessels are damaged and a clot (hematoma) is formed in the damaged area (Figure 4.a). About two or three days after the injury, blood vessels and surrounding tissues begin to invade the clot and form the callus which is a network of fibers and islets of cartilage between the two bone fragments (Figure 4.b). Between the fourth and sixth week after the injury, the osteoblasts enter the callus and

form spongy bone (Figure 4.c). Subsequently, the spongy bone is slowly remodeled to form compact bone and the repair is complete (Figure 4.d) [21].

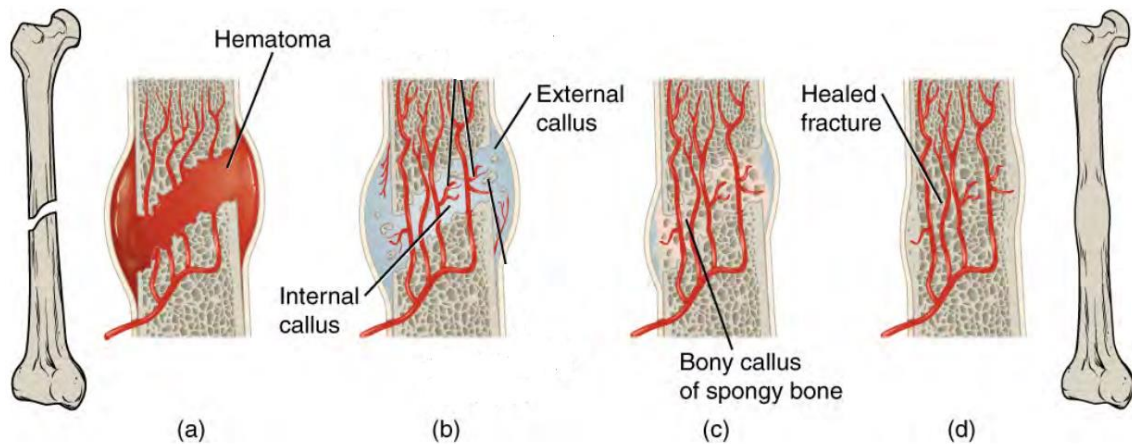


Figure 4. Stages in fracture repair. (a) a fracture hematoma, (b) internal and external calli, (c) cartilage of the calli is replaced by spongy bone, and (d) compact bone replaces spongy bone and complete healing [20].

As seen, bone remodeling is a complex process that requires interaction between different cells. This process is regulated by a variety of biochemical and mechanical factors. The major biochemical regulators include parathyroid hormone (PTH), calcitriol, and other hormones such as growth hormone, glucocorticoids, thyroid hormones, and sex hormones. Mechanical factors are associated with self-regulation and consist of the response to the mechanical forces acting upon bone tissues. For this, the trabeculae in spongy bone tend to align with the directions of the principal stresses applied to the bone, causing compression and tension. Positive charges are formed in the tension region and negative charges are formed in the compression region. The osteoclasts and osteoblasts are attracted to charges and the processes of bone resorption and growth begin. This theory is explained using Wolff's law that is schemed in Figure 5 [22][23].

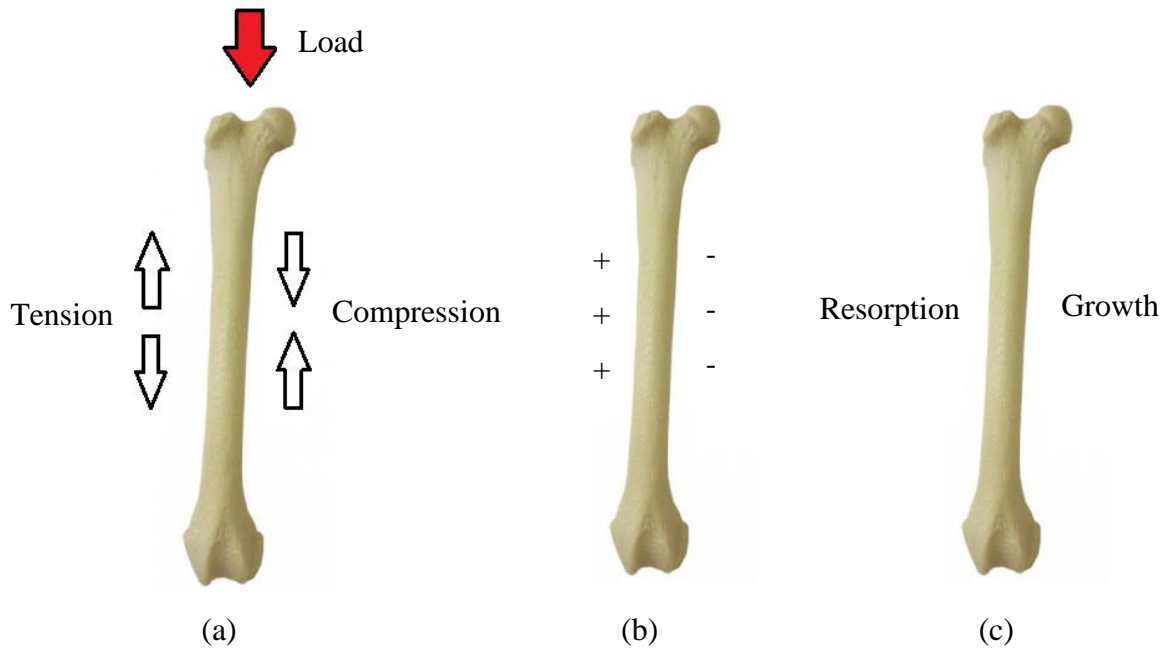


Figure 5. Wolff's law. (a) load application cause compression and tension in the bone, (b) positive and negative charges are formed, and (c) start of bone resorption and growth processes (based on [23]).

The bone response to mechanical stress leads to the activation of osteogenic cells. The osteoblasts are recruited in the periosteum or endosteum to grow new bone and osteoclasts are recruited to resorb bone along a surface. The final result is bone remodeling [24]. For instance, during bone repair, the bone cannot be completely immobilized, because the mechanical stresses are essential for bone formation [21].

2.1.2 Piezoelectricity of bone

Fukada, E. *et al.* [9] in 1957 proposed that the formation of electrical charges as a result of stress application in bone is due to the piezoelectric response originated by the presence of collagen fibrils. When the collagen is submitted to internal stress, it can generate electric signals transmitted through the cell membrane, attracting osteoblasts that start the bone repair and growth on the stressed side [25]. Recent studies have also shown that piezoelectricity in bones may be associated with the piezoelectric properties of hydroxyapatite crystals present in bone, though not fully proven or accepted [10][11].

To better understand the origins of piezoelectricity in bone, basic concepts of piezoelectricity are introduced below.

2.2 Piezoelectricity

Functional materials are materials able to perform a particular function under a determined stimulus. The function is associated with their electric, magnetic or optical properties. This group of materials includes dielectrics (pyroelectrics, piezoelectrics, and ferroelectrics), semiconductors, ionic conductors, superconductors, electro-opticals, and magnetic materials [26].

Dielectric materials are electrical insulators (nonmetallic) yet susceptible to polarization alignment (dipole moments arrangement) in response to an applied electrical field. Ferroelectrics are the class of dielectric materials that exhibit spontaneous polarization and can be polarized by the application of an electric field or mechanical stress [27].

Pierre and Jacques Curie discovered the piezoelectric effect in 1880. They conducted various experiments and founded that some crystals displayed surface charges when they were mechanically stressed, such as tourmaline, quartz, topaz, cane sugar, and Rochelle salt. The word “piezo” is a Greek word that means “to press”. Therefore, piezoelectricity means electricity generated from pressure [28].

The piezoelectric effect is the generation of an electric charge due to the application of mechanical stress and vice versa. The polarization generated from mechanical stress is called direct or generator effect, while converse or motor effect is associated with the mechanical deformation derived from the applied electric field [26].

A simple molecular model shown in Figure 6 explains this effect. The molecules are electrically neutral before subjecting the material to mechanical stress, that is, the centers of the negative and positive charges of each molecule coincide (Figure 6.a). However, the presence of mechanical stress causes separation of the positive and negative centers of the molecules and the dipoles are formed (Figure 6.b). As a result, the poles inside the material cancel each other and charges appear on the surface (Figure 6.c), causing the macroscopic polarization of the material that generates an electric field [27].

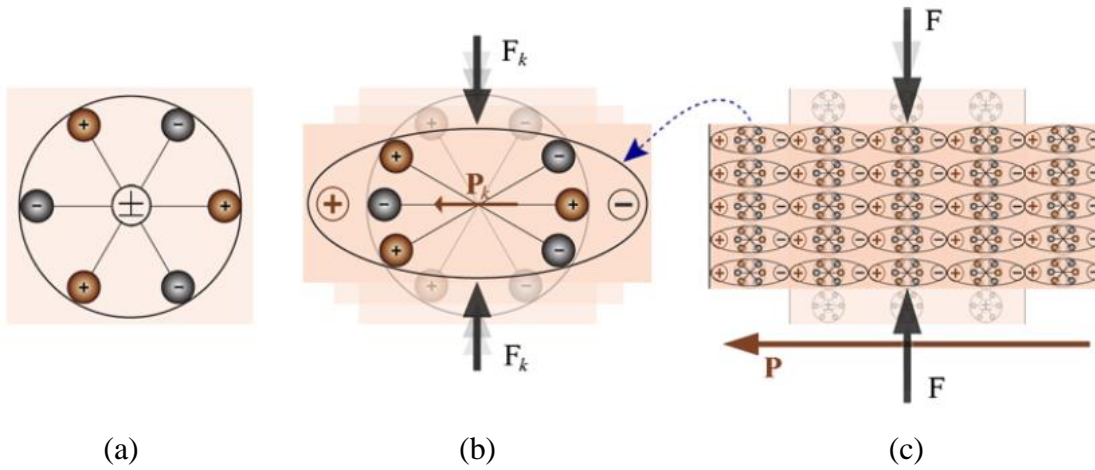


Figure 6. Piezoelectric effect explained with a simple molecular model: (a) molecule without polarization; (b) molecule subjected to an external force (F_k), resulting in polarization (P_k); and (c) the piezoelectric material subjected to an external force (F), resulting in macroscopic polarization (P) [27].

The magnitude of polarization (P) depends on the magnitude of the stress (σ) and the sign of the produced charge (positive or negative) depends on the type of applied stress (tensile or compressive). The relationships between the strain (F), stress (σ), electric field strength (E), and electric polarization (P) is:

$$P = d \sigma \text{ (direct effect)} \quad \text{Equation 1}$$

$$F = dE \text{ (converse effect)} \quad \text{Equation 2}$$

where d is the piezoelectric coefficient.

The effective coupling coefficient (k_{eff}) is another important parameter to evaluate the performance of a piezoelectric material. This coefficient measures the amount of electrical energy that is converted into a strain or vice-versa is defined as [26]:

$$K_{\text{eff}}^2 = \frac{\text{electrical energy converted into mechanical energy}}{\text{input electrical energy}} \quad \text{Equation 3}$$

(direct effect)

$$K_{\text{eff}}^2 = \frac{\text{mechanical energy converted into electrical energy}}{\text{input mechanical energy}} \quad \text{Equation 4}$$

(converse effect)

The piezoelectric charge constant has two subscripts. The first one indicates the direction of the induced polarization or the electric field applied, while, the second indicates the direction of the induced strain or stress applied. The directions in X, Y, or Z axes are represented by 1, 2, or 3, respectively, and shear about one of these axes is represented by 4, 5, or 6, respectively (Figure 7) [29].

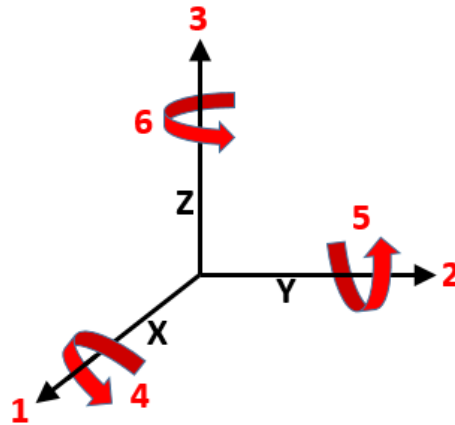


Figure 7. Rectangular system of piezoelectric directions (based on [29]).

2.2.1 Piezoelectric polymers

The most known piezoelectric polymer is the poly (vinylidene fluoride) (PVDF) which has piezoelectric coefficients of $d_{33} = 13 - 28 \text{ pC/N}$ and $d_{31} = 6 - 20 \text{ pC/N}$ [30]. Its chemical structure is formed of two fluorine atoms at every second carbon atom in the hydrocarbon backbone (Figure 8). Usually, it exists in the most stable, nonpolar α form, wherein the fluorine (F) atoms are arranged alternately on both sides of the hydrocarbon chain and does not exhibit a piezoelectric effect. However, in the β form, the fluorine atoms are located on the same side of the chain, resulting in the permanent dipole formation [31].

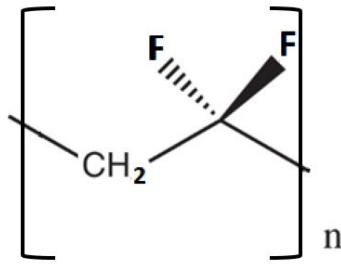


Figure 8. Molecular structure of poly (vinylidene fluoride) (PVDF) [32].

The other important piezoelectric polymer is poly (L-lactic acid) (PLLA), which has piezoelectric coefficients of $d_{14} = 11$ pC/N [33]. PLLA is widely used in the biomedical field due to its excellent biodegradability, biocompatibility, and piezoelectric properties. It is among the few polymers approved by the United States Food and Drug Administration (FDA) for specific human clinical applications [14][34][35].

PLLA is a stereoisomer of poly (lactic acid) (PLA). PLA is formed by polymerization of the lactic acid monomer, which is a simple chiral molecule that exists in two forms: L- and D-lactic acid. Thus, two different polymers are formed: poly (L-lactic acid) (PLLA) and poly (D-lactic acid) (PDLA) (Figure 9). Lactic acid is a natural organic acid present in materials that contain glucose, sucrose, and lactose, such as molasses, whey, sugarcane bagasse, cassava bagasse, wheat, and barley [36]. Lactic acid is a polar molecule due to the carbonyl group (C=O), which has a polarized covalent bond. The oxygen atom is more electronegative and attracts electrons [37]. PLA is a non-polar polymer without electric field application, but, when an electric field is applied, the dipoles align along with the electric field. This effect is known as an induced polarization [38][39].

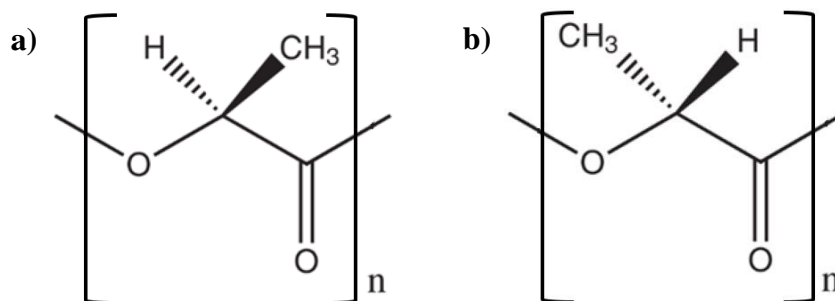


Figure 9. Molecular structure of the stereoisomers of poly (lactic acid) (PLA). a) poly (L-lactic acid) (PLLA) and b) poly (D-lactic acid) (PDLA) [40].

The electrical conductivity in polymers is based on the presence of double bonds (weak π chemical bonds) along the polymer chain. Using the doping process, charge defects (polarons) are created, allowing the flow of charges over long distances. These charge defects are "holes" (orbitals with a missing electron) that are filled by electrons of neighboring carbon atoms. The conductivity of the polymer depends on the density of charge carriers (number of charges per unit volume) and their mobility (how fast they can move in the material) [41].

2.2.2 Piezoelectricity application

The piezoelectric materials can convert an electric field into mechanical energy and mechanical deformation into electrical energy. They exhibit several potential applications in distinct industries like computing, automotive, medical, military, and consumer. These materials can be applied in microelectromechanical systems (MEMSs), sensors, actuators, motors, energy harvesters, etc. [42]–[47]. Their applications are mainly dependent on various piezoelectric characteristics such as the electromechanical coupling factor (k), relative dielectric permittivity ($\epsilon^T_{33}/\epsilon_0$), specific volume electric resistance (ρ_v), Curie temperature (T_c), electrical durability (E_{np}), and others [43].

2.2.3 Piezoelectric coatings and osseointegration

A literature search on piezoelectric coatings used to improve the osseointegration of metallic substrates was performed (Table III). The results show that this subject was little studied. The most of piezoelectric coatings are ceramic materials, for example, hydroxyapatite (HA), titanium dioxide (TiO_2) and barium titanate (BaTiO_3). Only substrates made of titanium and its alloys were studied.

Table III. Piezoelectric coatings used to improve the osseointegration of metallic substrates.

Piezoelectric coating	Substrate	Year	Ref.
HA/PVDF	Ti plate	2021	[48]
TiO ₂ /BaTiO ₃ nanotubes	Ti plate	2020	[49]
BaTiO ₃ nanoparticles	Ti6Al4V scaffold	2020	[50]
TiO ₂ /BaTiO ₃	Ti6Al4V plate	2020	[51]
BaTiO ₃	Ti6Al4V plate	2016	[52]
BaTiO ₃	Ti sheet	2007	[53]

2.3 Biomaterials

The loss or failure of an organ or tissue is one of the most frequent and devastating problems in human health. Medical doctors treat organ or tissue loss by transplanting organs from one individual into himself or another, performing surgical reconstruction, or using mechanical devices [54].

Biomaterials are materials that are intended to interact with biological systems to treat, increase or replace tissues, organs, or functions of the human body, according to the European Society for Biomaterials (ESB) [55]. The successful application of a material in the body depends on its biofunctionality and biocompatibility. When applied, it must replace the function for which it was created, having adequate mechanical strength, allowing good cell adhesion to its surface, having no oncogenic characteristics, being hemostatic, and sterilizable [2].

Biomaterials may be classified by their chemical composition and biological behavior. Regarding chemical composition, materials are classified as metals, ceramics and glasses, polymers, and composites. Considering biological behavior, the classification is based on host tissue response. The material can be inert, biotolerated, bioactive, and resorbable. Bioinert materials do not cause foreign body reactions and are directly connected to the receptor tissue, for example, titanium, zirconia, and alumina. Biotolerables are moderately accepted by the body and are usually surrounded by a fibrous capsule such as stainless steel, chromium cobalt alloys, and polymethyl methacrylate (PMMA). Bioactive materials form a direct bond to living tissues, having in their composition calcium and/or phosphorus ions that interact with the surrounding

bone, for example, hydroxyapatite and bioactive glasses. Resorbable materials are materials that slowly degrade and are gradually replaced by the tissues in which they are implanted, for example, chitosan, poly (glycolic acid), and poly (lactic acid) [2][56]. Some applications of materials in medicine can be found in Table IV.

Table IV. Some applications of materials in medicine [57].

Application	Types of materials
<u>Skeletal system</u>	
- Joint replacements (hip, knee).	- Titanium, Ti-Al-V alloy, stainless steel, polyethylene.
- Bone plate for fracture fixation.	- Stainless steel, cobalt-chromium alloy.
- Bone cement.	- Poly (methyl methacrylate).
- Bony defect repair.	- Hydroxyapatite.
- Artificial tendon and ligament.	- Teflon, Dracon.
- Dental implant for tooth fixation.	- Titanium, Ti-Al-V alloy, stainless steel, polyethylene, alumina, calcium phosphate.
<u>Cardiovascular system</u>	
- Blood vessel prosthesis.	- Dacron, Teflon, polyurethane.
- Heart valve.	- Reprocessed tissue, stainless steel, carbon.
- Catheter.	- Silicone rubber, Teflon, polyurethane.
<u>Organs</u>	
- Artificial heart.	- Polyurethane.
- Skin repair template.	- Silicone-collagen composite.
- Artificial kidney (hemodialyzer)	- Cellulose, polyacrylonitrile.
- Heart-lung machine.	- Silicone rubber.
<u>Senses</u>	
- Cochlear replacement.	- Platinum electrodes.
- Intraocular lens.	- Poly (methyl methacrylate), silicone rubber, hydrogel.
- Contact lens.	- Silicone-acrylate, hydrogel.
- Corneal bandage.	- Collagen, hydrogel.

Although traditional therapies have saved and improved countless lives, they still give imperfect solutions. Transplantation is severely limited by a critical donor shortage, surgical reconstruction can result in long-term problems and mechanical devices cannot perform all of the functions of a single organ and therefore cannot prevent progressive patient deterioration. Trying to solve these problems a new field, tissue engineering, has come to light, associated with the concept of regeneration, hardly achieved with most biomaterials [54].

2.4 Bone Tissue engineering

Tissue engineering applies the principles of life sciences and engineering to the development of functional substitutes to restore, maintain, or improve tissue function in damaged tissue [54]. In the future, engineered tissues could accelerate the development of new drugs and reduce the need for organ transplants [58].

A material for tissue engineering application has to have the following characteristics: (i) to be biocompatible and bioresorbable with a controllable degradation and resorption rate to compliment cell/tissue growth and maturation. (ii) physicochemical properties, morphology, and degradation kinetics that allow migration, proliferation, and differentiation of cell types of interest and enable flow transport of nutrients and metabolic waste. (iii) mechanical properties matching those of the tissues at the implantation site [58]–[61].

The bone tissue engineering materials should stimulate and support the onset and the continuance of bone in-growth, and subsequent remodeling and maturation by providing the mechanical properties and geometrical shapes required [60][61]. The osseointegration is essential for the performance of these functions and is defined as the bonding of living bone tissue with surgical implants so that implants can replace bone and perform load-bearing functions. An implant is considered osseointegrated if there is no relative motion between the implant and bone [62].

Tissue restoration occurs in two different ways: cell-based and cell-free. The cell-based restoration uses scaffolds as a carrier to deliver cells to increase the number of cells at the damaged area and to promote the regeneration process. The cell-free restoration uses scaffolds capable of delivering specific signals to stimulate local cells and to increase the body's capacity for regeneration [63].

Polymers for bone tissue engineering

Polymers present attractive properties when compared to inorganic materials, such as lightness, low cost, good electrical, and mechanical resistance [64]. Polymeric implants are used for osseointegration, bone growth, and regeneration, due to their ability to deliver bioactive agents [65].

In the last decades, a variety of natural and synthetic polymers emerged as potential biomaterials for tissue engineering. Natural materials are obtained from natural sources, exhibiting similar molecular structures to the tissue they are replacing, which allow them to enhance the cells' performance in the biological system. Among the natural

polymers that can be used in tissue engineering applications, we can find proteins (silk, collagen, gelatin, fibrinogen, elastin, keratin, actin, and myosin), polysaccharides (cellulose, amylose, dextran, chitin, and glycosaminoglycans), or polynucleotides (DNA, RNA) [66][67]. Synthetic polymers are highly useful in the biomedical field because their properties can be adapted for specific applications [68]. Poly (lactic acid) (PLA), poly (glycolic acid) (PGA), poly (lactic-co-glycolic acid) (PLGA), and polyhydroxyalkanoate (PHA) are among the most commonly used synthetic polymers in tissue engineering [67][69][70].

Although an extensive list of polymers has been studied regarding tissue engineering applications, most of the developed scaffolds have been used passively, just as support for the cells and tissues. Therefore, it becomes necessary to develop smart materials for tissue engineering applications, for example, functional piezoelectric polymers [71][72].

2.5 Metallic bone implants

The increase in life expectancy and the aging world population causes an increase in musculoskeletal disorders such as fractures, osteoporosis, and bone metastases. Consequently, the use of orthopedic implants also increases [73]. Current methods for surgical treatments of fractures and joint arthroplasties primarily use metal implants. Among the metallic materials, AISI stainless steel 316L, pure titanium and titanium alloys, and cobalt-chromium alloys have been widely utilized in orthopedic implants. These metallic materials are biocompatible due to the formation of a passive oxide layer on their surface and exhibit high mechanical strength and corrosion resistance that have encouraged their use in load-bearing implants [74].

2.5.1 Stainless Steel

The chemical composition of SS316 and SS316L is presented in Table V. Both materials are austenitic stainless steels and nonmagnetic, yet the SS316L is an extra-low carbon variation of SS316 that eliminates harmful carbide precipitation due to welding [75]. The chromium promotes the passivation ability while the molybdenum enhances the corrosion resistance. However, the corrosion resistance of stainless steel 316L is not sufficiently high. The release of iron, chromium, and nickel can be toxic and cause various health risks such as swelling, skin changes, discomfort, etc [74][75].

Table V. Chemical composition of SS316 and SS316L [75].

Composition	Type 316 (wt %)	Type 316L (wt %)
Carbon (C)	0.08 max	0.03 max
Manganese (Mn)	2.00 max	2.00 max
Phosphorus (P)	0.045 max	0.045 max
Sulfur (S)	0.03 max	0.03 max
Silicon (Si)	0.75 max	0.75 max
Chromium (Cr)	16.00 – 18.00	16.00 – 18.00
Nickel (Ni)	10.00 – 14.00	10.00 – 14.00
Molybdenum (Mo)	2.00 – 3.00	2.00 – 3.00
Nitrogen (N)	0.10 max	0.10 max
Iron (Fe)	Balance	Balance

2.5.2 Titanium alloy

Ti6Al4V is the most widely used titanium alloy. Its chemical composition is shown in Table VI. Titanium alloys are a suitable replacement for SS due to their better corrosion resistance, less stiffness, and easier machining capabilities. Although the Ti6Al4V has good mechanical strength, the release of vanadium and aluminum ions, and its high Young's modulus (113 GPa), when compared with cortical bone's Young's modulus (15-20 GPa), may limit the usability of this material for long term situations. Reduction of α phase in titanium alloys decreases Young's modulus; therefore, the titanium alloys with higher β phase (β titanium) have been explored for use in trauma implants [74].

Table VI. Chemical composition of Ti6Al4V [76].

Composition	ASTM F1108	ASTM F1472
	Cast material (wt %)	Wrought material (wt %)
Aluminium (Al)	5.50 – 6.75	5.50 – 6.75
Vanadium (V)	3.50 – 4.50	3.50 – 4.50
Carbon (C)	< 0.10	< 0.08
Iron (Fe)	< 0.30	< 0.30
Oxygen (O)	< 0.20	< 0.20
Nitrogen (N)	< 0.05	< 0.05
Hydrogen (H)	< 0.015	< 0.015
Titanium (Ti)	Balance	Balance

2.5.3 Cobalt-chromium alloys

Cobalt chromium alloys have a high surface hardness and wear resistance, which makes them hard to polish. Consequently, these alloys are applied for joint replacement prostheses such as the femoral component in total knee replacement and the femoral head in total hip replacement [74][77]. The chemical composition of Co-Cr alloys is shown in Table VII.

Table VII. Chemical composition of Co-Cr alloys [77].

Composition	ASTM F75 (wt %)
Chromium (Cr)	27.00 – 30.00
Molybdenum (Mo)	5.00 – 7.00
Nickel (Ni)	< 0.50
Iron (Fe)	< 0.75
Carbon (C)	< 0.35
Silicone (Si)	< 1.00
Manganese (Mn)	< 1.00
Tungsten (W)	< 0.20
Phosphorus (P)	< 0.02
Sulphur (S)	< 0.01
Nitrogen (N)	< 0.25
Aluminium (Al)	< 0.10
Titanium (Ti)	< 0.10
Bor (R)	< 0.01
Cobalt (Co)	Balance

2.5.4 Surface modification of metallic implants

Although these metal implants are biocompatible, they can fail due to insufficient osseointegration, which causes motion, wear, and loosening of the implant. Since the surface is the only region in contact with host bone tissue, many attempts have been made to modify the surface properties to enhance host tissue integration and mechanical fixation. Different surface treatments and coatings can be used to modify metal surfaces [12][74]. The most relevant ones are described in the following text.

Recent studies show that surface treatment with plasma and sodium hydroxide can improve the metal osseointegration [78]–[81]. Coating of metallic materials is also being studied and it was proved that coatings made of hydroxyapatite (HAp), polydopamine (PDA), graphene oxide (GO), bioactive glass, and silk fibroin (SF) have enhanced the mechanical fixation of the implant to the bone [65], [82]–[85]. Among these coatings, the polymeric coatings have been noteworthy, but piezoelectric polymers for bone tissue engineering have been little studied. Poly (L-lactic acid) (PLLA), polyhydroxybutyrate (PHB), polyvinylidene difluoride (PVDF), and collagen are examples of piezoelectric

polymers that enable the production of films, hydrogels, and scaffolds for bone tissue engineering [86]–[89].

2.6 Polymeric coatings on metal substrates adhesion

Polymeric coatings on metal implant materials have great potential in improving host tissue acceptance and preventing rejection, but the adhesion between an organic and inorganic material is a challenge to be overcome due to the physical and chemical differences between these materials [15][16].

Adhesion is the state in which two surfaces are held together by interphase forces. It is the sum of all the intermolecular or interatomic interactions. It can be measured by observing the wetting behavior of the liquid by the contact angle and applying Young's equation (Figure 10 and Equation 5).

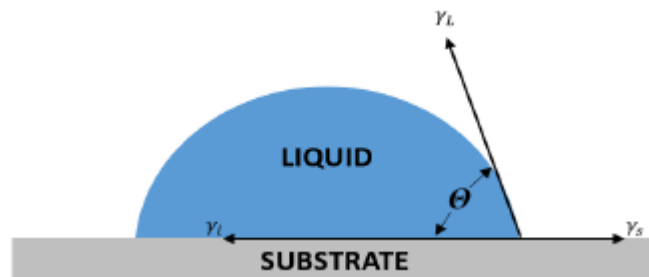


Figure 10. The contact angle between a substrate and a liquid (based on [90]).

$$\gamma_s = \gamma_i + \gamma_L \cos \theta \quad \text{Equation 5}$$

In this equation, γ_s is the substrate/liquid interfacial free energy, γ_i is the substrate surface free energy, γ_L is the liquid surface free energy, and θ is the contact angle between γ_L and γ_i [90].

Practical adhesion is measured in terms of forces required to separate the materials. It is expressed in terms of tensile or shear strengths. Tensile strength is the applied pulling force to the entire area of the adherent material to remove a certain area of it. This force is applied in the perpendicular direction to the adhesion surface. The shear strength is measured exactly in the same way as the tensile strength, but the force is applied in the parallel direction to the adhesion surface [91].

Adhesion can be improved through a physical surface modification or the creation of an intermediate layer. Physical treatments are used frequently to roughen materials

surfaces, using mechanical abrasion because adhesion generally increases when the contact area on the surface increases. Coating or intermediate layer formation such as silicon nitride, oxide, and siloxane can also enhance the metal-polymer adhesion [17], [92]–[96].

PLLA coating on a metallic substrate

A literature search on PLLA coating on metallic substrates (Table VIII) revealed that few studies have been performed on this subject. In most cases, the polymeric coating aimed to improve the corrosion resistance of the metal.

Table VIII. Studies about PLLA coatings on a metallic substrate.

<i>Coating</i>	<i>Substrate</i>	<i>Coating function</i>	<i>Adhesion/ Deposition method</i>	<i>Year</i>	<i>Ref.</i>
Poly (L-lactide)(PLLA)	Mg-Zn-Y-Nd alloy	Improving corrosion resistance	Electropolymerized dopamine (ePDA) coating	2019	[97]
Poly (L-lactide)(PLLA)	Magnesium rods	Improving corrosion resistance	Nonsolvent Induced	2018	[98]
Hafnium/poly (l, l-lactide) (Hf/PLLA)	Magnesium alloy	Improving degradation, corrosion resistance, and cytocompatibility	Magnetron sputtering coupled	2018	[99]
Poly (L-lactide)(PLLA)	Zinc stent	Drug-eluting polymer layers to inhibit harmful biological responses	Silanization	2017	[100]
Hydroxyapatite (HA)/poly-L-lactic acid	Magnesium alloy	Improving corrosion resistance	HA interlayer	2016	[101]
PLLA/PEGDMA	Nitinol stent	Avoiding stents thrombosis and in-stent restenosis.	Electrospinning technique	2016	[102]
Poly (L-lactide)(PLLA)	Bare metal L-605 stents	Holding and release the drug	Spray-coating process	2015	[103]
PLGA(PTX)/PLLA/MAO	AZ81 magnesium alloy stent	Controlling drug release and corrosion	–	2015	[104]
PEO/PLLA	Biodegradable AZ31 alloy	Improving corrosion resistance	PEO coatings	2015	[105]
Polydopamine-assisted heparinized PEO/PLLA composite	Stents made of biodegradable AZ31 alloy	Improving the corrosion resistance, hemocompatibility, and biocompatibility	Platelet adhesion. HUVEC adhesion. HUASMC adhesion.	2014	[106]
MAO/PLLA	Magnesium alloy stent (WE42 e AM20)	Improving corrosion resistance	The micro-arc oxidation (MAO) and the immersion technique.	2011	[107]–[109]
Poly (L-lactide)(PLLA)	Stainless steel 316LVM stents	Air suspension spray coating technique	–	2010	[110]
Poly (L-lactide)(PLLA)	Nitinol stent	Treating stent restenosis	–	2008	[111]

Magueta, A. [18] studied the interface and adhesion of PLLA films on stainless steel 316 substrates. In this work, it was concluded that the adhesion between the metallic substrate and the polymeric coating was possible through silanization. Silanization is a chemical procedure commonly studied in biomedical applications such as immobilization of peptides on a cardiovascular stent, fabrication of poly(ethylene glycol) (PEG) hydrogel micropatterns, and functionalization of porous silicon (PSi), but never reported in the literature as facilitating the joining of PLLA with stainless steel [112]–[114].

In silanization, the surface of the metal is covered with silanes, forming a layer. This layer can join organic and inorganic materials through molecular bridges at the interface of these two materials [19]. This treatment of the substrates consists of three steps: hydrolysis of silanes, silanization of the oxidized substrate, and thermal curing of the silanized substrate [115].

The silane molecules have two groups: leaving group (X) and functional group (R). The leaving group reacts with the hydroxylated surface of an inorganic material or with other molecules, such as $-\text{CH}_3$ (methoxy) and $-\text{OCH}_2\text{CH}_3$ (ethoxy). The functional group interacts with organic material such as $-(\text{CH}_2)_n\text{CH}_3$ (alkyl), $-(\text{CH}_2)_3\text{NH}_2$, and $-(\text{CH}_2)_2(\text{CF}_2)_5\text{CF}_3$ [116].

A mechanism of silanization on a metallic surface is presented in Figure 11. A hydroxylated surface is immersed in a solution containing n-propyl trimethoxysilane (nPTMS) Figure 11.a. One methoxy group of the nPTMS reacts with a hydroxyl group releasing methanol (Figure 11.b-c). Two methoxy groups in another molecule of the nPTMS will react: one reacts with a hydroxyl group on a metallic surface and the other reacts with a methoxy group from the first nPTMS molecule. It results in a siloxane network structure (SiOSi) and an intermediate layer after thermal curing (Figure 11.d-f) [116][117].

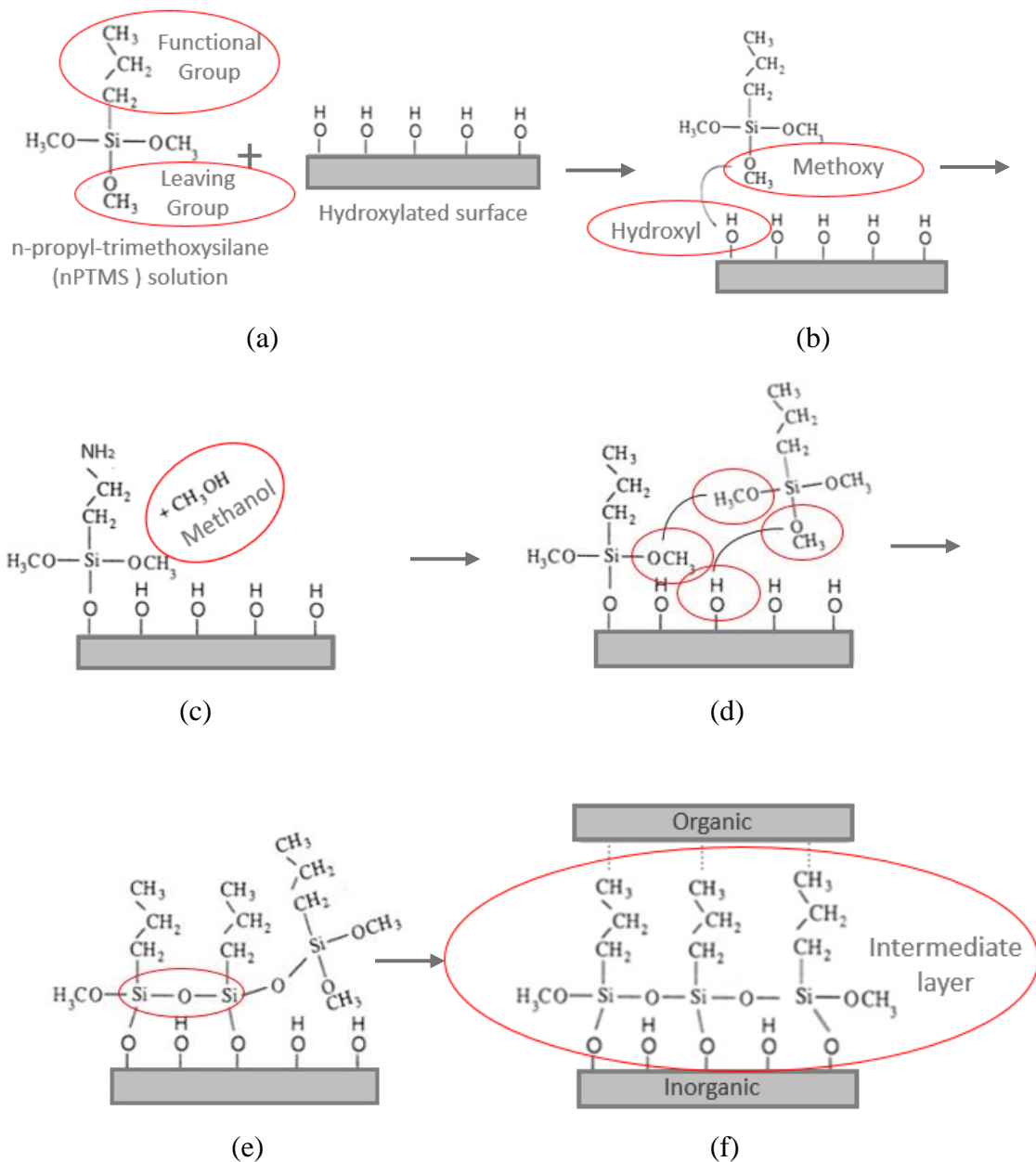


Figure 11. Mechanism of silanization on a metallic surface (based on [116]).

Considering the potential application of metallic devices coated with piezoelectric polymer films to increase the osseointegration, this work continues the research developments started by Magueta, A. The study of cytocompatibility of PLLA coating on SS316L substrate is performed. Structural, physicochemical, electrophysical, and piezoelectric analysis are also under study.

CHAPTER III
MATERIALS AND METHODS

CHAPTER III - MATERIALS AND METHODS

In this chapter, the materials, experimental procedure, and characterization techniques used in this work are described. First, the substrates were thermal treated at 500 °C for 2h and soaked in a silane solution for 1h. A solution of 2.5 wt % of PLLA in 1,4 dioxane was prepared and 3 layers were deposited by spin-coater on the silanized substrates. Next, the coated substrates were characterized. The adhesion of PLLA film to the SS316L substrate was evaluated using the tape test. Electrical and biological characterization was performed, using impedance spectroscopy, Atomic Force Microscopy (AFM), and cytocompatibility tests. Also, other techniques were used to understand better the physical and chemical properties of PLLA film. Fourier Transformed Infrared Spectroscopy (FTIR), X-Ray Diffractometry (XRD), surface roughness analysis, Scanning Electron Microscopy (SEM), contact angle analysis, and Differential scanning calorimetry (DSC) were performed. The experimental procedure is schematically represented in Figure 12 and detailed in the next sections. The abbreviations and illustration of the samples produced in this work are described in Table IX.

This production method was previously defined by Magueta, A [18]. In this work, the adhesion between SS316 and PLLA films as a function of different times of silanization (30, 60, and 90 min), PLLA solution concentration (2.5 and 5.0 wt %), the number of layers deposited (1, 2, and 3) and degree of crystallization (semi-crystalline and crystalline) was addressed. The formation of chromium and iron oxides, after the thermal treatment, was confirmed by FTIR and XPS. Using SEM, XRD, and thermogravimetry, it was verified that the heat treatment (500 °C for 2 h) does not cause surface degradation and changes in the structure and weight percentage of SS316 substrates. The presence of siloxanes was confirmed by FTIR and XPS. Long silanization times leads to the presence of more siloxanes in the substrates. The best time of silanization was 60 min due to the higher contact angle. The SS316 substrates covered with PLLA films melted for 3 min at 180 °C followed by 45 min heat treatment at 120 °C, 2.5 wt % solution, and 3 layers presented the best results in SEM, FTIR, tape test, and degradation in PBS studies [18].

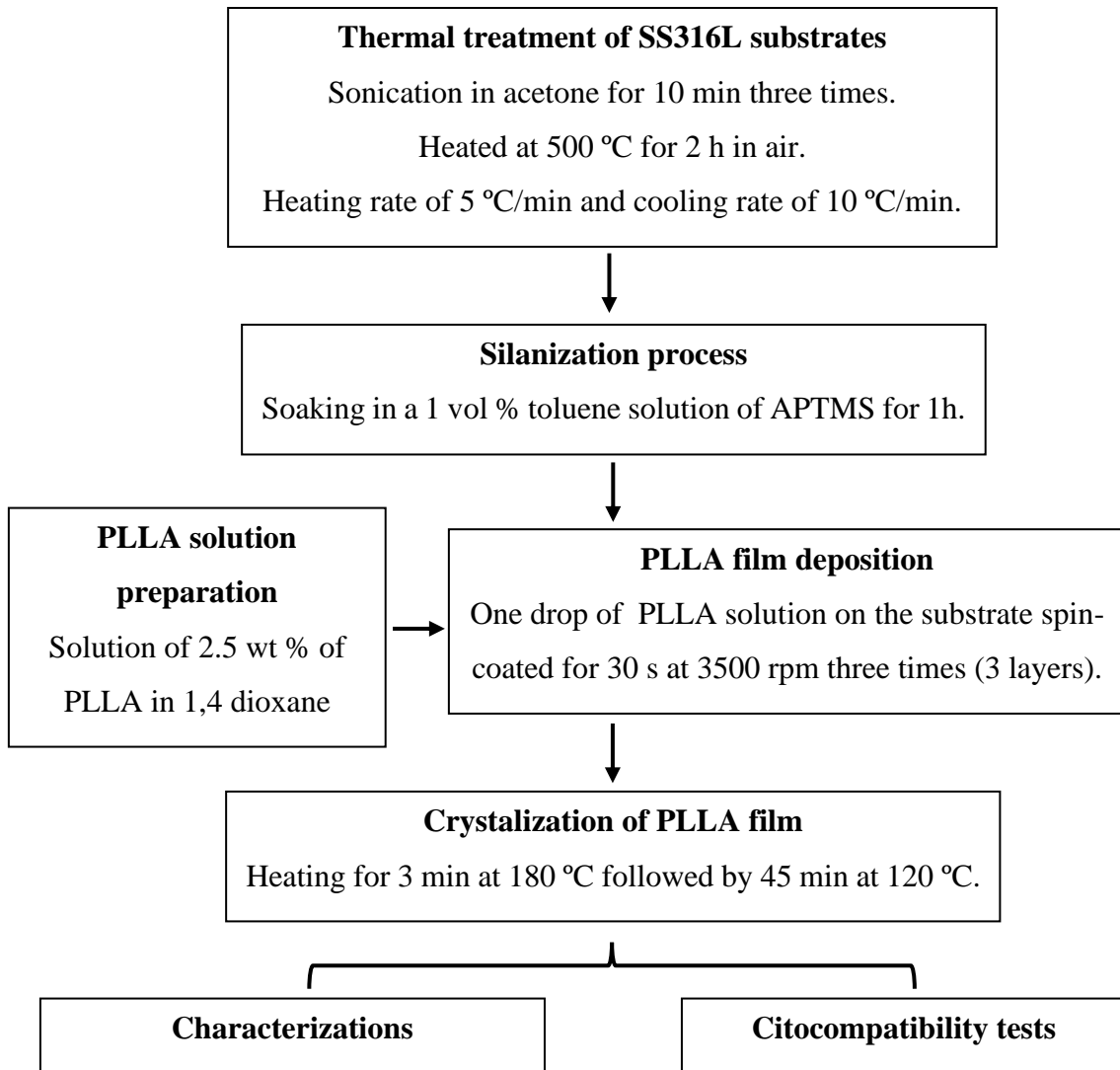



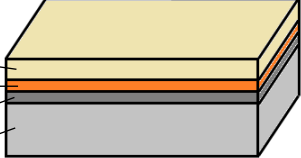


Figure 12. Schematically representation of the experimental process used in this work to develop PLLA coatings on functionalized SS316L substrates.

Table IX. Description of samples.

Abbreviation	Sample Description	Sample Illustration
a) SS316L	<ul style="list-style-type: none"> SS316L without treatments. 	 <p>SS316L</p>
b) SS316L TT	<ul style="list-style-type: none"> Thermal treatment at 500 °C for 2 h. 	 <p>OXIDE SS316L</p>
c) SS316L TT/SIL	<ul style="list-style-type: none"> Thermal treatment at 500 °C for 2 h; Silanization process for 1 h. 	 <p>SILANES OXIDE SS316L</p>
d) SS316L TT/SIL/PLLA	<ul style="list-style-type: none"> Thermal treatment at 500 °C for 2h; Silanization process for 1 h; PLLA film deposition by spin-coating (3 layers); Crystallization process at 180 °C for 3 min followed by 45 min at 120 °C. 	 <p>PLLA SILANES OXIDE SS316L</p>

3.1 Materials

The stainless steel used was AISI 316L (Fe/Cr18/Ni10/Mo3) foil from Goodfellow with 0.38 mm thickness. The foil, measuring 100 x 100 mm, was cut in substrates with 10 x 10 mm. PLLA film solution was prepared using poly (L-lactic acid) from Purasorb® PL 38 (Purac, Netherlands) and 1,4 dioxane (Sigma-Aldrich, 99.8 %). However, silanes solution was prepared using toluene (Riedel-de Haën, 99.7 %) and 3-(Aminopropyl) trimethoxysilane (APTMS) (Sigma-Aldrich, 99.8 %).

3.2 Methodologies

3.2.1 Thermal treatment of SS316L substrates

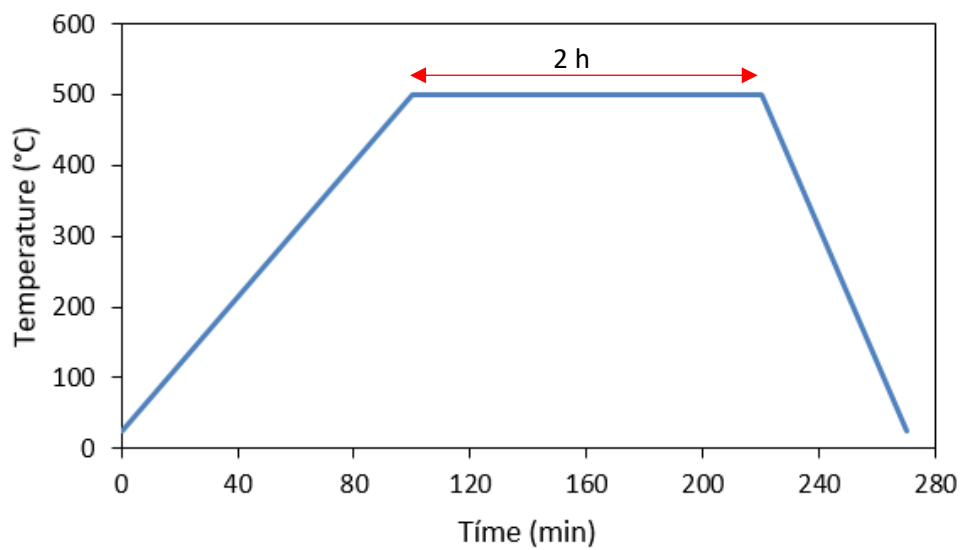
The stainless steel 316L substrates were cleaned by sonicating in acetone for 10 min three times and dried by blowing air (SS316L - Table IX.a). After, the substrates were placed in a ceramic boat (Figure 13.a) and heat-treated at 500 °C for 2 h in air, using

a heating rate of 5 °C/min and a cooling rate of 10 °C/min until room temperature (Figure 13.b). The oven used was Termolab, Fornos Elétricos (Figure 13.c). Samples at this stage are designated by SS316L TT, as presented in Table IX.b).

a)



b)



c)



Figure 13. a) SS316L substrates in a ceramic boat, b) schematic representation of the thermal treatment and c) the oven used.

3.2.2 Silanization of heat-treated SS316L substrates

The SS316L TT samples were soaked in a 1 vol % toluene solution of 3-(Aminopropyl)trimethoxysilane (APTMS) for 60 min in air (pH = 7) using a petri dish (Figure 14). The samples were rinsed with toluene and ethanol and sonicated in ethanol for 5 min. They were dried in air for about 30 min and then dried at 100°C in the oven for 10 min. Samples at this stage are designated by SS316L TT/SIL, as presented in Table IX.c).

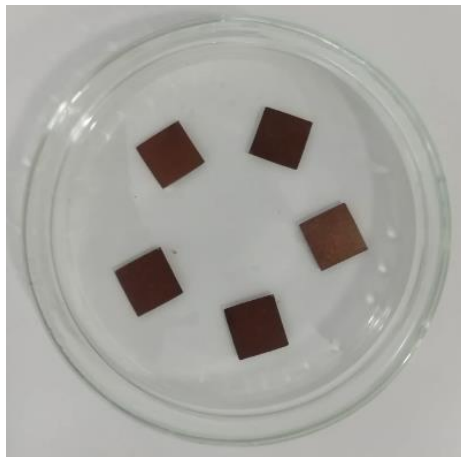


Figure 14. The heat-treated SS316L substrates in a silane solution.

3.2.3 Poly (L-lactic acid) solution preparation

PLLA solution of 2.5 wt % was prepared by dissolving PLLA pellets at 80 °C for 2 h in 1,4 dioxane (Sigma-Aldrich, 99.8 %). To homogenize the solution a thermal stirrer plate, magnetic stirring bar, and silicone oil were used. The temperature was controlled by an electronic contact thermometer with a stainless steel sensor (Figure 15).

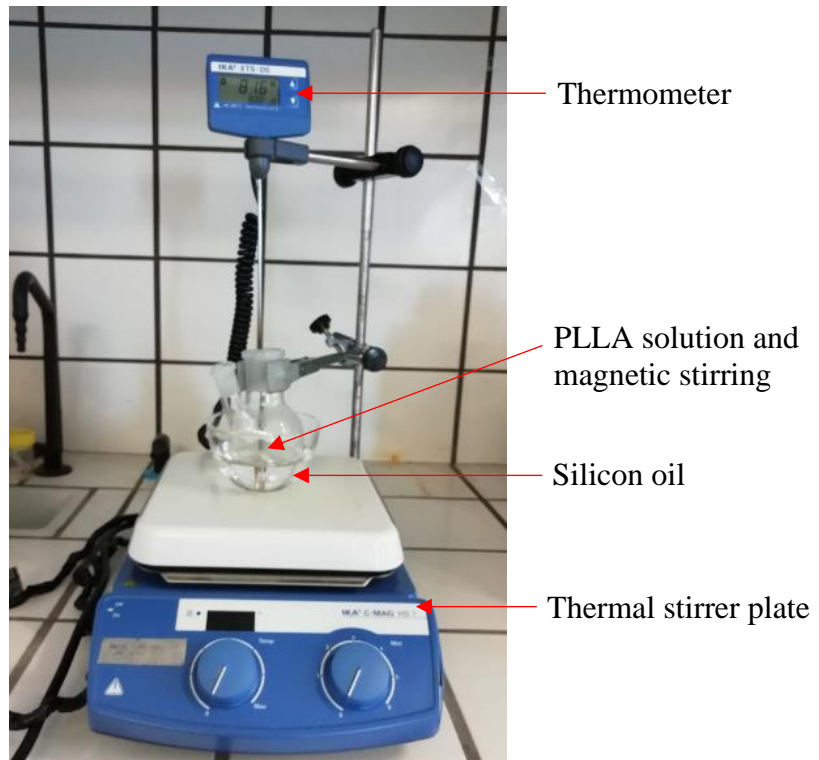


Figure 15. Apparatus used in PLLA solution preparation.

3.2.4 Poly (L-lactic acid) films deposition

The PLLA solution was heated to 45°C using a thermal stirrer plate. One drop (approximately 100 μ L) of this solution was placed on the static SS316L TT/SIL sample and it was spin-coated for 30 s at 3500 revolutions per minute (rpm). This process was repeated three times (3 layers). The spin coater used was from Chemat Technology (Figure 16). Samples at this stage are designated by SS316L TT/SIL/PLLA, as presented in Table IX.d).



Figure 16. Spin-coater used in the PLLA film deposition.

The stages are described below and represented in Figure 17 and Figure 18.

Stage 1: Dispensation (Figure 17.a). Deposition of the fluid on the surface of the static substrate [118].

Stage 2: Acceleration (Figure 17.b): The solution is being spread over the substrate while the spin speed is increasing due to acceleration until the substrate reaches the desired speed [118].

Stage 3: Constant speed with the domination of flow (Figure 17.c): The substrate is spinning at a constant rate and the film thickness is predominantly determined by viscous forces. This stage will last until the flow and evaporation contributions are equal. At this point, the coating becomes thin and dense enough that fluid flow stops. The coating “gels” on the substrate [118].

Stage 4: Constant speed with the domination of evaporation (Figure 17.d): The substrate is spinning at a constant rate and the film thickness is predominantly determined by solvent evaporation. This stage will last until the spinning stops and the films become uniform and thin (Figure 17.e) [118].

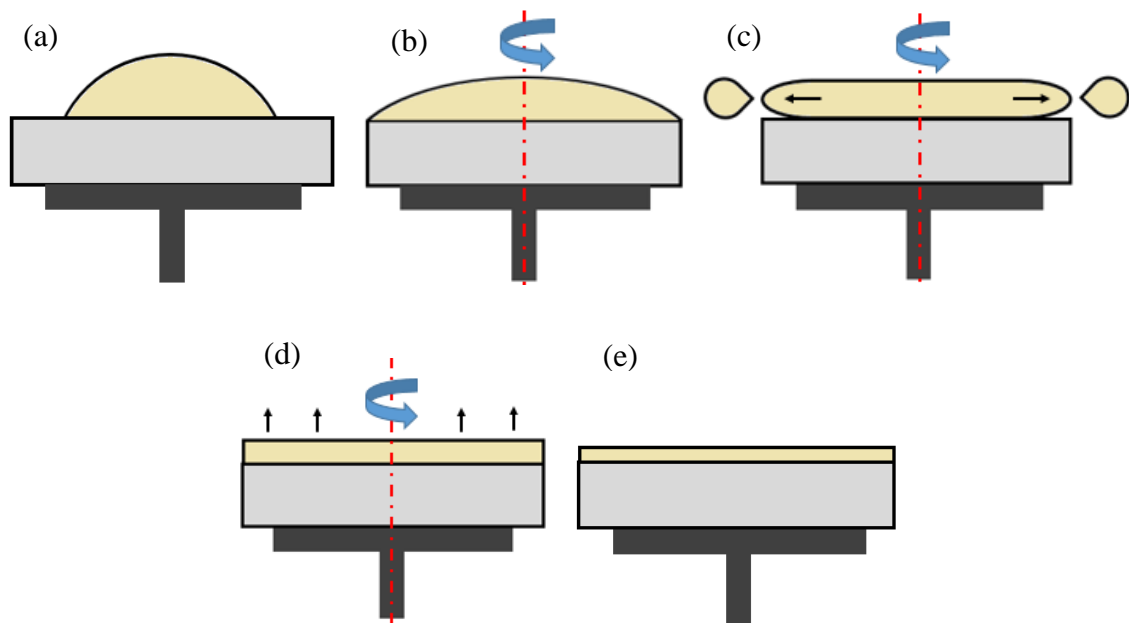


Figure 17. Spin coating process (based on [119]).

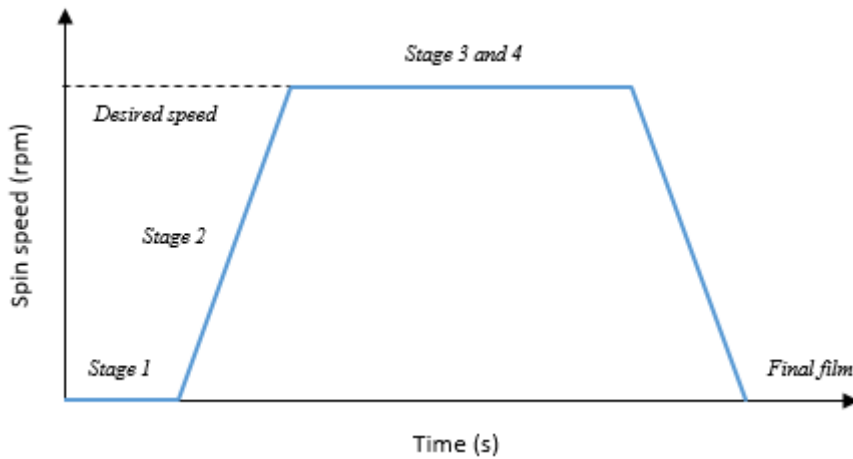


Figure 18. Stages of the spin coating process (based on [119]).

3.2.5 Crystallization process of Poly (L-lactic acid) films

In order to promote the PLLA crystallization. The silanized SS316L covered with PLLA films were heated on a thermal stirrer plate for 3 min at 180 °C, followed by a 45 min period at 120 °C (Figure 19). The temperature of 120°C was used once it is above the PLLA glass transition temperature (T_g), while 180 °C was used since it is above the melting temperature (T_m), as will be later discussed.

a)

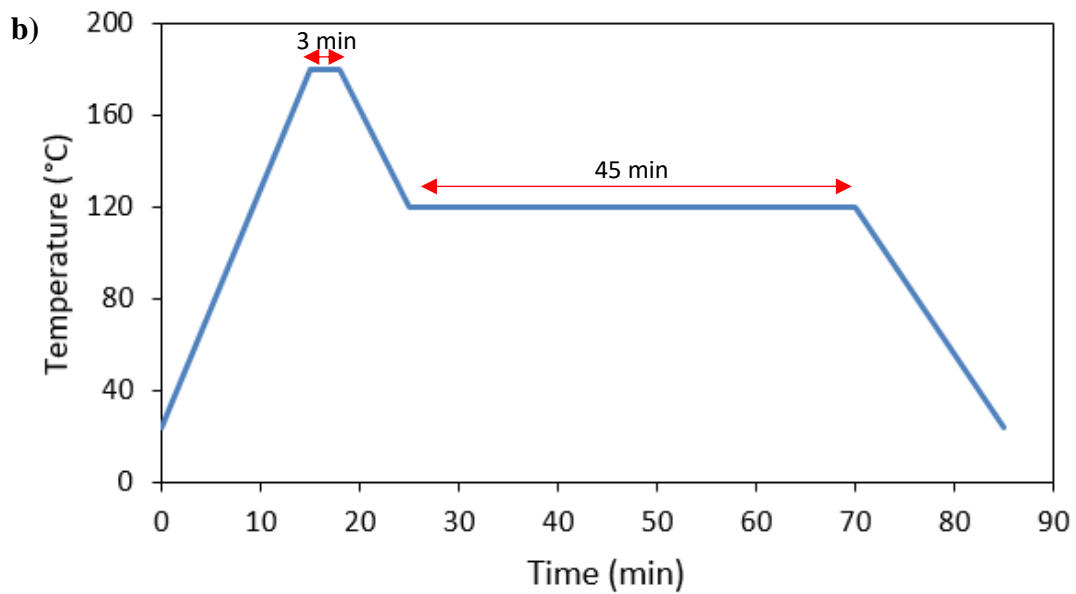


Figure 19. a) Crystallization of coated substrates on thermal stirrer plate and b) crystallization process schedule.

3.3 Characterization techniques

The techniques used for the characterization of the samples are presented in the following sections.

3.3.1 Fourier Transformed Infrared Spectroscopy (FTIR)

The chemical composition identification of molecules and substances on SS316L TT, SS316L TT/SIL, and SS316L TT/SIL/PLLA samples were studied by FTIR. Relevant peaks should be related to the presence of oxides like chromium oxide (Cr_2O_3) on SS316L TT, siloxanes on SS316L TT/SIL, and organic molecules (CH, CH_3 , C=O, C-O-C, etc) on SS316L TT/SIL/PLLA. The transmittance percentage was recorded as a function of the wavenumber in the range 3150 to 350 cm^{-1} . The spectroscopy equipment utilized was Thermo-Nicolet Nexus 670 FTIR (Thermo Scientific, USA).

FTIR is a vibrational spectroscopic technique in which the Fourier transform method is used to obtain an infrared spectrum in a whole range of wavenumbers. In this technique, the infrared radiation from a source enters an interferometer composed of one beam-splitter and two mirrors. The beam-splitter transmits half of the infrared (IR) beam from the source to the fixed mirror and reflects the other half to the moving mirror. These mirrors reflect the beams and the two split beams combine at the beam-splitter again. The combined beams pass through the sample and are received by a detector (Figure 20). The function of the moving mirror is to change the optical path lengths to generate light interference between the two split beams [120].

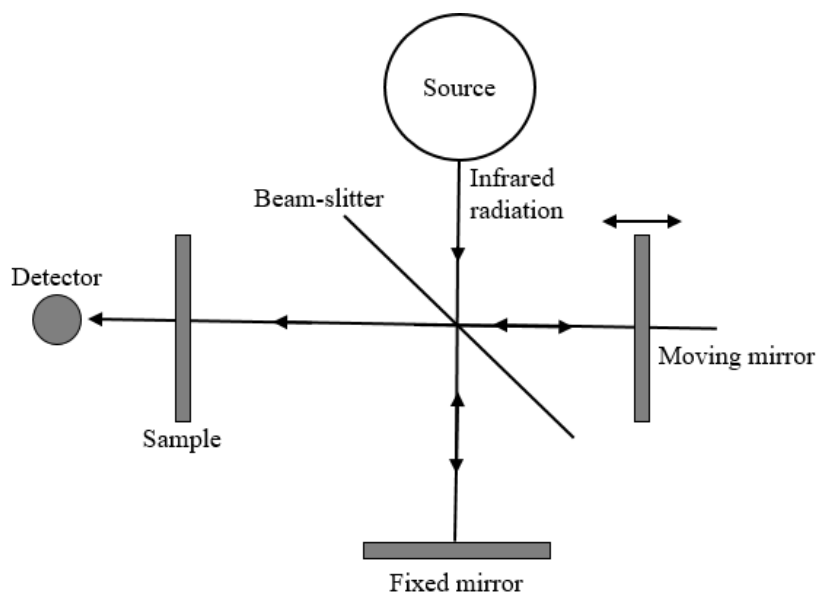


Figure 20. Optical diagram of FTIR [120].

A plot of light interference intensity as a function of optical path difference is called an interferogram. The FTIR detector receives interferogram signals which are transmitted to a sample or reflected from a sample. The Fourier transform converts the intensity versus optical path difference into the intensity versus wavenumber (infrared spectrum). The spectrum can also be presented as transmittance or absorbance. Transmittance (T) is defined as the ratio of intensities (Equation 6), where I is the intensity measured in a single beam spectrum of a sample and I_0 is the intensity measured in the background spectrum. Nevertheless, the absorbance (A) is calculated from the transmittance (Equation 7). The vibration band peaks point downward in a transmittance spectrum and upward in an absorbance spectrum [120].

$$T = I / I_0 \quad \text{Equation 6}$$

$$A = - \log T \quad \text{Equation 7}$$

3.3.2 X-Ray Diffractometry (XRD)

The crystallographic planes and compounds of SS316L, SS316L TT, and SS316L TT/SIL/PLLA samples were studied by XRD. The crystal structure between SS316L before and after the thermal treatment was compared. The crystal structure of crystallized PLLA films was also studied. The diffraction angle studied was 2θ from 5 to 100° and the diffractometer used was Panalytical Xpert PRO3.

XRD is an X-ray diffraction technique, which an X-ray beam of a single wavelength is used to identify the crystal structure of polycrystalline specimens. A spectrum of diffraction intensity versus the angle between the incident and diffraction beams is recorded by changing the incident angle of the X-ray beam [120].

In this technique, the X-ray radiation generated by an X-ray tube passes through a divergent slit, which collimates the X-ray beam. Divergent X-ray beams strike the specimen and are diffracted by it. The diffracted X-ray beams pass through a convergent slit and form a convergent beam. Before hitting a detector, the beam passes through a monochromator to suppress wavelengths and decrease background radiation originated within the specimen (Figure 21). Relative movements among the X-ray tube, specimen, and the detector ensure the recording of diffraction intensity in a range of 2θ , where θ is the angle between the incident beam and the crystallographic plane that generates diffraction [120].

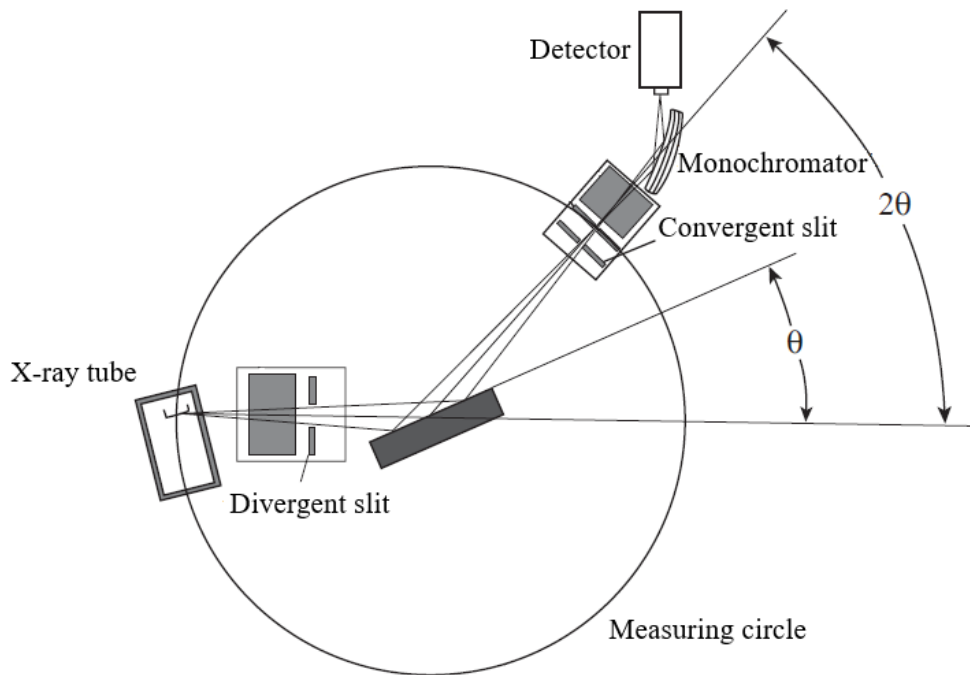


Figure 21. The geometric arrangement of X-ray diffractometer (adapted from [120]).

3.3.3 Surface roughness analysis

The surface roughness of SS316L, SS316L TT, SS316L TT/SIL, and SS316L TT/SIL/PLLA samples was studied to analyze the influence of thermal treatment, silanization, and film deposition on the microtopography of the samples. The parameters studied were arithmetic mean roughness (R_A), maximum roughness depth (R_{MAX}), and mean roughness depth (R_Z). A Hommel Tester T1000 rugosimeter was used following standard ISO 4287:1997 [121]. The measure conditions are described in Table X. The PLLA film thickness was also calculated from the roughness measurements.

Table X. Surface roughness measurement conditions.

Parameters	Conditions
Pick-up type	TK300
Measurement range / resolution	320,0 μm
Transverse length (L)	4,8 mm
Cut-off (L_x)	0,8 mm
Transverse speed (V)	0,5 mm/s

Surface texture is the repetitive or random deviation from the nominal surface that forms the three-dimensional topography of the surface, including roughness, waviness, lay, and flaws. Surface roughness refers to the variations in the height of the surface relative to a reference plane [122].

The mechanical stylus method records the vertical motions of a stylus displaced at a constant speed by the surface to be measured. The stylus arm is loaded against the sample. As the stylus moves, it rides over the surface detecting deviations. It produces an analog signal corresponding to the vertical stylus movement. This signal is then amplified, conditioned, and digitized (Figure 22) [122].

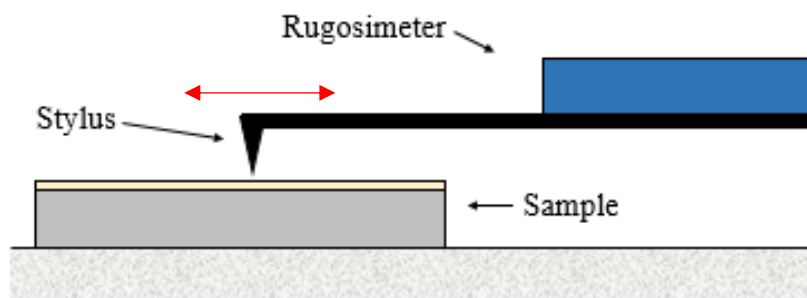
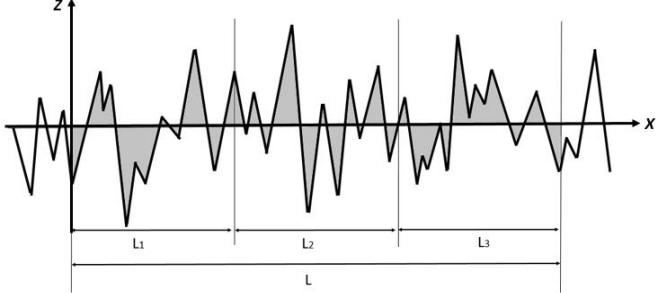
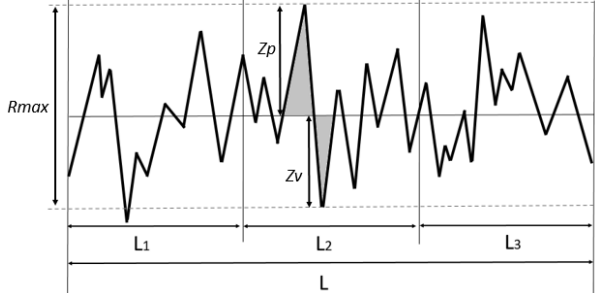
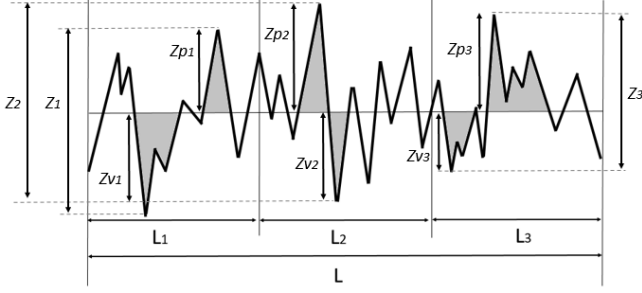


Figure 22. Rugosimeter (based on [122]).

Some important parameters are arithmetic mean roughness (R_A), maximum roughness depth (R_{MAX}), and mean roughness depth (R_Z). The arithmetic mean roughness (R_A) is the arithmetical mean of the absolute values of the profile deviations $Z(x)$ from the mean line within the transverse length (L). The maximum roughness depth (R_{MAX}) is the largest single roughness depth within the transverse length (L). On the other hand, the mean roughness depth (R_Z) is the mean value of the sum of the maximum peak height Z_p and the maximum valley depth Z_v within all cut-off (L_x). R_A provides stable results as the parameter is not significantly influenced by scratches, contamination, and measurement noise. Moreover, R_{MAX} and R_Z are significantly influenced due to their utilization of peak values [123][124]. The mathematical definition and graphic representation of these parameters are shown in Table XI.

Table XI. Surface roughness measurement. Parameters representation.

Mathematical definition	Graphic representation
$R_A = \frac{1}{L} \int_0^L Z(x) dx$ <p>Equation 8</p>	
$R_{MAX} = Z_P + Z_V$ <p>Equation 9</p>	
$R_Z = \frac{1}{n} (\sum_{i=1}^n Z_{pi} + Z_{vi})$ <p>Equation 10</p> $R_Z = \frac{1}{3} [(Z_{p1} + Z_{v1}) + (Z_{p2} + Z_{v2}) + (Z_{p3} + Z_{v3})]$	

It is possible to measure the thickness of films on a substrate, through the roughness on a sample without a piece of film, using the maximum roughness depth (R_{MAX}) (Figure 23). For this purpose, one must consider that this difference of height is the largest single roughness depth within one sample.

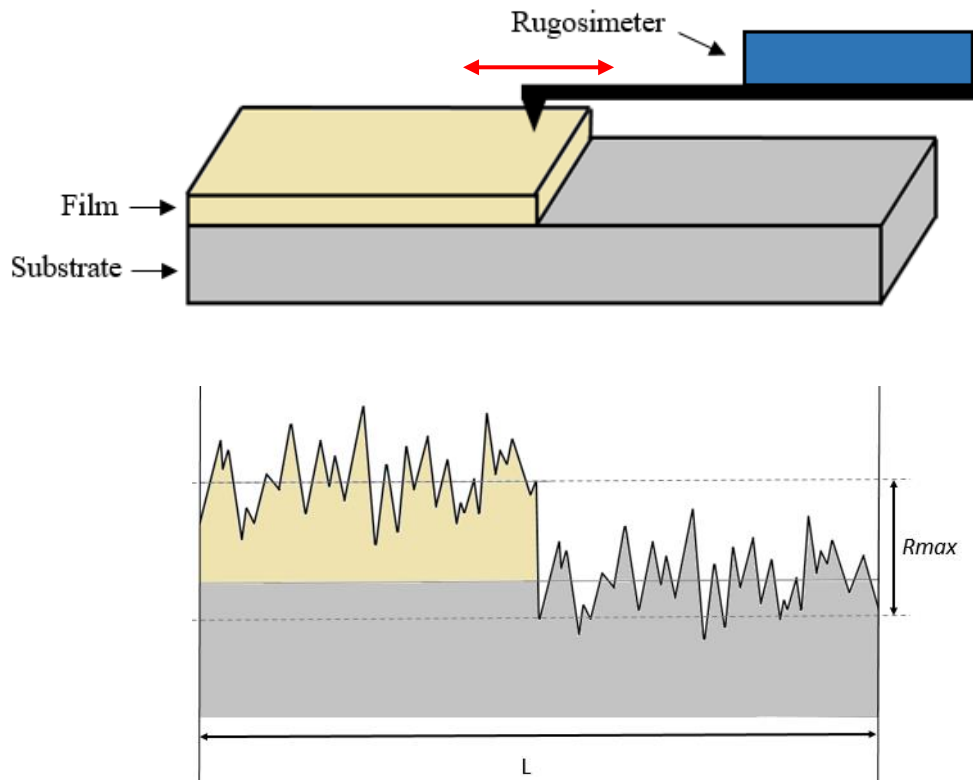


Figure 23. The measure of the thickness films on the substrate using a rugosimeter (based on [123][124]).

3.3.4 Microstructural studies by Scanning Electron Microscopy (SEM)

The morphology and microstructure of the surface of SS316L TT/SIL/PLLA samples were studied by SEM. Three micrographs with different magnifications (100, 500, and 1000 x) were obtained and the average grain size was calculated from 328 spherulites of the crystallized PLLA films using ImageJ software. A Hitachi SU70 microscope was used working under the electron acceleration field of 5 kV. Before the test, a layer of carbon was deposited on the PLLA films.

SEM examines the sample microstructure by a focused electron beam that scans over the surface area. The electron gun emits an electron beam that passes through several electromagnetic lenses, including condenser lenses and one objective lens for electron probe formation. The two condenser lenses reduce the diameter of the electron beam and the objective lens focuses the electron beam. The signal electrons emitted from the samples are collected by a detector, amplified, and used to reconstruct an image (Figure 24) [120].

Probe scanning is operated by a beam deflection system incorporated within the objective lens and composed of two pairs of electromagnetic coils (scan coils). The

deflection system moves the probe over the sample surface along a line and then displaces the probe to a position on the next line for scanning so that a rectangular raster is generated on the specimen surface [120].

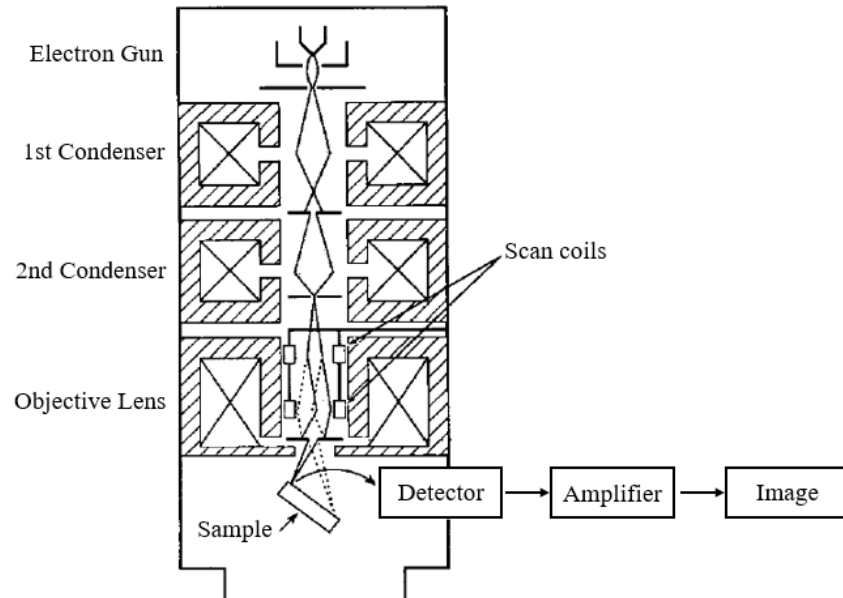


Figure 24. Structure of an SEM (adapted from [120]).

3.3.5 Film adhesion by Tape test

The adhesion of PLLA films to the SS316L substrates was evaluated using a pressure-sensitive tape (Elcometer 99). The test was performed in three substrates and, after the test, those substrates were observed using an optical microscope (Nikon Microphot – Infinity) and a scanning electron microscope (Hitachi SU70) under a 5 kV electron acceleration field. A 3D printed plastic accessory was made to help the cutting process (Figure 25.d).

The tape test is used to evaluate the adhesion of a coating to a substrate and is described in standard ASTM D3359 [125]. This standard mentions two test methods and method B is the most suitable for this study. This method consists of making a lattice pattern with six cuts in each direction (perpendicular) through the film until the substrate using a sharp cutting device (x-acto knife) positioned at a cutting angle between 15 and 30°. A distance of 1 mm is kept between cuts (Figure 25.a). About 75 mm of pressure-sensitive tape is applied over the substrate and a pressure application device (rubber eraser) is used to apply pressure to ensure good and uniform wetting of the coating with

the adhesive of the tape (Figure 25.b). The dwell time of the tape over the substrate is 60 s. After that, the tape is removed rapidly as close to the angle of 180° as possible (Figure 25.c). The test area is examined using an optical microscope and adhesion is assessed qualitatively on a 0 to 5 scale, according to Table XII [125].

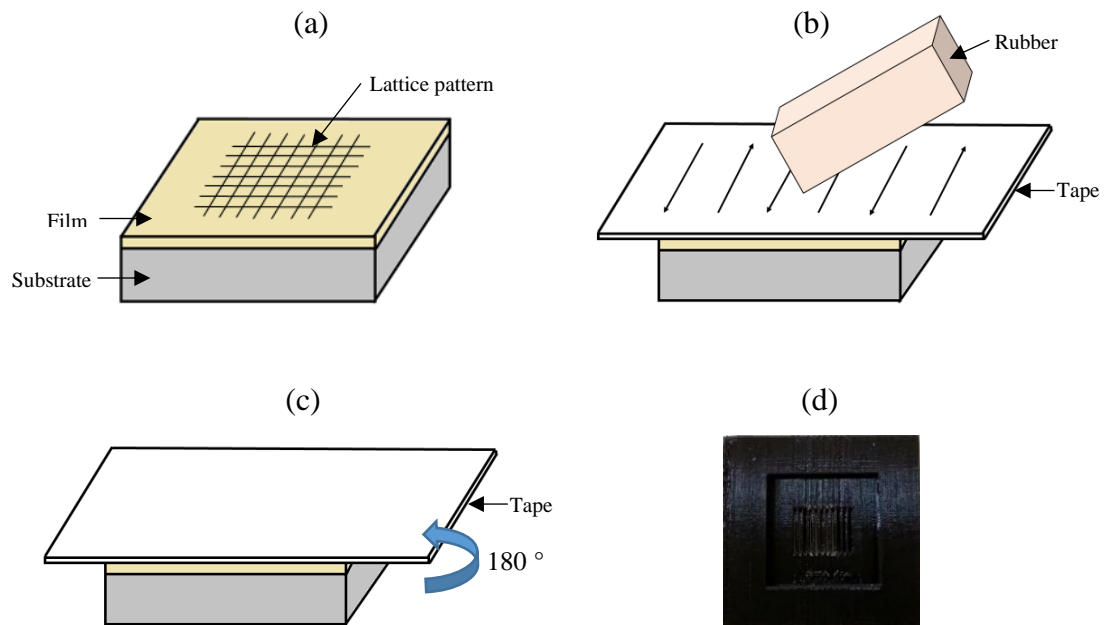
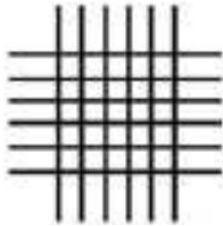
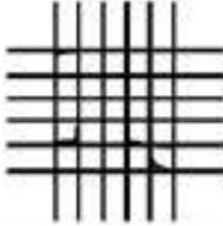
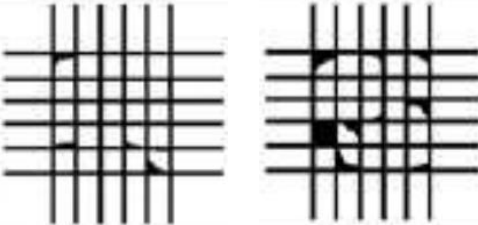
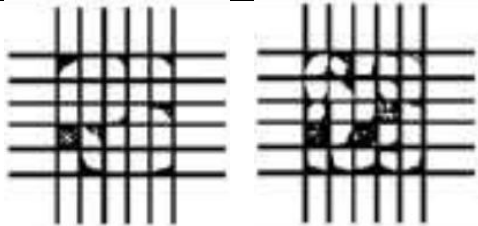
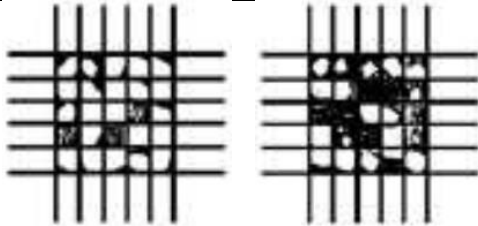
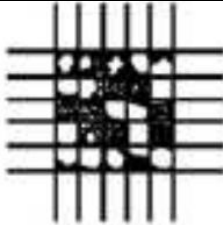


Figure 25. a-c) Tape test process and d) 3D printed plastic accessory.

Table XII. Classification of tape test results according to standard ASTM D3359 [125].

Classification	Percent area removed	Surface of cross-cut area
5B	0 % None	
4B	Less than 5 %	
3B	5 – 15 %	
2B	15 – 35 %	
1B	35 – 65 %	
0B	Greater than 65 %	

3.3.6 Contact angle analysis

The wettability and the surface energy of the SS316L TT/SIL/PLLA samples were studied by measuring the contact angle of the PLLA films with water and diiodomethane drops. The contact angle of ten drops of each liquid, on four samples, was measured, using the system OCA 20 (Dataphysics). The system's syringe was filled with the liquids and the system was programmed to dispense 3 μL drops, automatically. For each measurement, the system recorded the result using an integrated camera, and the data was processed using the SCA20_M4 software (Dataphysics).

The wettability of a liquid on a solid surface depends on chemical and geometrical factors. The chemical factor depends on the molecular interaction with the solid material, the liquid material, and the solid/liquid interface. It is important for the macroscopic characterization of the surface. The geometric factor represents the shape (roughness) of a solid surface and contributes to the understanding of the microscopic phenomena [126].

The wettability can be represented quantitatively by the contact angle θ , outlined in Figure 26, and expressed by Equation 11 (Young's equation), where γ_S is the tension of solid, γ_L is the tension of the liquid, and γ_{SL} is the interfacial tension. When $\theta < 90^\circ$, the surface is hydrophilic, and when $\theta > 90^\circ$, it is hydrophobic [126].

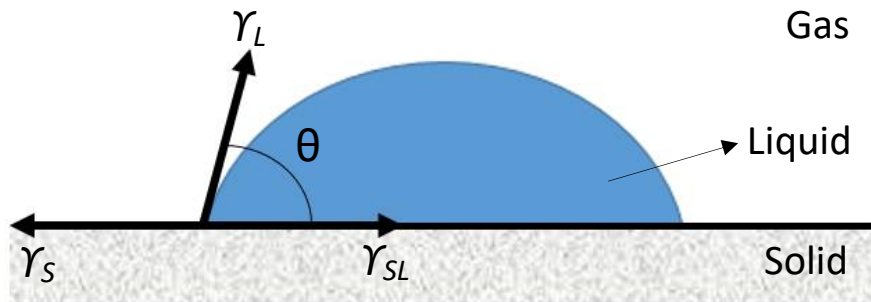


Figure 26. Wettability of a liquid droplet on a solid surface (based on [126]).

$$\gamma_S = \gamma_{SL} + \gamma_L \cos \theta \quad \text{Equation 11}$$

To determine the surface energy of a solid (γ_S), one can apply the OWRK-model from Owens, Wendt, Rabel, and Kaelble (Equation 12). This model considers that the surface tension consists of a nonpolar or dispersive component (γ^d) and a polar component (γ^p) [126][127].

$$\gamma_{SL} = \gamma_S + \gamma_L - 2 \left(\sqrt{\gamma_S^d \gamma_L^d} + \sqrt{\gamma_S^p \gamma_L^p} \right) \quad \text{Equation 12}$$

Substituting Equation 12 in Equation 11, a linear equation of the type $y=m.x+c$ can be obtained (Equation 23).

$$\frac{\gamma_L (1 + \cos \theta)}{2\sqrt{\gamma_L^d}} = \sqrt{\gamma_S^p} \cdot \sqrt{\frac{\gamma_L^p}{\gamma_L^d}} + \sqrt{\gamma_S^d} \quad \text{Equation 13}$$

The contact angles of two liquids are measured. The nonpolar (γ_L^d) and polar components (γ_L^p) of these liquids must be known in the literature. Considering $\gamma_L = \gamma_L^d + \gamma_L^p$, $y = \frac{\gamma_L (1 + \cos \theta)}{2\sqrt{\gamma_L^d}}$ and $x = \sqrt{\frac{\gamma_L^p}{\gamma_L^d}}$, it is possible to define one point for each liquid, (x_1, y_1) and (x_2, y_2) . With these two points expressed in a graphic, a regression line is created. The $m = \sqrt{\gamma_S^p}$ and $c = \sqrt{\gamma_S^d}$ are obtained from the equation. Then, $\gamma_S = \gamma_S^d + \gamma_S^p$ is determined. Generally, the use of diiodomethane, ethylene glycol, and thiodiglycol as test liquids yields good results

3.3.7 Differential scanning calorimetry (DSC)

The thermal properties (phase transitions and degree of crystallization) of the PLLA films were studied using DSC. The experiments were performed in duplicate at a heating/cooling rate of ± 10 °C/min from room temperature to 200 °C under airflow.

The differential scanning calorimetry (DSC) is a thermal analysis used to measure the energy changes that occur while a sample is heated or cooled. The energy changes are related to the phase transitions during the heating (T_g , T_m) and the cooling (T_c). For polymeric materials, the glass transition (at T_g) is an endothermic event in which the mobility of the amorphous regions of a semi-crystalline material occurs. The melting temperature (T_m) is an endothermic event in which the crystalline regions melt. The crystallization temperature (T_c) is an exothermic event in which the polymer chains are organized forming a crystalline structure [128][32].

The DCS equipment records the heat flow (J/s) as a function of temperature and time, and it consists of a heater, heat sink, heat resistor, and thermocouple (Figure 27).

The heat from the heater is transferred to the sample and the reference through the heat sink and heat resistor. The temperatures of the sample and the reference are the same and are controlled by a thermocouple. The heat flow is proportional to the heat difference between the heat sink and the materials [129].

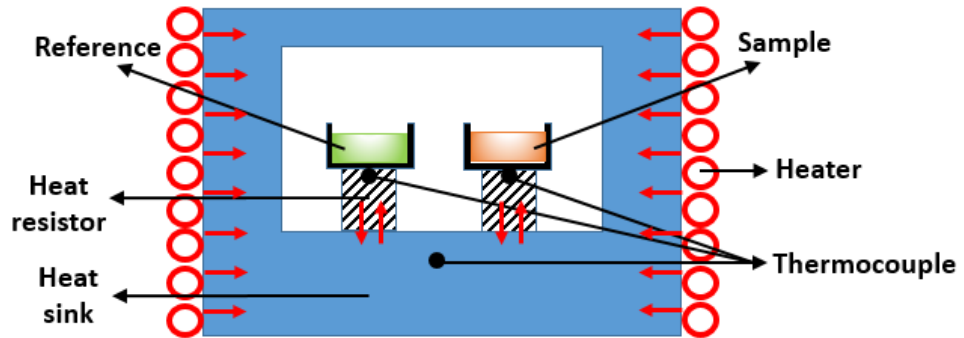


Figure 27. Principle of DSC technique (Based on [129]).

The degree of crystallinity of the material can be estimated from Equation 14, where ΔH_f is the specific enthalpy of fusion (J/g) of the sample determined from the peak area in a DSC graphic, and ΔH_f^0 is the enthalpy of fusion of a 100 % crystalline material, found in the literature [32].

$$X_c (\%) = \frac{\Delta H_f}{\Delta H_f^0} \times 100 \quad \text{Equation 14}$$

3.3.8 Dielectric characterization

The resistivity (ρ), dielectric permittivity (ϵ), and dielectric loss tangent ($\tan(\delta)$) were determined, as a function of frequency and temperature, using impedance spectroscopy. The Linkam THMS600 equipment was used to control the temperature and the Agilent E4980A precision LCR meter was used to measure the electric properties. The measurements were performed under the conditions described in Table XIII. A gold electrode, with 1.5 mm of diameter, was deposited on the PLLA film's surface before the test.

Table XIII. Impedance measurement conditions.

Parameters	Conditions
Temperature range	120 °C to 24 °C (cooling)
Frequency range	1 kHz to 100 kHz
Heat rate	2 °C/min
Tension applied	100 mV
Bias	0 V
Sweeps interval	10 s

The response of materials to an electrical input can be classified by their abilities to conduct a current, that is, electrical conductivity (σ) or resistivity (ρ), respectively. They are divided into conductors, semiconductors, and insulators (dielectrics). The determination of the conductivity under a direct current (DC) is made using Equation 15, where R is the resistance, l length, w width, and d thickness of the material. Electrical resistivity is the inverse of conductivity and is represented by Equation 16 [130].

$$\sigma = \frac{l}{Rwd} \quad \text{Equation 15}$$

$$\rho = \frac{1}{\sigma} \quad \text{Equation 16}$$

The resistance is calculated according to Ohm's law (Equation 17), in which I is the current and U is the voltage.

$$R = \frac{U}{I} \quad \text{Equation 17}$$

The dielectric properties of materials are used to describe electrical energy storage, dissipation, and transfer. Electrical storage is the result of dielectric polarization that causes charge displacement or rearrangement of molecular dipoles. The loss of energy is eventually related to scattering, radiation, or electrical energy conversion into thermal energy (Joule heating). Energy transfer is related to the propagation of electromagnetic waves in dielectric media, transmission lines, and waveguides [130].

Dielectric polarization P is calculated using Equation 18, where D is the dielectric displacement, originated from the response of the material to an external electric field E , and ϵ_0 is the dielectric permittivity of free space (8.854×10^{-12} F/m) [130].

$$P = D - \epsilon_0 E \quad \text{Equation 18}$$

Dielectric permittivity (ϵ) is a measure of the electric polarizability of a dielectric material. It is defined as a complex quantity (Equation 19), as it contains real and imaginary parts, where ϵ' is the real permittivity (dielectric constant), ϵ'' the imaginary permittivity (dielectric loss), and i the complex number. The real part is related to the sample polarization, while the imaginary part is related to the dielectric loss of the material. However, the relative permittivity (ϵ_r) is a dimensionless ratio of complex permittivity (ϵ) to the permittivity of free space (ϵ_0), presented in Equation 20 [130].

$$\epsilon = \epsilon' - i\epsilon'' \quad \text{Equation 19}$$

$$\epsilon_r = \frac{\epsilon}{\epsilon_0} \quad \text{Equation 20}$$

There is energy dissipation in all-dielectric materials. This loss of energy can be quantified by dielectric loss tangent ($\tan(\delta)$) which can be calculated by Equation 21 [130].

$$\tan(\delta) = \frac{\epsilon''}{\epsilon'} \quad \text{Equation 21}$$

The complex dielectric permittivity depends on temperature, frequency, and direction of the electric field vector E , in the case of anisotropic materials. That frequency dependence indicates a dielectric relaxation originated from redirected responses of electric dipoles to the applied electric field [130].

3.3.9 Atomic force microscopy (AFM)

The topography, electrophysical (surface potential, electric field, and capacitance distributions), and piezoelectric properties were studied in PLLA films using the AFM technique. Commercial AFMs (Ntegra Prima NTMDT and Agilent 5000) were used in

Electrostatic Force Microscopy (EFM), Kelvin Probe Force Microscopy (KPFM), and Piezoresponse Force Microscopy (PFM) modes.

The AFM uses the atomic forces to map the tip-sample interaction in order to study the topographic, chemical, electrophysical, and magnetic properties of the material. While a tip in the cantilever traces the surface, the contact force causes the bending of the cantilever, and then the laser is reflected from the back of a cantilever to the detector. The cantilever bends to accommodate changes in topography. The laser position on the detector is used to track the surface for imaging and measuring. The scheme of the AFM technique is shown in Figure 28.

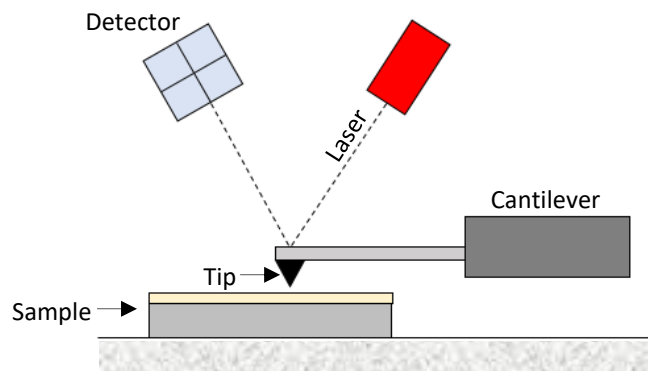


Figure 28. AFM technique representation.

The contact force is not measured directly but calculated by measuring the deflection of the cantilever using Hooke's law (Equation 22), where F is the force, k is the stiffness of the cantilever, and z is the distance that the cantilever is bent [131].

$$F = -kz \quad \text{Equation 22}$$

The force can be studied by the Van der Waals curve (Figure 29). At the right side of the curve, the atoms are separated by a large distance. Going to the left side of the curve, the atoms are gradually brought together and they attract each other. This attraction increases until the atoms are so close that their electron clouds begin to repel themselves electrostatically. This electrostatic repulsion progressively weakens the attractive force to zero and increases the repulsive force. When the total van der Waals force becomes positive, the atoms are in contact. In AFM, this means that when the cantilever pushes the

tip against the sample, the cantilever bends rather than forcing the tip atoms closer to the sample atoms [131][132].

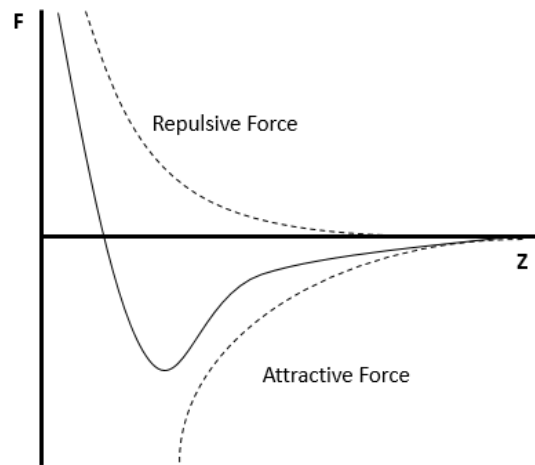


Figure 29. Van der Waals curve. Atomic Force versus probe distance from a sample (based on [131][132]).

The AFM modes are classified by imaging modes and electrophysical modes. These modes are explained in the topics below.

Imaging modes

The imaging modes are contact and dynamic mode (non-contact and tapping mode). The difference between them is the probe distance from a sample, represented in Figure 30.

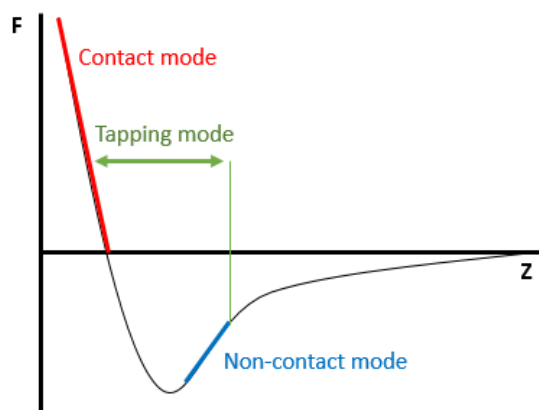


Figure 30. Imaging modes representation. Atomic Force versus probe distance from a sample. (based on [131][132]).

In the contact mode, the tip is in the repulsive regime and touches the surface of the sample. There are two methods of imaging: constant force or constant height. In constant force, the cantilever deflection is constant while the vertical tip position changes. As in constant height, the vertical tip position is constant while cantilever deflection changes. The results of this mode are topography and frictional force. The frictional forces on a surface are obtained by measuring the lateral twist of the cantilever [131][132].

The non-contact and tapping modes are dynamic modes where there is cantilever oscillation. In the non-contact mode, the tip is quite close to the sample but does not touch it. The cantilever oscillates in the attractive regime and the detection scheme is based on measuring changes to the resonant frequency or amplitude of the cantilever. However, in the tapping mode, the cantilever oscillates closer to the sample between the contact and non-contact modes; hence, there are attractive and repulsive forces. The tip taps the surface intermittently. This mode improves the lateral resolution on samples because lateral forces such as drag are eliminated. The results of dynamic mode are topography and phase [131].

Phase imaging refers to the monitoring of the phase lag ($\Delta\theta$) between the input and output signal in the cantilever (Figure 31). The phase-contrast can be correlated with specific material properties that affect the tip/sample interaction. The phase shift can be used to differentiate areas in a sample with different physical and chemical properties such as friction, adhesion, and viscoelasticity [131][132].

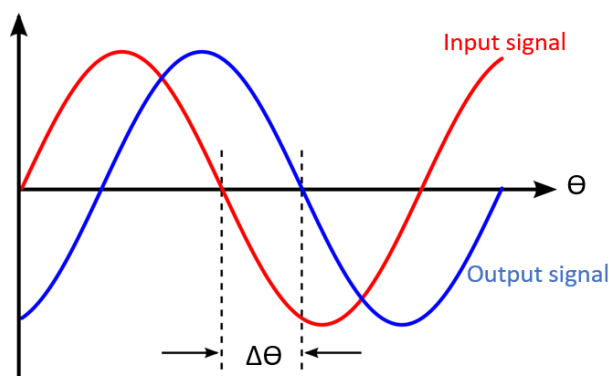


Figure 31. Phase lag measure (based on [131]).

Electrophysical modes

Electrostatic Force Microscopy (EFM)

A voltage is applied between the conducting tip and the sample while the tip oscillates on the surface in two passes (Figure 32). The first scan is performed to obtain the topography by scanning the tip near the sample surface in the non-contact mode where the van der Waals forces are dominant. The second scan is performed to obtain electric force gradients. The system lifts the tip and increases the tip-sample distance in order to place the tip in the region where electrostatic forces are dominant. The results of EFM are topography, surface potential, and charge distribution. Using the phase signal, an electric field gradient map is created. The magnitude of the deflection is proportional to the charge density [131][132].

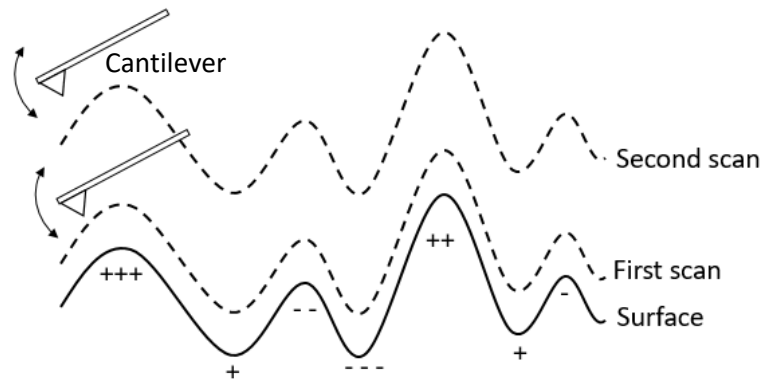


Figure 32. Scheme of EFM operation (based on [132]).

Kelvin Probe Force Microscopy (KPFM)

Like EFM, a voltage is applied between the conducting tip and the sample while the tip oscillates on the surface in a tapping mode (Figure 33). First, an AC voltage (alternating current) with a frequency (ω) is applied to the cantilever during its pass, creating an oscillating electrostatic force between tip and sample. Then, a DC voltage (direct current) is applied to null the potential, prevent cantilever oscillation, and turns ω term into zero. Then, this applied DC voltage is mapped as a measure of the difference in electrical potential and as a work function between tip and sample. Work-function is defined in solid-state physics as the energy needed to remove an electron from the Fermi level in a solid under vacuum. It is a property of the surface, not the bulk. Then, this technique can measure the surface potential and work function of the surface [132].

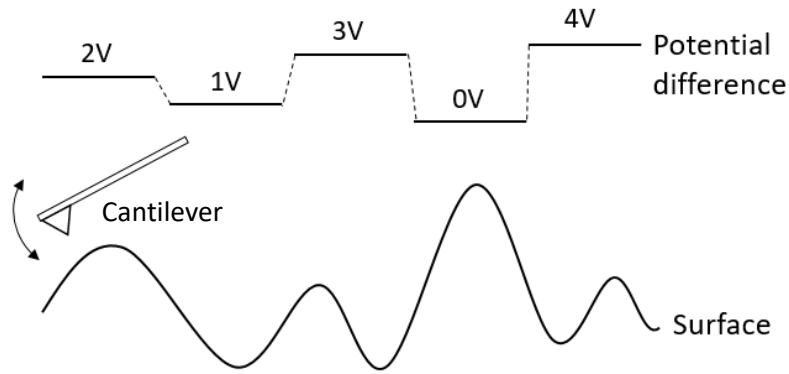


Figure 33. Scheme of KPFM operation (based on [132]).

Piezoresponse Force Microscopy (PFM)

This technique is a contact-mode in which a voltage is applied to the conductive tip while the piezoelectric sample expands and contracts (mechanical deformation) due to the converse piezoelectric effect. The tip deflects due to the mechanical deformation of the sample. This method simultaneously measures the vertical piezoresponse signal (out-of-plane response) and the lateral one (in-plane response). The amplitude provides information about the magnitude of the local electromechanical coupling, while the phase image gives local polarization orientation [132].

The domain expansion occurs if the initial polarization (P) of the piezoelectric domain is perpendicular to the sample surface and parallel to the applied electric field (E). Since the AFM tip is in contact with the sample surface, such domain expansion would bend the AFM cantilever upwards, increasing the cantilever deflection. Conversely, the domain contraction occurs if the initial domain polarization is anti-parallel to the applied electric field, decreasing the cantilever deflection (Figure 34). The cantilever deflection is directly related to the expansion or contraction of the sample electric domains and proportional to the applied electric field. A vector PFM with one vertical and two lateral channels can provide complete information for complicated samples with different directions of domains within the surface plane [132].

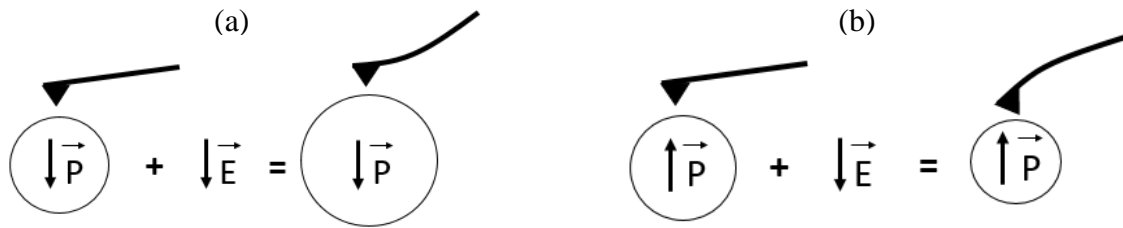


Figure 34. Expansion and contraction of the sample electric domains. Polarization (P) of the piezoelectric domain is (a) parallel and (b) anti-parallel to the applied electric field (E) (based on [132][133]).

3.3.10 Cytocompatibility tests

The Presto Blue™ viability and the osteogenic differentiation assay were performed in SS316L TT/SIL and SS316L TT/SIL/PLLA samples. A positive control group with cells and without biomaterial (CONTROL) was also studied.

First, the biomaterial samples were sterilized by ultraviolet light, for 20 min, at each side. The Human Dental Pulp stem/stromal cells (hDPSCs) obtained from AllCells, LLC (Cat. DP0037F, Lot N° DPSC090411-01) were cultured (see Appendix A) and maintained at 37 °C, 80 % humidified atmosphere and 5 % CO₂ environment, during the entire assays. Then, the assays were performed.

The Presto Blue™ viability assay evaluated the biomaterials cytocompatibility at four time-points: 24, 72, 120, and 168 h. However, osteogenic differentiation assay evaluated the calcium deposition (mineralization) in cell culture after 21 days. SEM micrographs after osteogenic differentiation assay verified the presence of cells on both samples. The tests were performed by the University of Porto (UP), in collaboration with the project “Advanced BioMEMs for Tissue Engineering: Applications in Hard Tissues (BioMEMs)”.

Presto Blue™ viability assay

The cytocompatibility between the cellular system and the biomaterials was assessed by Presto Blue™ assay based on an established protocol (see Appendix A) [134]. In this study, 10 samples from each group (SS316L TT/SIL, SS316L TT/SIL/PLLA, and CONTROL group) were used: 8 samples were placed in wells with cells (experimental wells) and 2 samples were placed in wells without cells (control wells).

First, the stem cells were seeded over the biomaterials and incubated. The culture medium was removed from each well at every time-point (24, 72, 120, and 168 h), the

Presto Blue™ cell viability reagent (Invitrogen, A13262) was added and the absorbance values were measured in triplicate at 570 and 595 nm, using a Multiskan™ FC Microplate Photometer (Thermo Scientific™, 51119000). Then, the corrected absorbance was calculated.

Resazurin, present in PrestoBlue™ Cell Viability Reagent, is a blue non-fluorescent compound. The viable cells reduce the resazurin to resorufin and the color of the media becomes red and fluorescent. Therefore, cell viability can be detected by measuring the absorbance of the final medium. The higher the corrected absorbance, the more viable cells reduced the resazurin, that is, the higher the cytocompatibility [134].

Osteogenic differentiation assay

The calcium deposition (mineralization), in cell culture after 21 days, was evaluated by osteogenic differentiation assay based on established protocols (see Appendix A) [135][136]. Sets of 16 samples from each group (SS316L TT/SIL, SS316L TT/SIL/PLLA, and CONTROL group) were studied: 8 samples with undifferentiated and 8 with differentiated cells.

First, the stem cells were seeded over the biomaterials and incubated. After 3 days, the cell wells reached 80 % confluency, and, at this point, cells were transitioned to Osteogenesis media (StemPro™ Osteogenesis Differentiation Kit, Gibco A1007201). Undifferentiated wells were maintained in culture media without osteogenic supplements. Media was changed every 3 days, and, after 21 days, the Alizarin Red S (ARS) assay was performed. Absorbance values were measured in triplicate at 405 nm, using a Multiskan™ FC Microplate Photometer (Thermo Scientific™, 51119000), and the ARS concentration in the samples was calculated. The ARS is a dye used to evaluate calcium deposits in cell culture and can be extracted from the stained monolayer of cells [136]. The higher the ARS concentration (mM), the higher the calcium deposition.

Scanning Electronic Microscopy (SEM)

The SS316L TT/SIL and SS316L TT/SIL/PLLA samples, without and with undifferentiated and differentiated cells, were collected and fixated for SEM (protocol in Appendix A) [137]. The samples were coated with gold/palladium for 80 s, using a current of 15mA. They were analyzed by a high resolution (Schottky) Environmental Scanning Electron Microscope (ESEN), working under the electron acceleration field of 15 kV.

CHAPTER IV
RESULTS AND DISCUSSION

CHAPTER IV - RESULTS AND DISCUSSION

4.1 Chemical composition by Fourier Transformed Infrared Spectroscopy (FTIR)

The chemical composition identification of molecules and substances on SS316L TT, SS316L TT/SIL, and SS316L TT/SIL/PLLA samples were studied using FTIR. Transmittance percentage was recorded as a function of wavenumber from 3150 to 350 cm^{-1} .

The FTIR spectra of SS316L TT and SS316L TT/SIL samples are presented in Figure 35. It was possible to identify the peak at 659 cm^{-1} for both samples (Figure 35.b). This peak is attributed to the presence of chromium oxide, Cr_2O_3 . The SS316L SIL also presented peaks at 1040 cm^{-1} and 1140 cm^{-1} due to the presence of siloxane groups (Si-O-Si) (Figure 35.c). There is a fluctuation in the baseline between 2400 and 2000 cm^{-1} that is related to atmospheric CO_2 (Figure 35.d) [138]. The identified peaks with the corresponding chemical composition are summarized in Table XIV. The presence of chromium oxide group, siloxane groups, and atmospheric CO_2 , were also found by Magueta, A. using FTIR in SS316 substrate after thermal treatment and silanization process [18].

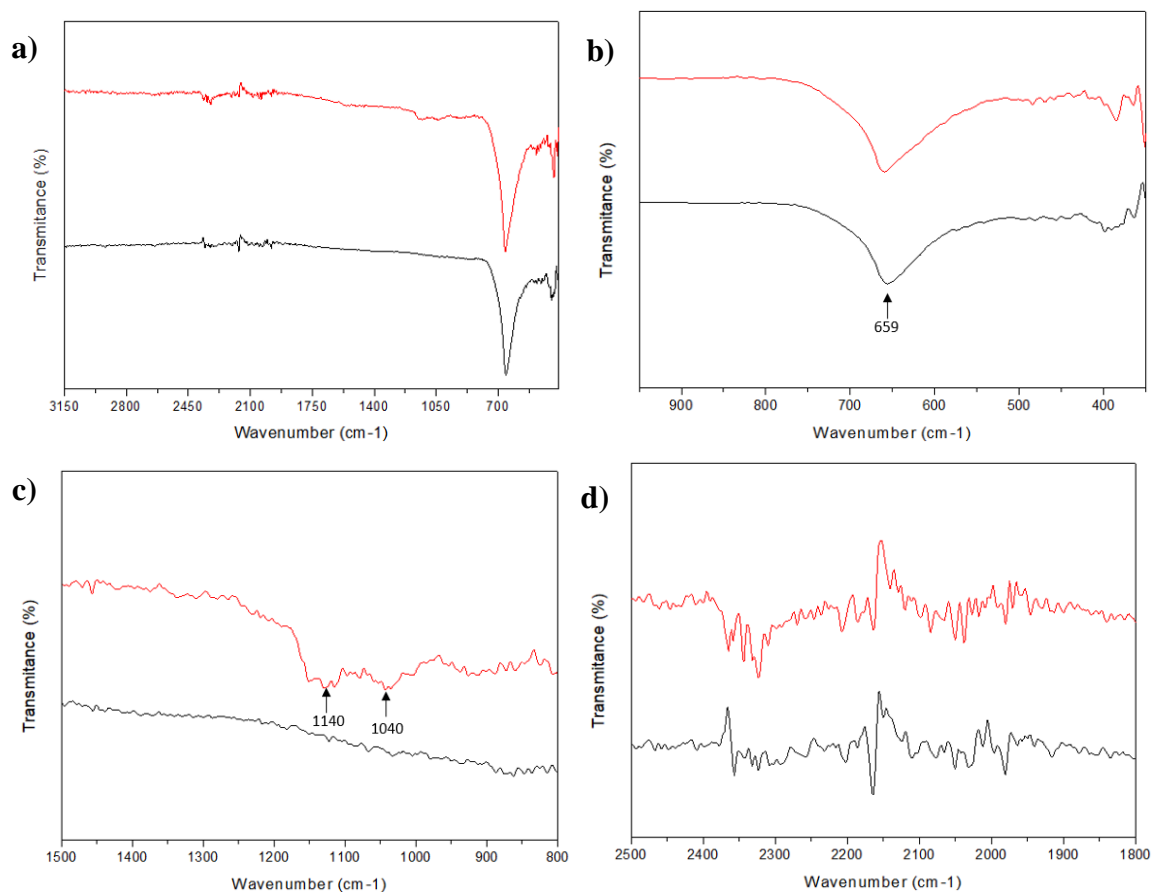


Figure 35. FTIR spectroscopy results of SS316L TT (black line) and SS316L TT/SIL (red line) samples. Transmittance percentage (%) as a function of wavenumber (cm^{-1}) a) from 3150 to 350 cm^{-1} , b) from 950 to 350 cm^{-1} , c) from 1500 to 800 cm^{-1} , and d) from 2500 to 1800 cm^{-1} .

Table XIV. FTIR peak assignment of SS316L TT and SS316L TT/SIL samples.

Wavenumber (cm^{-1})	Peak assignment
659	Cr_2O_3
1040, 1140	ν_{as} (Si-O-Si)
2400 – 1900	Atmospheric CO_2

ν_{as} = stretching symmetric vibration mode.

The FTIR spectra of SS316L TT/SIL/PLLA samples are presented in Figure 36. Many peaks of organic molecules were identified, like CH_3 , $\text{C}=\text{O}$, CH , $\text{C}-\text{O}-\text{C}$, $\text{C}-\text{CH}_3$, and $\text{C}-\text{C}$. The identified peaks and their corresponding chemical composition are summarized in Table XV.

The same peaks were found by Barroca, N., and Thangaraju, E. *et al.* in PLLA platforms and PLLA nanofibers, respectively [139][140]. The unequivocal identification of chromium oxide, siloxanes, and organic molecules by FTIR allows concluding that the thermal treatment, the silanization process, and the deposition of PLLA films have been carried out effectively.

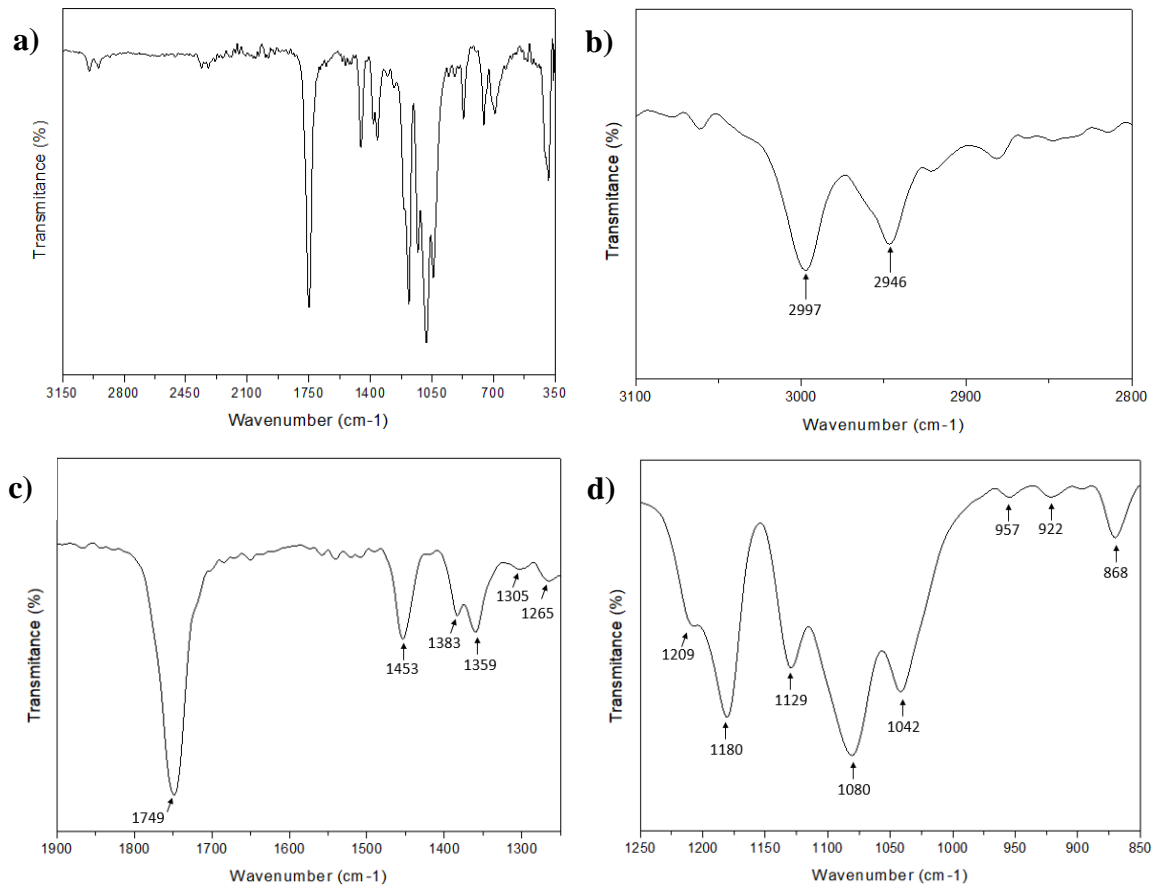


Figure 36. FTIR spectroscopy results of SS316L TT/SIL/PLLA samples. Transmittance percentage (%) as a function of wavenumber (cm^{-1}) a) from 3150 to 350 cm^{-1} , b) from 3100 to 2800 cm^{-1} , c) from 1900 to 1250 and d) from 1250 to 850 cm^{-1} .

Table XV. FTIR peak assignment of SS316L TT/SIL/PLLA samples [18][139].

Wavenumber (cm ⁻¹)	Peak assignment
2997	ν_{as} (CH ₃)
2946	ν_s (CH ₃)
1749	ν (C=O)
1454	δ_{as} (CH ₃)
1382	δ_s (CH ₃)
1359	δ_s (CH ₃) + δ (CH)
1304	ν (CH)
1265	ν (C-O-C) + ν (CH)
1212, 1180	ν_{as} (C-O-C) + ρ_{as} (CH ₃)
1129	ρ_s (CH ₃)
1080	ν_s (C-O-C)
1042	ν (C-CH ₃)
957, 922	ν (C-C)
868	ρ (CH ₃)

ν = stretching, δ = bending, ω = wagging, ρ = rocking, s = symmetric vibration mode and as = asymmetric vibration mode.

4.2 Structural analysis by X-Ray Diffraction (XRD)

The crystallographic planes and compounds of SS316L, SS316L TT, and SS316L TT/SIL/PLLA samples were identified using XRD. The obtained diffractograms are presented in Figure 37. The identified diffraction angles with their crystallographic planes, based on JCPDS-PDF cards [141][142], are summarized in Table XVI.

Table XVI. XRD results. Crystallographic planes and identified compounds for SS316L, SS316L TT and SS316L TT/SIL/PLLA samples. [141][142].

Diffraction angle (2Θ)	Crystallographic planes	Compound
16.6	(110)/(200)	PLLA α form
19.0	(203)/(113)	PLLA α form
43.5	(111)	Fe
50.6	(200)	Fe
74.5	(220)	Fe
90.4	(311)	Fe

The crystal structure of SS316L and SS316L TT samples presented peaks at 43.5, 50.6, 74.5, and 90.4 degrees, which corresponds to (111), (200), (220), and (311) crystallographic planes, respectively, due to the presence of Fe (Figure 37). It is possible to conclude that the thermal treatment did not change the crystal structure of the substrate. The *in-situ* XRD pattern of stainless steel 316 under different temperatures in air atmosphere was studied by Magueta, A. and was observed that, for temperatures lower than 800°C, only Fe is identified, while, for temperatures above 800°C, there is the formation of iron and chromium oxides (Fe_2O_3 , Fe_3O_4 , and $\text{Cr}_{0.25}\text{Fe}_{1.25}\text{O}_3$) [18].

For the SS316L TT/SIL/PLLA samples, peaks at 16.6 and 19.0 degrees were identified, due to the presence of PLLA α form, being (110)/(200) and (203)/(113) the corresponding crystallographic plans, respectively (Figure 37). The same crystallographic planes of α -form were found by Magueta A. for 2.5 wt % and 5 wt % PLLA films. Besides the peaks at 16.6 and 19.0 degrees, two other peaks at 14.6 and 22.3 degrees were identified in 5 wt % PLLA films, corresponding to (011) and (211) crystallographic plans, respectively [18]. The influence of temperature on the crystallization of PLLA was studied by Righetti, M. C. *et al.*, and these four peaks were also identified in PLLA samples which were heated at 200 °C for 2 min and 135 °C for 130 min and 145 °C for 240 min [143].

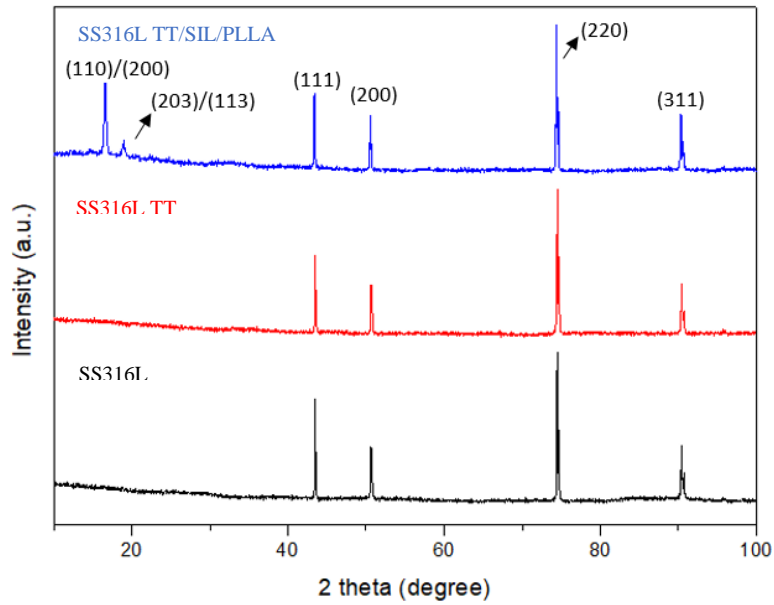


Figure 37. XRD patterns of SS316L (black line), SS316L TT (red line) SS316L TT/SIL/PLLA (blue line) samples. Diffraction peak intensity (a.u) as a function of the diffraction angle (2 theta degree).

4.3 Morphology and microstructure by Scanning Electron Microscopy (SEM)

The morphology and microstructure of the surface of SS316L TT/SIL/PLLA samples were studied by SEM at different magnifications (100, 500, and 1000 x). The micrographs are presented in Figure 38, clearly showing the formation of spherulites of well-defined borders. Spherulite size was obtained by measuring the mean diameters of 628 spherulites, using SEM micrographs and ImageJ software. The relative frequency in function of spherulite diameter is presented in Figure 39. The mean diameter of spherulite and the corresponding standard error was $88.86 \pm 1.72 \mu\text{m}$. Big spherulites with a diameter size distribution ranging from 19.4 to 270.4 μm were observed.

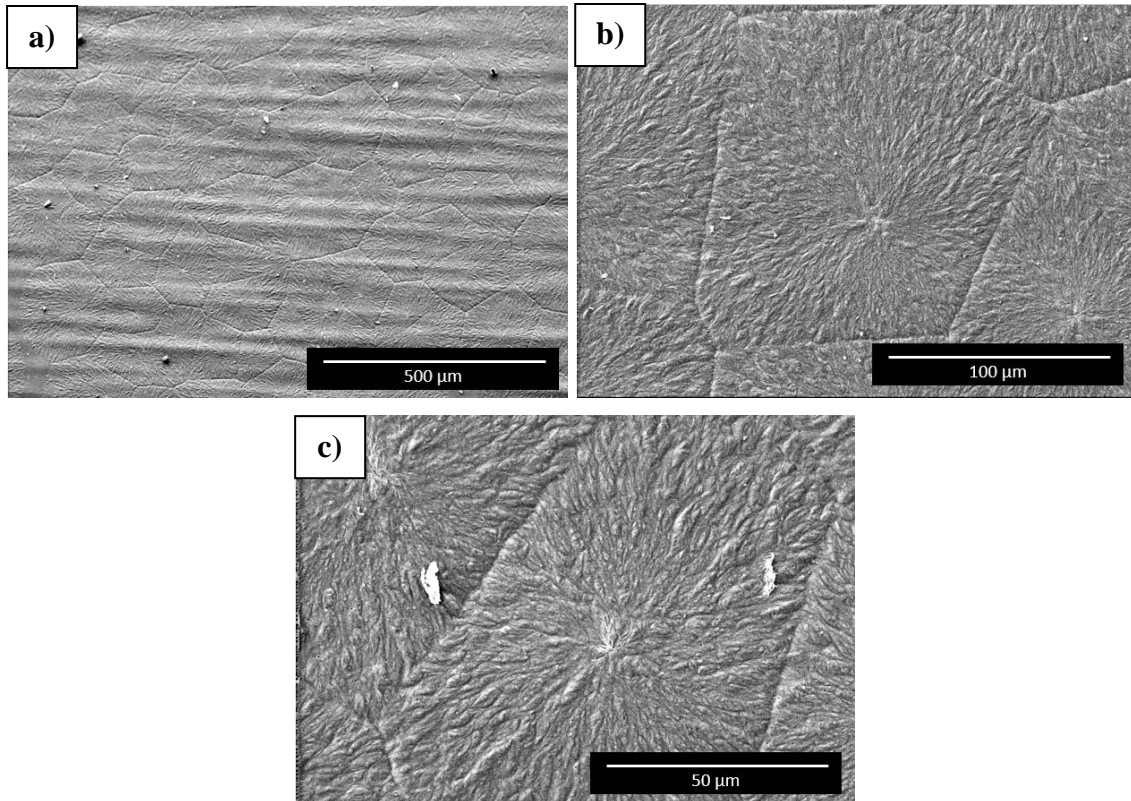


Figure 38. Micrographs of SS316L TT/SIL/PLLA samples with different magnifications: a) 100x, b) 500x and c) 1000x.

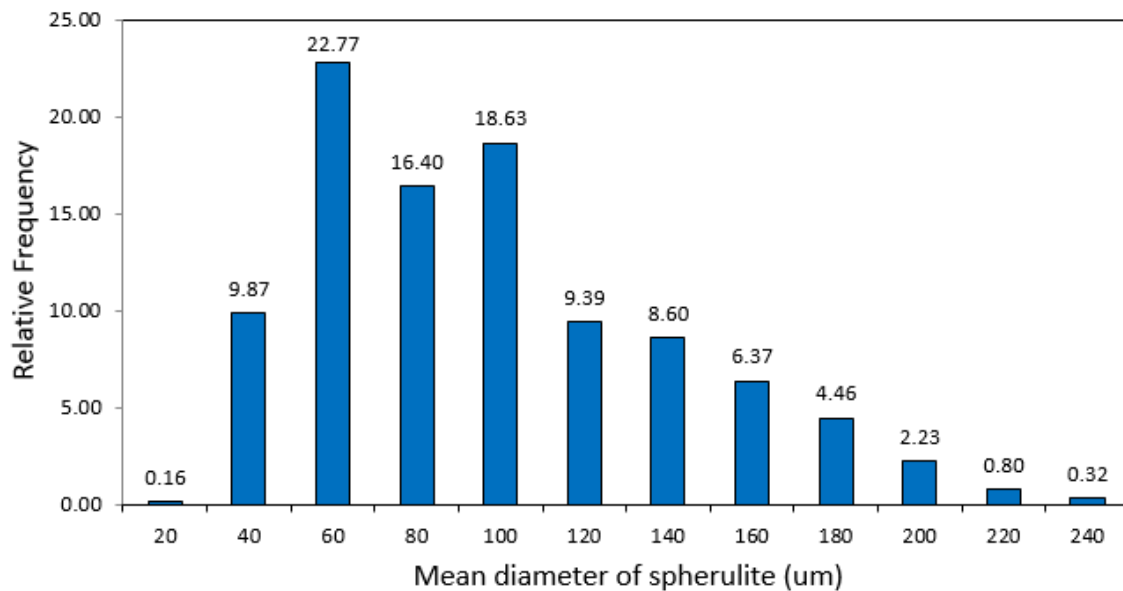


Figure 39. The relative frequency in function of spherulite diameter (μm) of 628 spherulites from the SS316L TT/SIL/PLLA samples.

The spherulite development in spin-coated films of poly (L-lactide) acid in dichloromethane solution was studied by Zoe, F. *et al.* [144]. The films were spin-coated

at 2000 rpm for 30 s at room temperature, dried at 37 °C, and then melted at 230 °C for 10 min, and crystallized at 100 °C (PLLA100) or 140 °C (PLLA140). Measuring the size of 100 spherulites, mean spherulite radius less than or equal to 150 μm and 800 μm was obtained for PLLA100 and PLLA140 films, respectively. The higher the crystallization temperature, the bigger the spherulites, because high crystallization temperature decreases the nucleation sites. It was also proved that higher crystallization temperatures generate more roughness. The ridge depth of the spherulites ranged 50 - 100 nm for PLLA100 film and 100 - 350 nm for PLLA140 film. Consequently, the roughness of the film increased from 35 nm to 88 nm.

The spin-coated PLLA films of 2.5 wt % poly (L-lactide) acid in 1,4 dioxane solution with different numbers of layers were produced by Magueta, A. [18]. The thickness of these films were $1.03 \pm 0.06 \mu\text{m}$, $1.17 \pm 0.19 \mu\text{m}$, and $1.98 \pm 0.21 \mu\text{m}$ for films with 1, 2, and 3 layers, respectively. It was observed that films with 3 layers had bigger spherulites, leading to the conclusion that the higher the thickness of the films, the bigger the spherulite size.

4.4 Surface roughness analysis

The surface roughness of SS316L, SS316L TT, SS316L TT/SIL, and SS316L TT/SIL/PLLA samples was studied to analyze the influence of the thermal treatment, silanization, and film deposition on the surface texture of the samples. The parameters studied were arithmetic mean roughness (R_A) and mean roughness depth (R_Z). The measurements were done in triplicate (see Appendix B) and the results are presented as mean \pm standard deviation in Figure 40.

Statistical analysis was performed using GraphPad Prism version 8.00 for Windows 10, GraphPad Software, LLC, and by One-Way ANOVA analysis with Tukey multi comparison test. Differences were considered statistically significant at $p \leq 0.05$. Results significance are presented through the symbol (*), according to the p-value, with one, two, three or four symbols, corresponding to $0.01 < p \leq 0.05$; $0.001 < p \leq 0.01$; $0.0001 < p \leq 0.001$ and $p \leq 0.0001$, respectively.

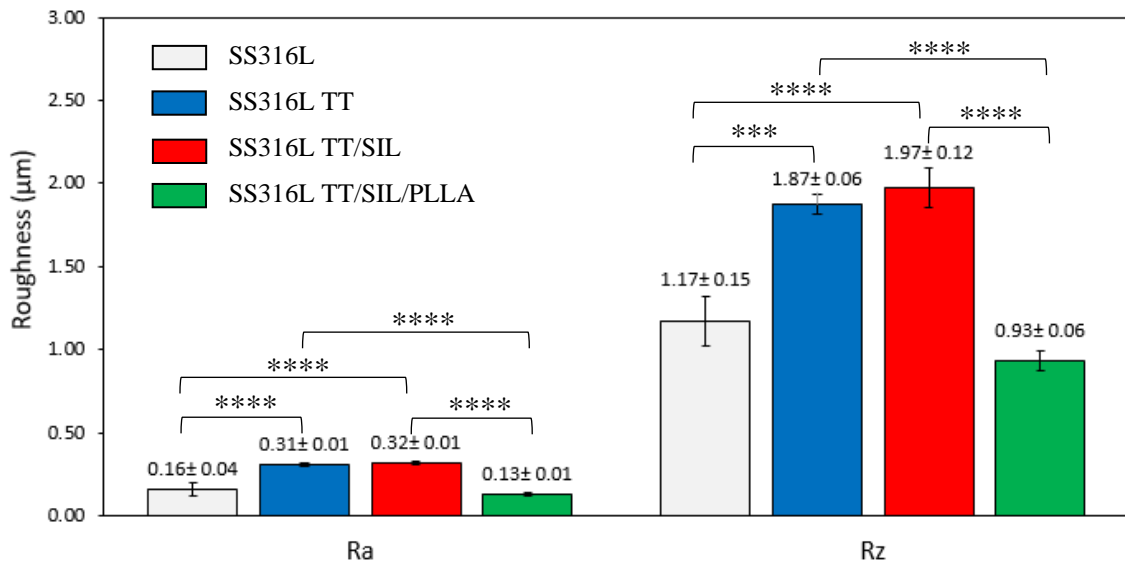


Figure 40. Arithmetic mean roughness (R_A) and mean roughness depth (R_Z) for each sample as mean \pm standard deviation. Differences were considered statistically significant at $p \leq 0.05$, and expressed by * ($0.01 < p \leq 0.05$), ** ($0.001 < p \leq 0.01$), *** ($0.0001 < p \leq 0.001$) and **** ($p \leq 0.0001$).

Comparing arithmetic mean roughness (R_A) and mean roughness depth (R_Z) results, as expected, the R_Z values are higher than R_A values because R_Z considers the mean value of the sum of the maximum peak height and the maximum valley depth, while R_A considers the arithmetical mean of the absolute values of the profile deviations from the mean line. Using the R_Z results, it is possible to conclude that there are significant roughness differences caused by micro holes, scratches, contamination, or measurement noise at some points of the surface.

Based on the statistical analysis, the thermal treatment increased the R_A and R_Z of the SS316L substrates by 93.75 % and 59.83 %, respectively, suggesting that the temperature used in the thermal treatment permitted the intergranular corrosion. The presence of at least 10 % chromium makes the steel to be stainless, but if the sample is exposed to high temperatures (450 – 800 °C), chromium carbides are formed and precipitate at grain boundaries, decreasing the presence of chromium in this region, turning the steel very sensitive to the corrosion process. This corrosion increases the size of the valleys and, consequently, increases the roughness of the SS316L substrate [145].

The silanization process did not significantly change the roughness. However, the PLLA film decreased the R_A and R_Z of SS316L SIL samples in 59.38 % and 52.79 %, respectively. Probably, the PLLA solution fills the valleys, decreasing the roughness.

Worthwhile to say that the roughness of PLLA films depends considerably on the processing, presence or not of a substrate, type of substrate, degree of PLLA crystallinity, among other factors. For example, free-standing PLLA films of the average thickness of 350 μm and 2 % of crystallinity were reported to have roughnesses of 0.02 μm and 0.10 μm , R_A , and R_Z , respectively [146]. The low roughnesses of these last PLLA films are probably due to the low crystallinity of the films and the non-presence of a substrate. The higher the crystallinity of the films and the roughness of the substrate, the higher the roughness of the films [144].

PLLA films with big spherulites present high surface roughness and, consequently, high adhesion, proliferation, and differentiation of MC3T3-E1 osteoblastic cells as observed by Zoe, F. *et al.* [144]. In addition, the rough films presented strong cell alignment along the radial direction, whereas, non-rough films presented randomly cell distribution on the surface. However, the role of the surface roughness on the proliferation of 3T3 fibroblast and MC3T3-E1 osteoblast cells on PLLA films was studied by Ribeiro, C. *et al.* [147]. It was verified that high roughness promotes low osteoblast but high fibroblast proliferation.

The PLLA film thickness was calculated based on the maximum roughness depth (R_{MAX}), which is the largest single roughness depth within the transverse length. The measurements were done in triplicate (see Appendix B) and the mean \pm standard deviation was $4.78 \pm 1.21 \mu\text{m}$. The extruded magnesium rod (99.95 % composition, 8 mm diameter and 2 mm thickness) coated with PLLA film of 5 % (w/v) poly (L-lactic) acid in chloroform solution were studied Xu, L. and Yamamoto, A. The polymer film was prepared by spin coating at 5000 rpm for 30 s and 3 layers were deposited. PLLA pellets of low and high molecular weight were used and the thicknesses of the films were 0.34 and 0.97 μm , respectively [148]. The thicknesses of the PLLA films made by Xu, L. and Yamamoto, A. are lower than the thickness of the PLLA films of this work, probably, due to higher spinning speed and lower solution concentration used by them. The higher the spinning speed and the lower the solution concentration, the lower the film thickness [119].

4.5 Adhesion measurements by Tape test

The adhesion of the PLLA film to the SS316L substrate was evaluated, in triplicate, using pressure-sensitive tape, and then classified according to the ASTM D3359 standard [125]. The surface of the cross-cut area was observed in an optical

microscope and the test results were 5B, that is, the percentage of the area removed was 0 %. After the test, the samples were also observed in SEM (Figure 41). The clear identification of the PLLA spherulites allows concluding that the PLLA films remained on the SS316L substrate, without any morphology changes. The crystallized PLLA films were studied by Magueta, A. and the 5B result was also obtained [18]. Therefore, it was proved that the silanization process is efficient in promoting the adhesion of the polymer to the substrate.

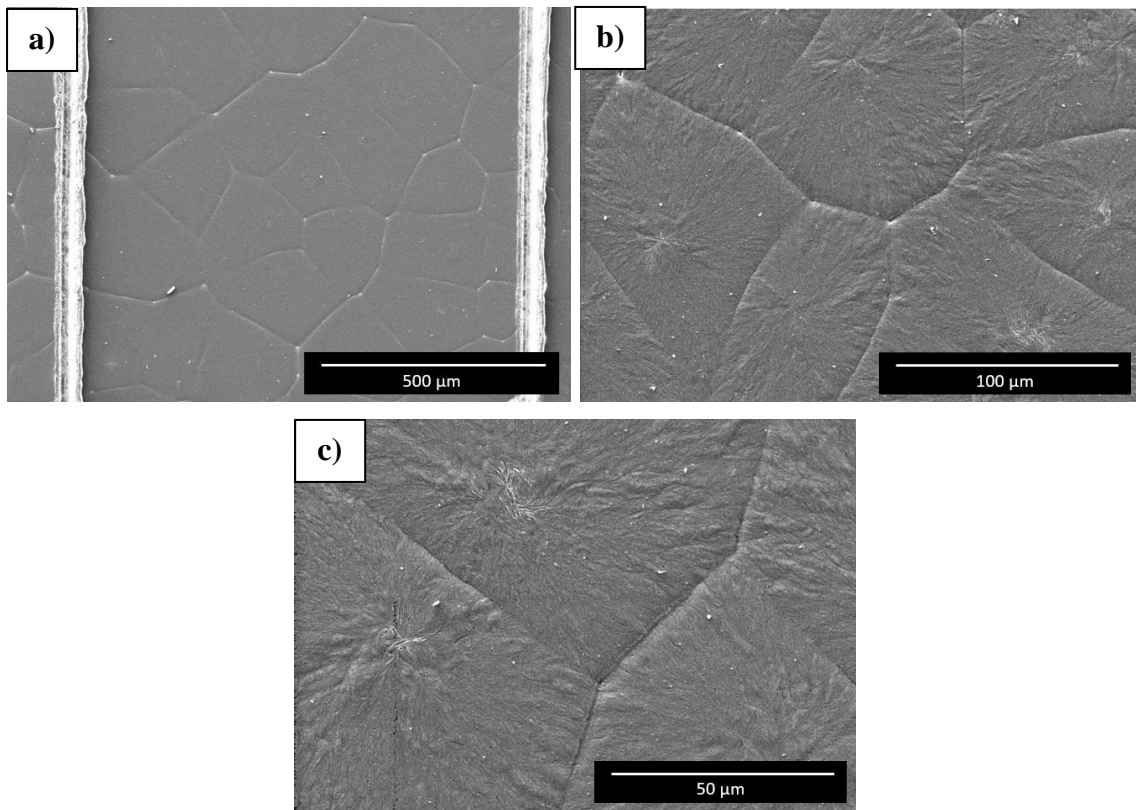


Figure 41. Micrographs of SS316L TT/SIL/PLLA samples after tape test with different magnifications: a) 100x, b) 500x and c) 1000x.

4.6 Wettability and surface energy by contact angle measurements

The wettability and the surface energy of the SS316L TT/SIL/PLLA samples were studied by measuring the contact angle of the PLLA films with ten drops of water and diiodomethane. The contact angle with water was $83.48 \pm 1.94^\circ$ and with diiodomethane was $40.03 \pm 6.43^\circ$ (see Appendix C).

PLLA film surface is considered little hydrophilic/wettable due to the high contact angle with water. The contact angle around $74.7 \pm 4.6^\circ$ for spin-coated PLLA films of 5 wt % poly (L-lactic) acid in 1,4-dioxane solution was measured by Barroca, N [140].

The films, with 6 μm of thickness, were melted for 30 min at 190° and then crystallized for 30 min at 80° . On the other hand, the contact angle of $80.2 \pm 2.5^\circ$ for PLLA films of 2 wt % poly (L-lactic) acid in chloroform solution was measured by Wang, Y-Q [149]. The films, with 0.1 mm of thickness, were dried under the vacuum.

The surface energy of SS316L TT/SIL/PLLA samples (γ_S) was determined using a linear equation of the type $y=m.x+c$ (Equation 23) for each liquid (water and diiodomethane), where the abscissa x is $\sqrt{\frac{\gamma_L^p}{\gamma_L^d}}$ and the ordinate y is $\frac{\gamma_L (1+\cos \theta)}{2\sqrt{\gamma_L^d}}$.

$$\frac{\gamma_L (1 + \cos \theta)}{2\sqrt{\gamma_L^d}} = \sqrt{\gamma_S^p} \cdot \sqrt{\frac{\gamma_L^p}{\gamma_L^d}} + \sqrt{\gamma_S^d} \quad \text{Equation 23}$$

Using the contact angle values, and γ_L , γ_L^d and γ_L^p values (Table XVII), x and y for water and diiodomethane equation were calculated (Table XVIII).

Table XVII. Dispersive and polar parts of surface tension of water and diiodomethane [150].

Liquid	γ_L^d (mJ/m ²)	γ_L^p (mJ/m ²)	γ_L (mJ/m ²)
Water	22.0	50.2	72.2
Diiodomethane	48.5	2.3	50.8

Table XVIII. Calculated values of x and y for water and diiodomethane equation.

Liquid	x	y
Water	1.51	8.57
Diiodomethane	0.22	6.44

The points (x,y) were expressed in a graphic and a regression line ($y = 1.65x + 6.08$) was created. The $m = 1.65$ and $c = 6.08$ were obtained from the line equation. Considering that $m = \sqrt{\gamma_S^p}$, $c = \sqrt{\gamma_S^d}$ and $\gamma_S = \gamma_S^d + \gamma_S^p$, it is possible to obtain $\gamma_S^p = 2.72$, $\gamma_S^d = 36.98$, $\gamma_S = 39.70$. That is, the surface energy of PLLA films coating on the SS316L substrate is 39.70 mJ/m². A similar surface free energy of 46.01 mJ/m² is reported in the literature for PLA film without additives and 30 μm thickness, using Fowke's method [151].

The wettability and surface free energy are fundamental properties of the material surface because they will govern the first interactions with the biological environment. In general terms, currently, research has often reported that high wettability and surface free energy promote cell adhesion. Polymers have low wettability and surface energy due to weak intermolecular forces, thus, for many biomaterial applications in which cell adhesion is required, polymer surface modification is often necessary, like plasma and NaOH treatment [149][152].

4.7 Thermal properties by Differential scanning calorimetry (DSC)

The thermal properties of the PLLA films were studied by DSC. The phase transitions were defined by observing the heat flow (J/s.g) as a function of the temperature (°C) (Figure 42). During heating, the glass transition (T_g) and the melting temperature (T_m) were 60.4 °C and 179.4 °C, respectively. During cooling, the crystallization temperature (T_c) was 73.0 °C.

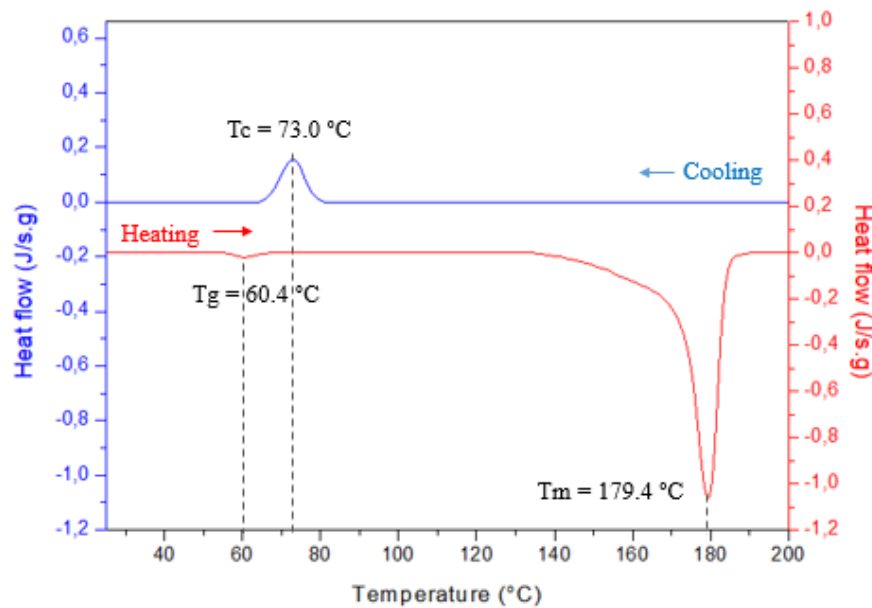


Figure 42. Heat flow (J/s.g) as a function of the temperature (°C) by DSC of the PLLA film.

The degree of crystallization was defined by Equation 14. Using the Origin Pro 8 software, the peak area of the melting temperature (T_m) was calculated in the graph of heat flow (J/s.g) as a function of time (s) (Figure 43) [32]. The specific enthalpy of fusion (J/g) of the PLLA film (ΔH_f) was -69.80 J/g.

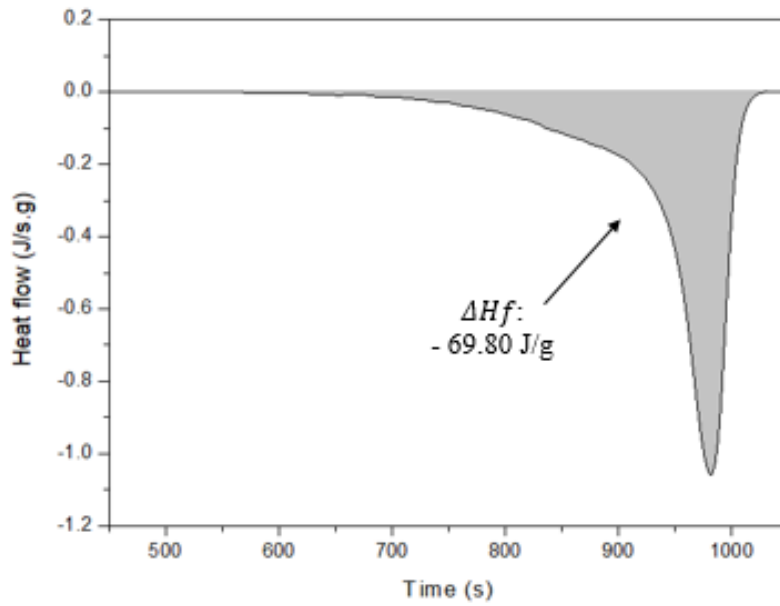


Figure 43. The specific enthalpy of fusion (J/g) of the PLLA film (ΔH_f).

Considering for the enthalpy of fusion of 100 % crystalline PLLA samples with α -crystals (ΔH_f^0) the value of -143.00 J/g [153], then, the degree of crystallization is 48.81 % (Equation 24).

$$X_c (\%) = \frac{\Delta H_f}{\Delta H_f^0} \times 100 = \frac{-69.80 \frac{J}{g}}{-143.00 \frac{J}{g}} \times 100 = 48.81 \% \quad \text{Equation 24}$$

The melting temperature (T_m) at 180 °C and the crystallization temperature (T_c) at 145 °C for 100 % crystalline PLLA samples with α -crystals were identified by Righetti, M. C. *et al.* [153]. The samples were heated from room temperature to 200° C and maintained at this temperature for 3 min. Subsequently, the samples were cooled to 145 °C and crystallized for 250 min. PLLA films were melted at 200 °C for 3 min and crystallized at 120 °C for 55 min by Priscila, M. [154]. The glass transition (T_g) at 65 °C, melting temperature (T_m) at 175 °C, and crystallization temperature (T_c) at 95 °C were identified, approximately. The degree of crystallization of the films was 34.86 %. However, the degree of crystallization of 53 % for PLLA samples, crystallized at 140 °C for 100 min, was calculated by Shyr, T-W. *et al.* [155], based on the peak integration of wide-angle X-ray scattering (WAXS).

The proliferation of 3T3 fibroblast and MC3T3-E1 osteoblast cells in PLLA films of 10 wt % poly (L-lactic) acid in methylene chloride (DCM) and N,N-dimethylformamide (DMF) solution were studied by Ribeiro, C. *et al.* [147]. The films, with 40 μm thickness, approximately, were subjected to thermal annealing at different temperatures (70, 90, and 140 $^{\circ}\text{C}$) and times (10, 60, and 1440 min), obtaining different degrees of crystallization (20, 30, and 50 %). It was observed that the films with higher crystallinity presented low proliferation of osteoblast and high proliferation of fibroblast cells.

The role of polymer crystallinity on adhesion and proliferation of HEPM 1486 osteoblast and NIH 3T3 fibroblast cells in poly (caprolactone-co-glycolide) (PCL/PGA) films with different compositions (0:100, 25:75, 35:65, 45:45, and 100:0) were evaluated by Helen, C. and Patrick, J. S. [156]. PCL and PGA polymers were selected because they have high crystallinity and low crystallinity, respectively. Polymeric films were prepared using a melt-compression method, in which the polymers were processed at temperatures above their melting points, and films of 3 mm in diameter and 300 μm in thickness, approximately, were produced. The samples were dehydrated in an isopropyl alcohol solution (70 %) and dried in vacuum for 48 h. It was observed that the crystalline and rigid surfaces enabled remarkable growth of fibroblast cells, whereas the amorphous and flexible surfaces enabled greater growth of osteoblast cells. Therefore, the crystallinity and rigidity of polymer films play an important role in cellular responses.

4.8 Electric properties by Impedance spectroscopy

Electric properties of PLLA films on SS316L substrates were studied using impedance spectroscopy. Dielectric relative permittivity (ϵ_r), dielectric loss tangent ($\tan(\delta)$) and resistivity (ρ) were determined as a function of frequency (from 1 kHz to 100 kHz) and temperature (from 120 $^{\circ}\text{C}$ to 24 $^{\circ}\text{C}$).

The relative permittivity and dielectric losses are presented in Figure 44 and Figure 45. PLLA films on 316SS L present low permittivity and dielectric losses. ϵ_r varies between 5.0 and 6.2 (Figure 44), and $\tan(\delta)$ varies between $0.5 - 3.5 \times 10^{-2}$ (Figure 45).

As the frequency increases and for low temperatures, below 60 $^{\circ}\text{C}$, the permittivity keeps almost constant in this frequency range (Figure 44.a). As the temperature increases the permittivity increases and slightly decreases with frequency, except at 80 $^{\circ}\text{C}$ in which the decreasing of ϵ_r is from 5.9 at 1 kHz to 5.3 at 100 kHz (Figure 44.a). The effect of the

temperature for the different frequencies is clearly seen in Figure 44.b, in which a well-defined increase of the permittivity is observed for the temperature interval between 60 to 90 °C and the curves are shifted to higher temperatures as the frequency increases.

The dependence of the polarization on the temperature is well seen in the loss curves as well, with typical bell shape curves peaking between 60 and 90 °C depending on the frequency; i.e. these peaks move to higher temperatures when frequency increases (Figure 45.b). The peak for 1 kHz appears at 73.1 °C and the peak for 100 kHz appears at 86.3 °C. It is also possible to observe that the higher the frequency, the higher the dielectric loss tangent, The peak of $\tan(\delta)$ enhanced from 3.0×10^{-2} for 1 kHz to 4.0×10^{-2} for 100 kHz, approximately.

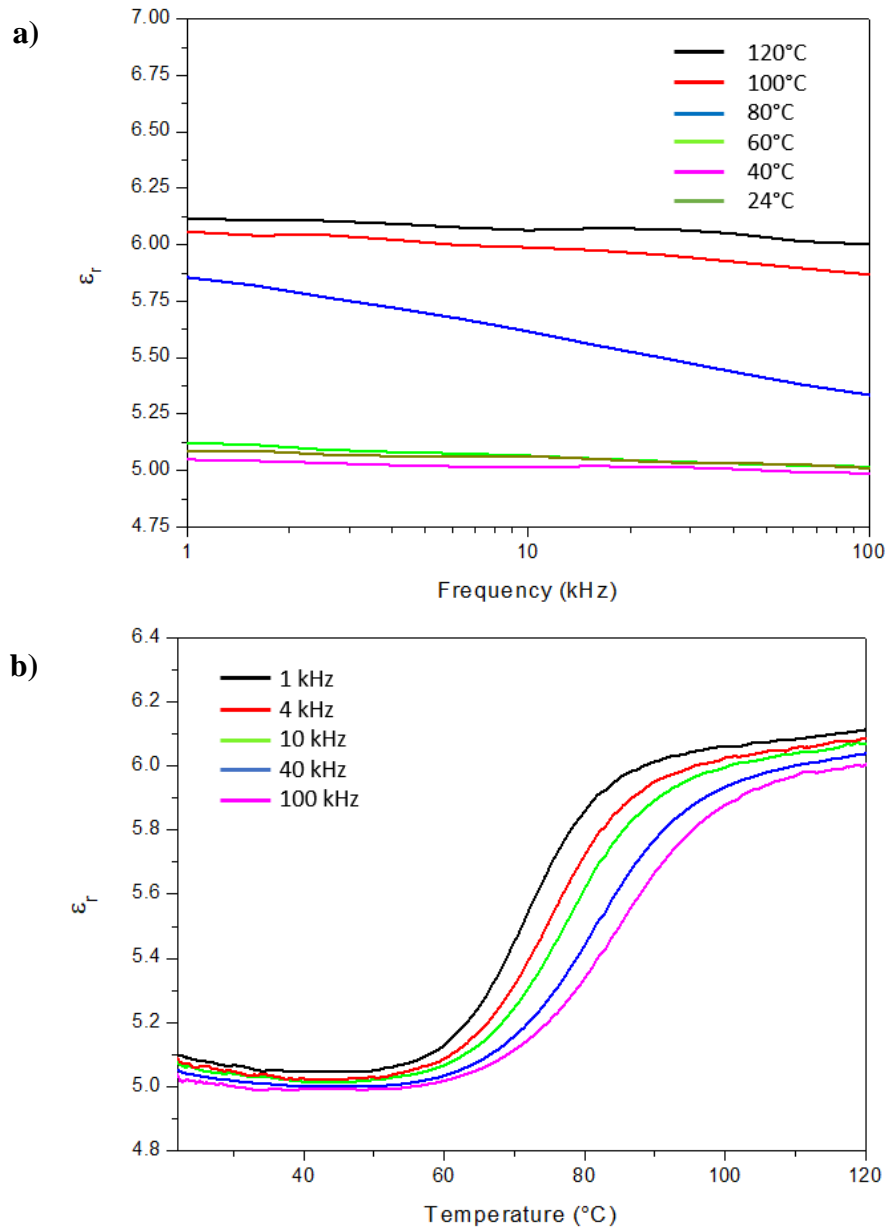


Figure 44. Relative permittivity (ϵ_r) as a function of a) frequency and b) temperature.

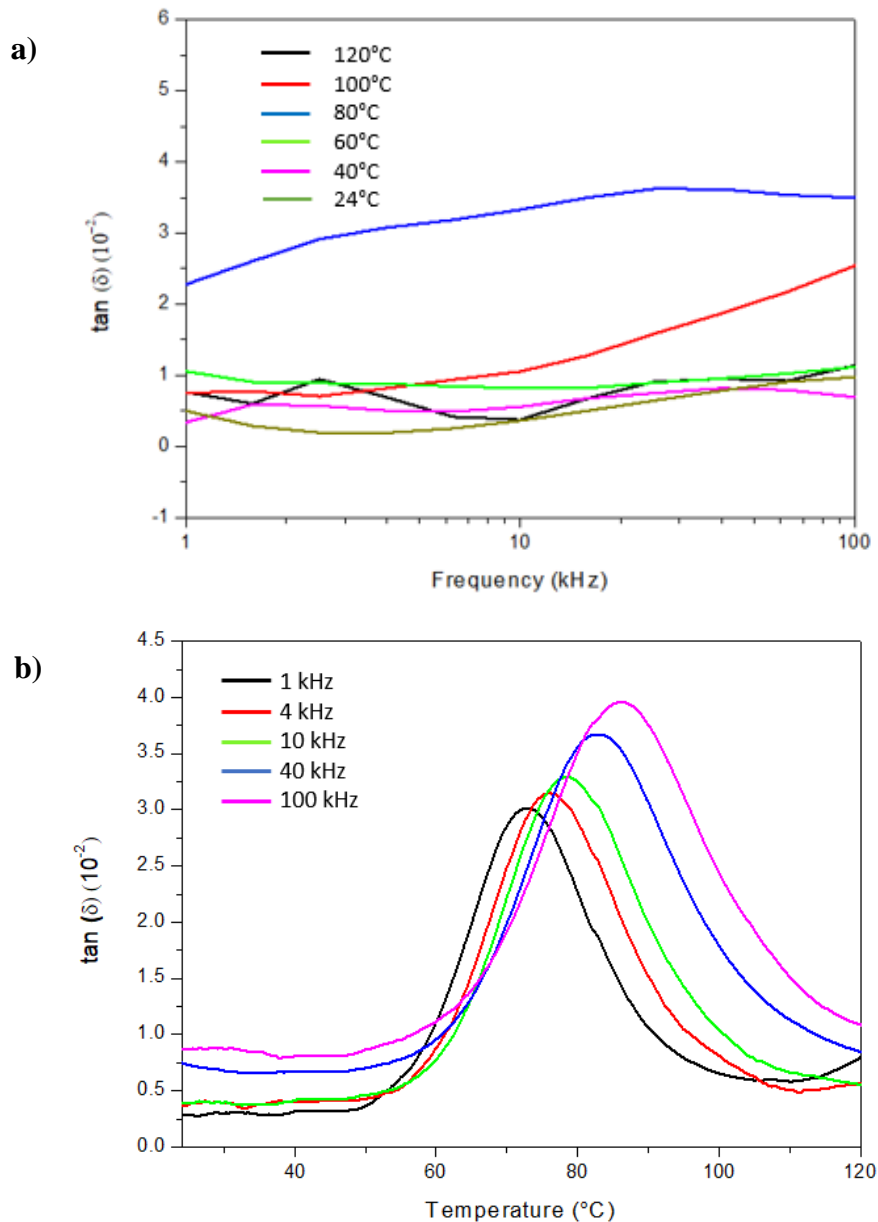


Figure 45. Dielectric loss tangent ($\tan(\delta)$) as a function of a) frequency and b) temperature.

The results of the relative permittivity (ϵ_r) and dielectric loss tangent ($\tan(\delta)$) are in accordance with the literature. The increase in temperature breaks the intermolecular forces and allows the motion of the polymers chains, thus, the polar groups orient themselves easily and follow changes in the electric field (E), facilitating/increasing the polarization (P). At glass transition (T_g), at 60.4 °C, according to the DSC results presented in topic 4.7, the α segmental relaxation in PLLA films occurs due to the melting of the amorphous regions. This relaxation is presented as an increase in ϵ_r (Figure 44.b) and a peak in $\tan(\delta)$ between 60 °C and 100 °C (Figure 45.b) [157].

At frequencies below relaxation frequency (f_r), the molecular dipoles respond easily and align with the applied alternating electric field (E) without time lag. Then, the polarization reaches its maximum value and the dielectric loss is small. At f_r , the dipoles can only partially follow the oscillation of the electric field, so, their contribution to ϵ_r is small. This time lag or phase difference between E and P increases the dielectric loss that reaches the peak at f_r (Figure 45.b). The rise in frequency also causes the delay in the peak of $\tan(\delta)$ because the fewer molecules follow the field, the greater the energy (temperature) required to cause relaxation (Figure 45.b). However, at frequencies above f_r , the dipoles cannot follow the E and do not contribute to ϵ_r . Only atoms and electrons can follow the E at high frequencies [130].

The AC resistivity (ρ) results as a function of frequency and temperature are represented in Figure 46. Resistivity decreases with frequency and temperature. The decrease in resistivity while the frequency increases (Figure 46.a,b) may be due to the presence of polarons, that move along the polymer chain in the amorphous region, allowing the flow of charges [41][158]. Figure 46.b shows that the resistivity decreases from 1.3×10^9 to 0.4×10^9 in the 1 kHz curve because thermal energy helps molecules to overcome the potential barrier in the conduction mechanism. The conduction increases mainly when the temperature exceeds T_g , causing a minimum of resistivity, as observed between 50°C and 100°C in the 1kHz curve (Figure 46.b) [159][158].

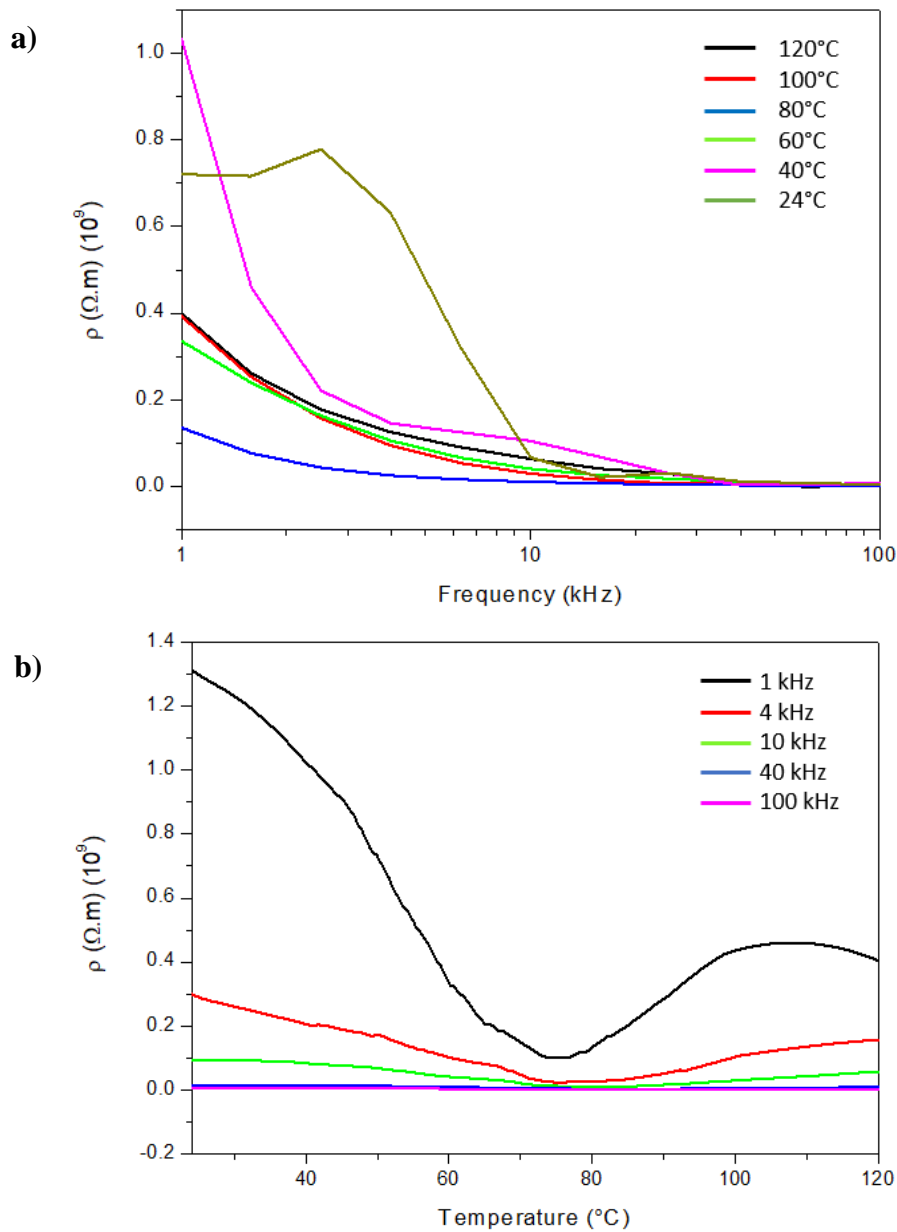


Figure 46. AC Resistivity (ρ) as a function of a) frequency and b) temperature.

The dielectric properties of 3D printed PLA varying the frequency from 1 Hz to 3 GHz, and the temperature from $-123^{\circ}C$ to $147^{\circ}C$, at a rate of 0.2 K/min, were studied by Dichtl, C. *et al.* [159]. It was observed that the higher the temperature and the lower the frequency, the greater the dielectric constant (ϵ'). At frequencies between 1 Hz and 117 kHz, the ϵ' values enhanced from 3.0 at $24^{\circ}C$ to 4.0 at $120^{\circ}C$, approximately, and increased quickly from $50^{\circ}C$ (close to the glass transition (T_g) at $60.4^{\circ}C$). A peak in dielectric loss (ϵ'') and the conductivity (σ), between $50^{\circ}C$ and $100^{\circ}C$, was identified

and associated with relaxation at T_g . They also observed that the higher the temperature and the higher the frequency, the greater the conductivity (σ).

The effects of crystallinity on dielectric properties of poly (L-lactide) were evaluated by Hikosaka, S. *et al.* [160]. It was observed that, below the glass transition (T_g), the crystallinity does not affect the conductivity. At temperatures above T_g , the conductivity becomes greater as the crystallinity decreases. This occurred because the lower the crystallinity of the material, the more polymer chains acquired movement and allowed the flow of charges. They also observed that the values of the dielectric constant (ϵ') and the dielectric loss (ϵ'') peak become smaller as the crystallinity becomes higher. This was attributed to the amorphous regions decrease, in which polarization and segmental relaxations occur.

4.9 Topography, electrophysical and piezoelectric properties by Atomic force microscopy (AFM)

The topography, electrophysical (surface potential, electric field, and capacitance distributions), and piezoelectric properties were studied in fibril and spherulite structures of PLLA films using AFM technique in different modes: Electrostatic Force Microscopy (EFM), Kelvin Probe Force Microscopy (KPFM) and Piezoresponse Force Microscopy (PFM).

Atomic force microscopy (AFM)

Figure 47.a shows a general topography of the PLLA film acquired at $70 \times 70 \mu\text{m}^2$ where the SS316L substrate (black part), the edge of the film, and the PLLA film (brown part) can be distinguished. The cross-section profile (yellow line in Figure 47.a) applied to these parts is presented in Figure 47.b and the thickness of the PLLA film was measured at about $4.4 \mu\text{m}$.

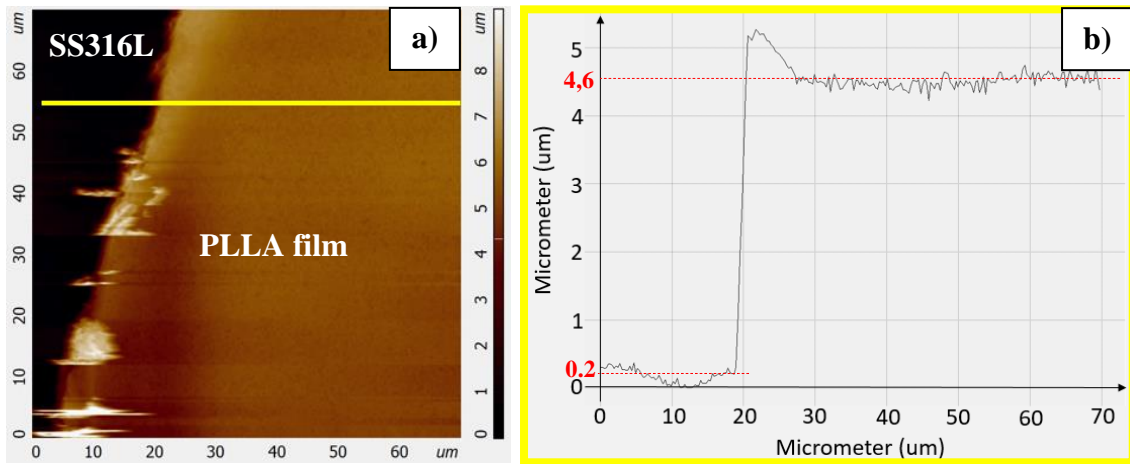


Figure 47. (a) AFM topography scan image of PLLA film and (b) corresponding cross-section profile.

An inhomogeneous behavior of the PLLA film was verified by using phase-sensitive semicontact AFM mode. There are three different areas were analyzed: 1) in the vicinity of the substrate (Figure 48.a-b), 2) several μm from the substrate (Figure 48.c-d), and 3) at a significant distance from the substrate (Figure 48.e-f). The topography and phase scan images of the PLLA film near the substrate are different reflecting the strong influence of the boundary. This also means that chemical and physical properties can be significantly different at this place. The far from the substrate, the more homogenous phase image of the surface of the PLLA film is observed (Figure 48.d). It is important to mention that the topography image reveals a uniform fibril structure (Figure 48.c). The increasing resolution allows observing these fibrils in details possessing equal phase contrast (Figure 48.e-f).

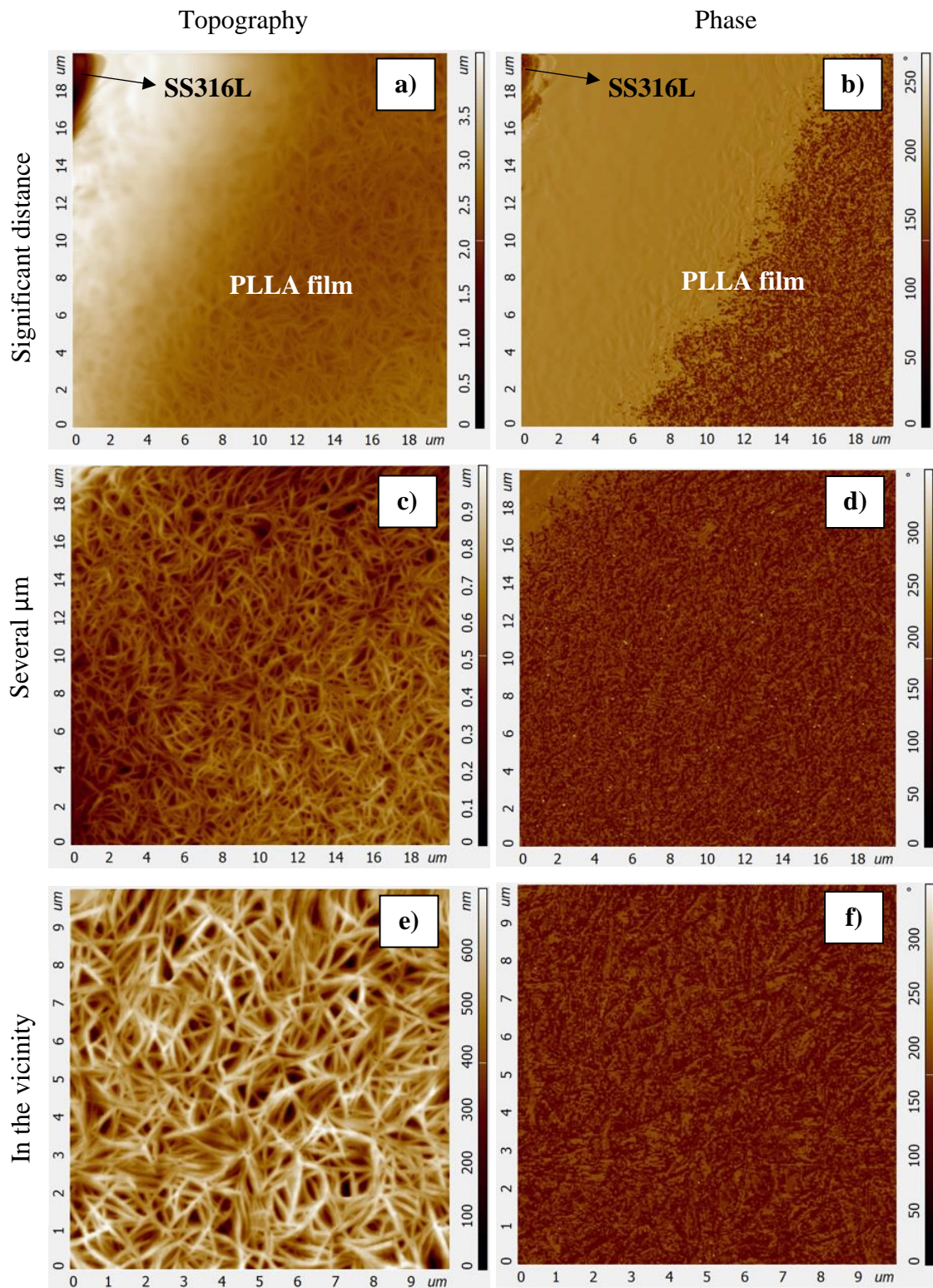


Figure 48. AFM topography and phase scan images acquired on different areas of the PLLA film: (a-b) in the vicinity of the substrate, (c-d) several μm from the substrate, and (e-f) at a significant distance from the substrate.

The verification of the spherulite and spherulite's grain boundary structures are presented in Figure 49. These spherulites demonstrate a sufficiently big diameter (60 μm), high roughness (2 μm), and broad grain boundary width (2-5 μm) on the large scan image Figure 49.a-d. While the decreasing of the scan image area, the fibril structure can be recognized inside the spherulites [161] with a roughness of about 200 nm (Figure 49.e,f).

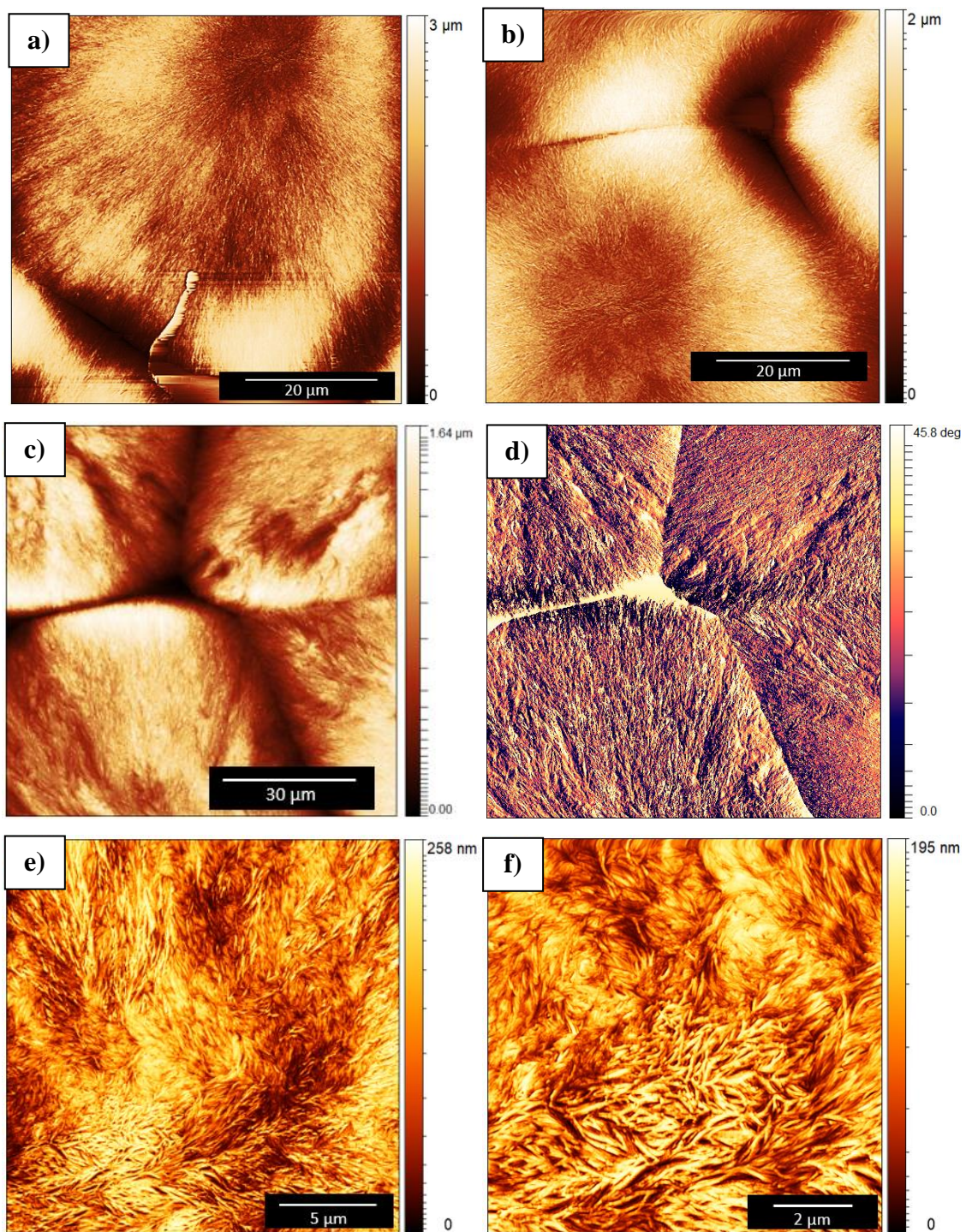


Figure 49. AFM scan images of spherulite structure: a-b) morphology, c-d) grain boundary and e-f) fibril structure.

Electrostatic Force Microscopy (EFM) / Kelvin Probe Force Microscopy (KPFM)

Electrophysical properties of PLLA film were studied using EFM and KPFM approaches. Figure 50 shows the results of the EFM scan done with and without the application of *dc* bias voltage (BV). The EFM scan without *dc* BV demonstrates the only phase separation associated with morphological properties of the PLLA film-related fibril structure (Figure 50.b). The corresponding topography displays a uniform structure with an intermediate single fibril's dimension at about 1.0 μm in length and 200 nm in diameter (Figure 50.a). An application of ± 5 *dc* BV results in considerable EFM scan image alteration (Figure 50.c-d). Generally, the positive voltage yields in higher EFM signal contrast in comparison to the negative voltage. However, considering the fibril structure, there is a coexistence of EFM signal contrast alteration in dependence on voltage polarity. Since the EFM phase signal is proportional to the electrostatic charge density (the attractive forces reduce the resonant frequency of the cantilever and the repulsive forces increase the frequency [162]) the potential differences observed in fibril structure corresponding to the meaningful influence of electrostatic forces. These electrostatic charges can be rearranged in different ways according to the applied voltage. The origin of these electrostatic charges is due to uncompensated carbonyl groups organized into the fibril structure of the PLLA film [37].

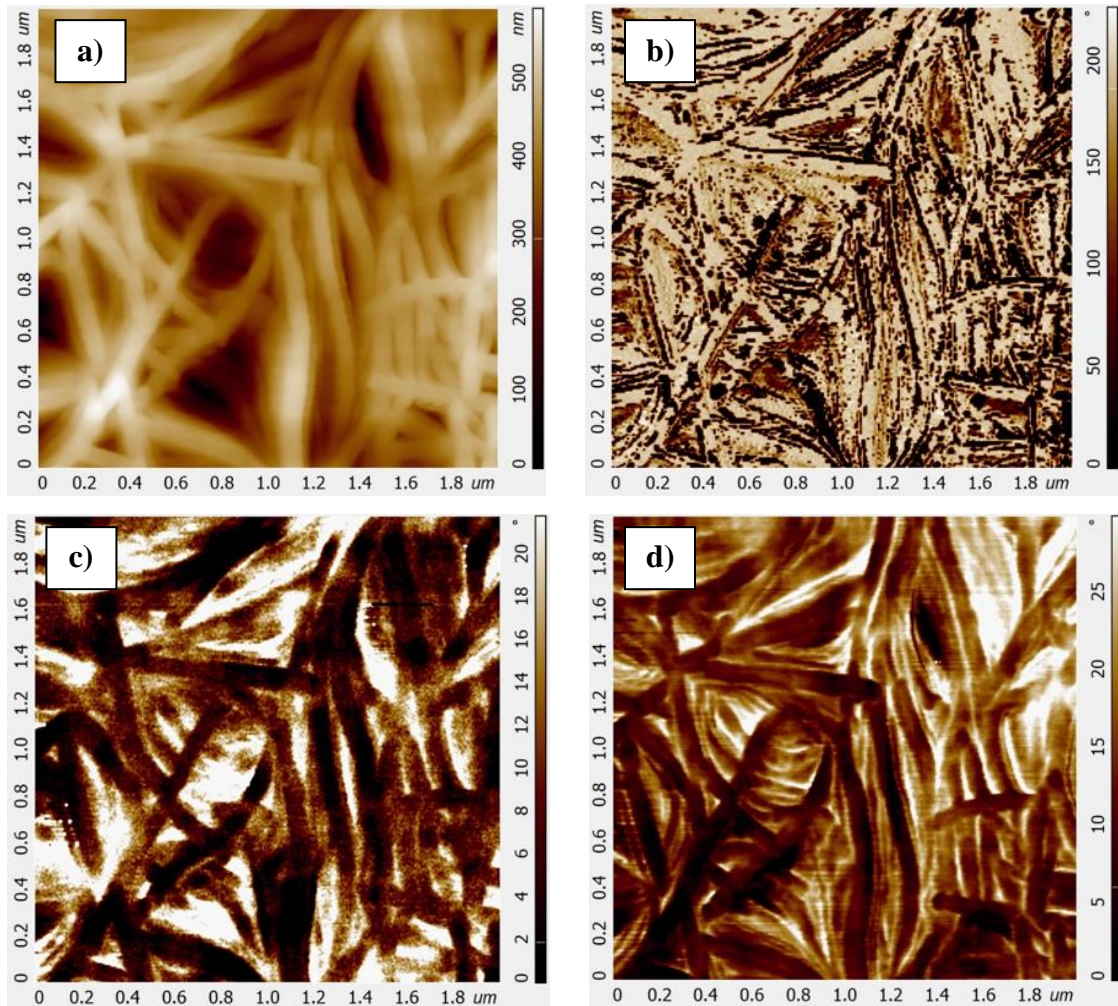


Figure 50. Electrostatic Force Microscopy scan images of PLLA film: (a) topography, (b) 0, (c) + 5V, and (d) - 5V *dc* BV.

The PLLA surface potential distribution was measured by the KPFM method (Figure 51). At the large scan images ($20 \times 20 \mu\text{m}^2$) the spherulites and the spherulite's grain boundary of the PLLA film can be distinguished (Figure 51.a). The corresponding KPFM image reveals a higher response inside the spherulites than at the grain boundary, which is related to the decreasing of the work function of the PLLA film affected by the edge conditions (Figure 51.b). The acquired high-resolution scan images ($5 \times 5 \mu\text{m}^2$) demonstrate the only homogenous KPFM signal distribution (Figure 51.d). This result confirms the equal work function values for all the fibril structure of the PLLA film.

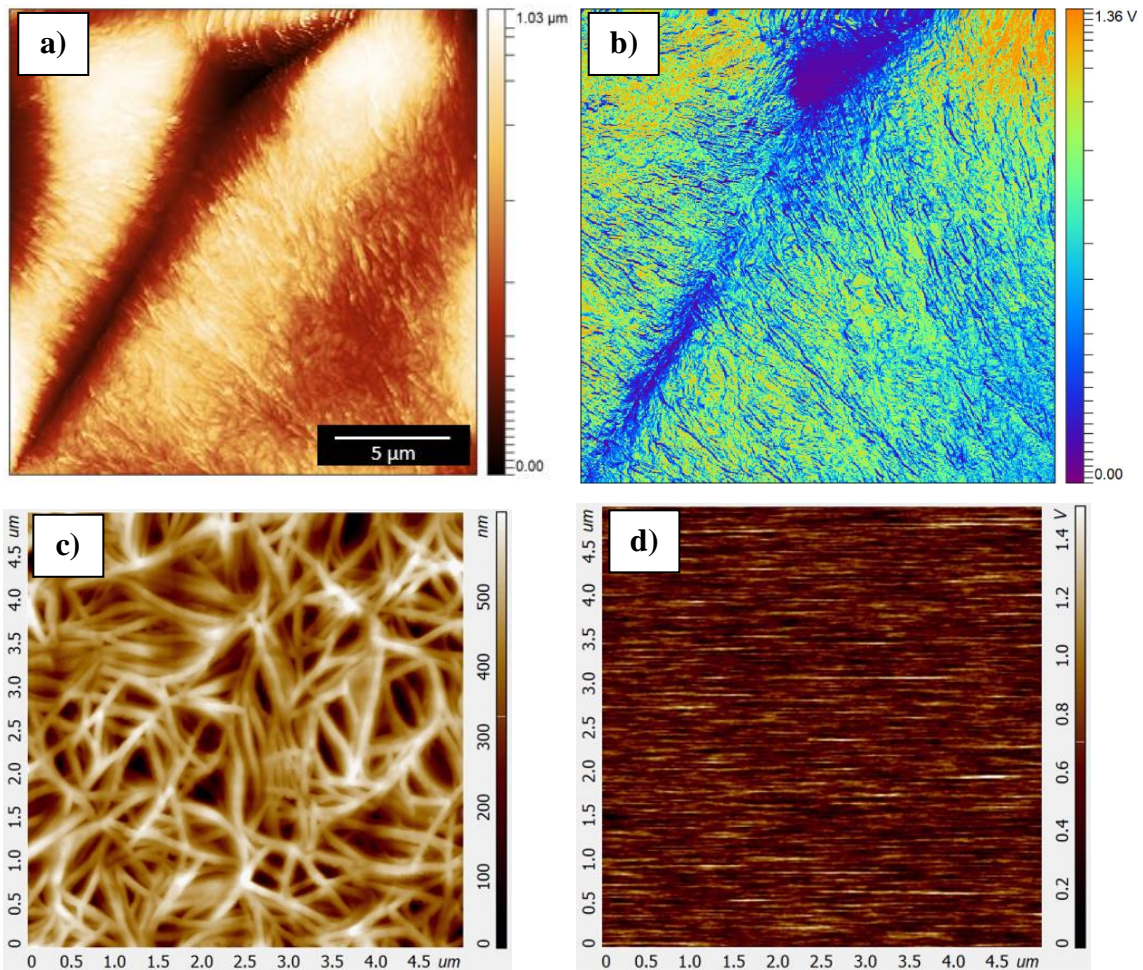


Figure 51. KPFM scan images of the PLLA film surface: (a, c) topography, (b, d) surface potential distribution.

The KPFM responses of spin-coated PLLA films, 5 wt % poly (L-lactic) acid in 1,4-dioxane solution, covering Pt/TiO₂/SiO₂/Si substrate, were studied by Barroca, N. *et al.* The films, with thickness ranging from 3 to 6 μm, were crystallized at 80 °C for 30 min. It was observed that the surface potential ranged from -0.35 V to 2.5V, after electrical poling with *dc* field from -10 V to +10 V [140].

Piezoresponse Force Microscopy (PFM)

In order to confirm the piezo- and ferroelectric activities of the PLLA film, the PFM approach was used. The physical rotation of the sample during the PFM scan displays correlated piezoelectric images that are in good agreement with the share components of the piezoelectric tensors d_{31} and d_{14} [29][163]. Thus, the results of the PFM scan of spherulite's grain boundary under different azimuthal scan angle (0°, 90°, 180°, and 360°) demonstrate alteration of the out-of-plane and in-plane PFM responses

after each iteration of the rotation (Figure 52). However, the 0° and 360° steps show the equal out-of-plane and in-plane PFM responses, thus revealing resumption to the initial polarization state and strong piezoelectric behaviour on the sample.

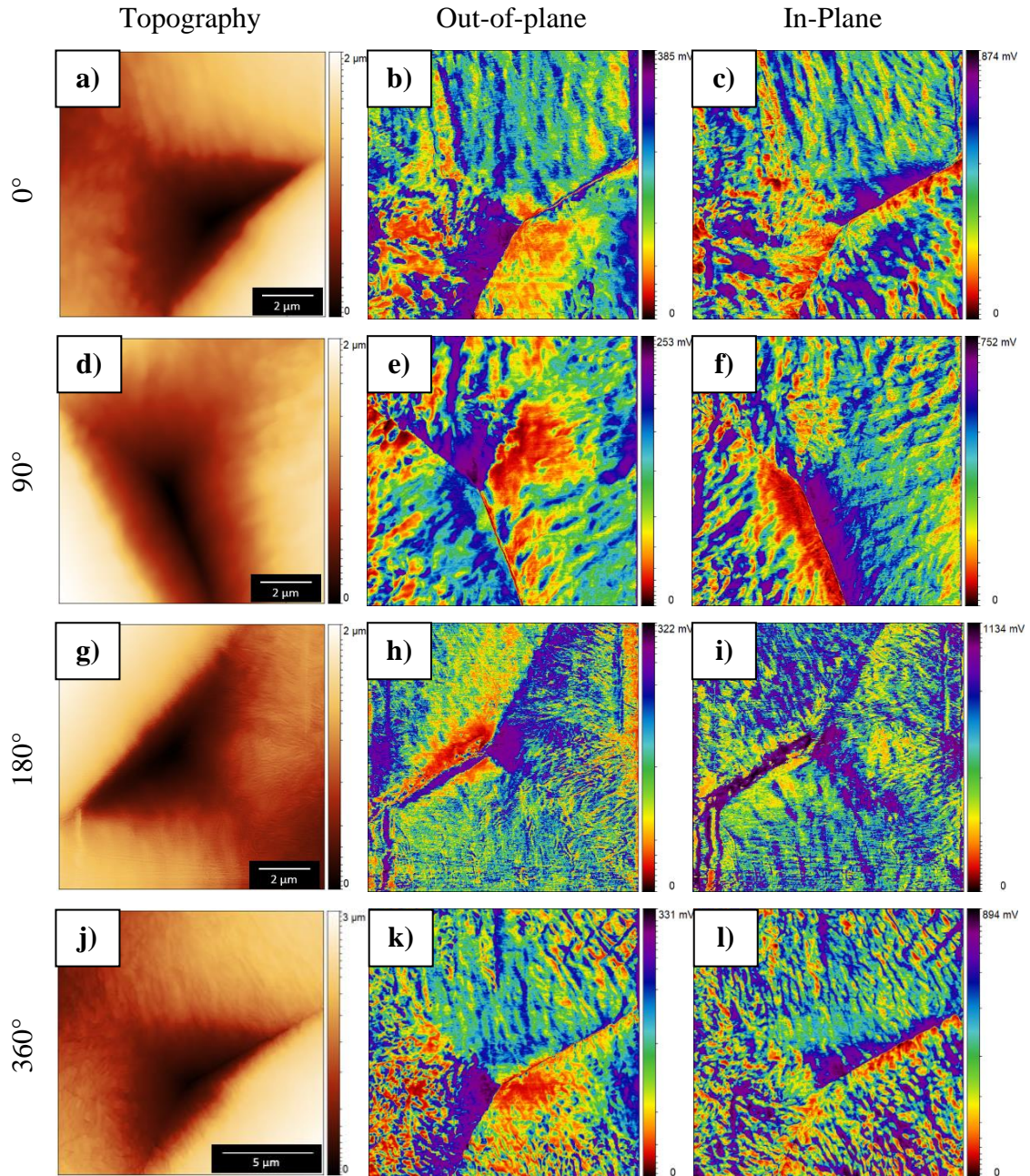


Figure 52. PFM scan images of spherulite's grain boundary under rotation: a, d, g, j) topography, b, e, h, k) out-of-plane and c, f, i, l) in-plane responses.

The PFM scan images done on a non-poled area ($10 \times 10 \mu\text{m}^2$) show correlated out-of-plane and in-plane responses that indicate on local ferroelectric nature of the samples (Figure 53.a-c). An application of *dc* BV (± 40 V) in agreement with the pattern

shown in Figure 53.d results in a strong poling behavior of the sample's surface. The induced polarization states follow the sign of the applied voltage (Figure 53.d-f) and properly correlated out-of-plane and in-plane PFM signals, thus confirming the robust macroscopic piezoelectric nature of the PLLA film. Moreover, the box-in-box poling pattern yields the ability in the change of polarization states (i.e., depolarization behavior). The combined EFM and KPFM measurements confirm the electrophysical activity of the samples' surface (Figure 53.g-h). The EFM image shows the surface charge density storage independently on the applied voltage, while the KPFM image demonstrates distinct differences in work functions with respect to *dc* BV polarity.

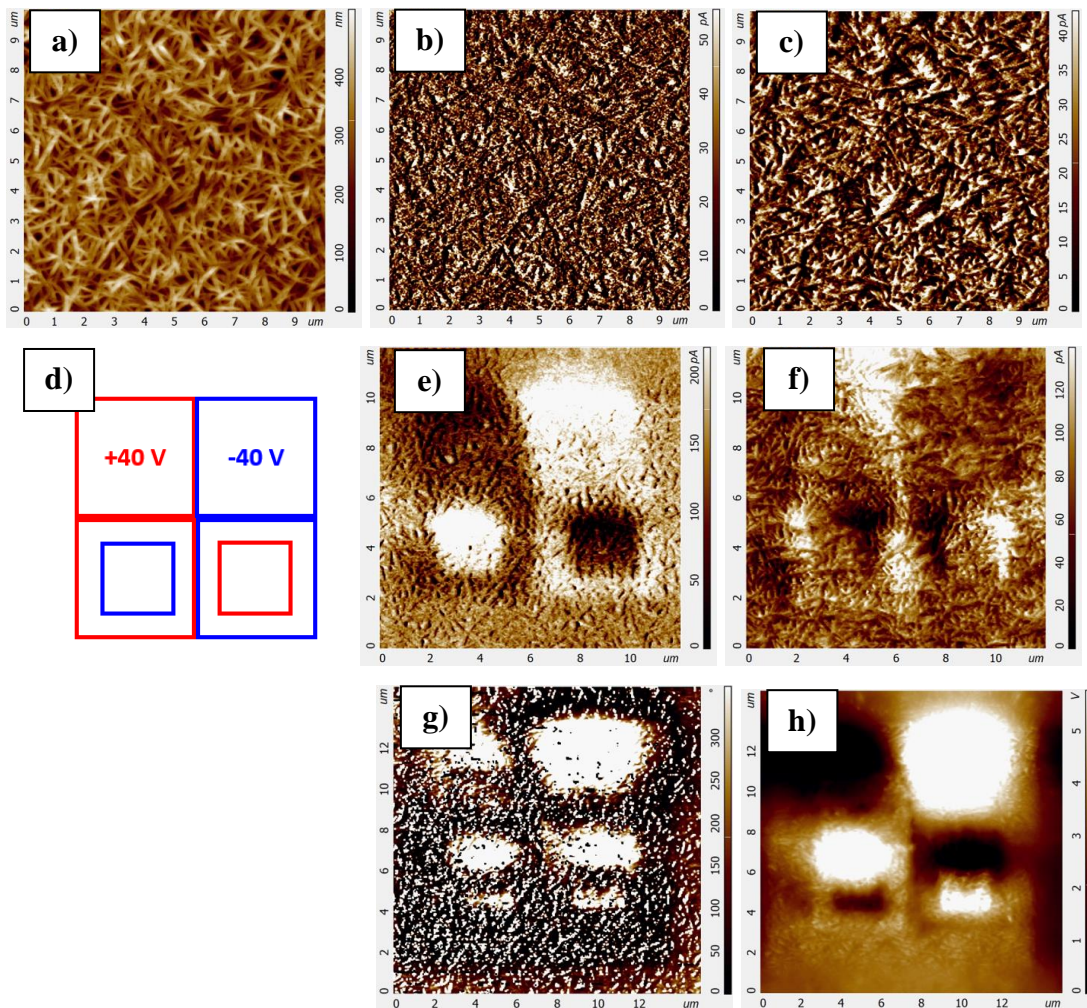


Figure 53. PFM, EFM, and KPFM scan images: (a) topography, (b,c) out-of-plane and in-plane PFM responses of the non-poled area, (d) *dc* BV (± 40 V) poling pattern, (e-f) out-of-plane and in-plane PFM responses of the poled area, (g) electrostatic and (h) surface potential distributions.

The cross-section analysis was applied to the out-of-plane and in-plane PFM phase images of the poled area (Figure 54). Here, the differences in phase indicate differences in induced polarization orientation [132].

Figure 54.a shows yellow and green profile lines, where the phase difference between out-of-plane positive and negative domains is 28° and the phase difference between out-of-plane positive and negative domains of the box-in-box pattern is 14° . Figure 54.b represents red and blue profile lines, where the phase difference between in-plane positive and negative domains is 15° and the phase difference between in-plane positive and negative domains of the box-in-box pattern is 17° . The comparison of these results points to the immense impact of the size of the polling area on the width of the induced domain wall (Figure 54.b). Both planes have their polarization direction changed according to the local poling. Dipolar orientation in PLLA corresponds to the internal rotation of polar groups linked to asymmetric carbon atoms in the molecular chain [140].

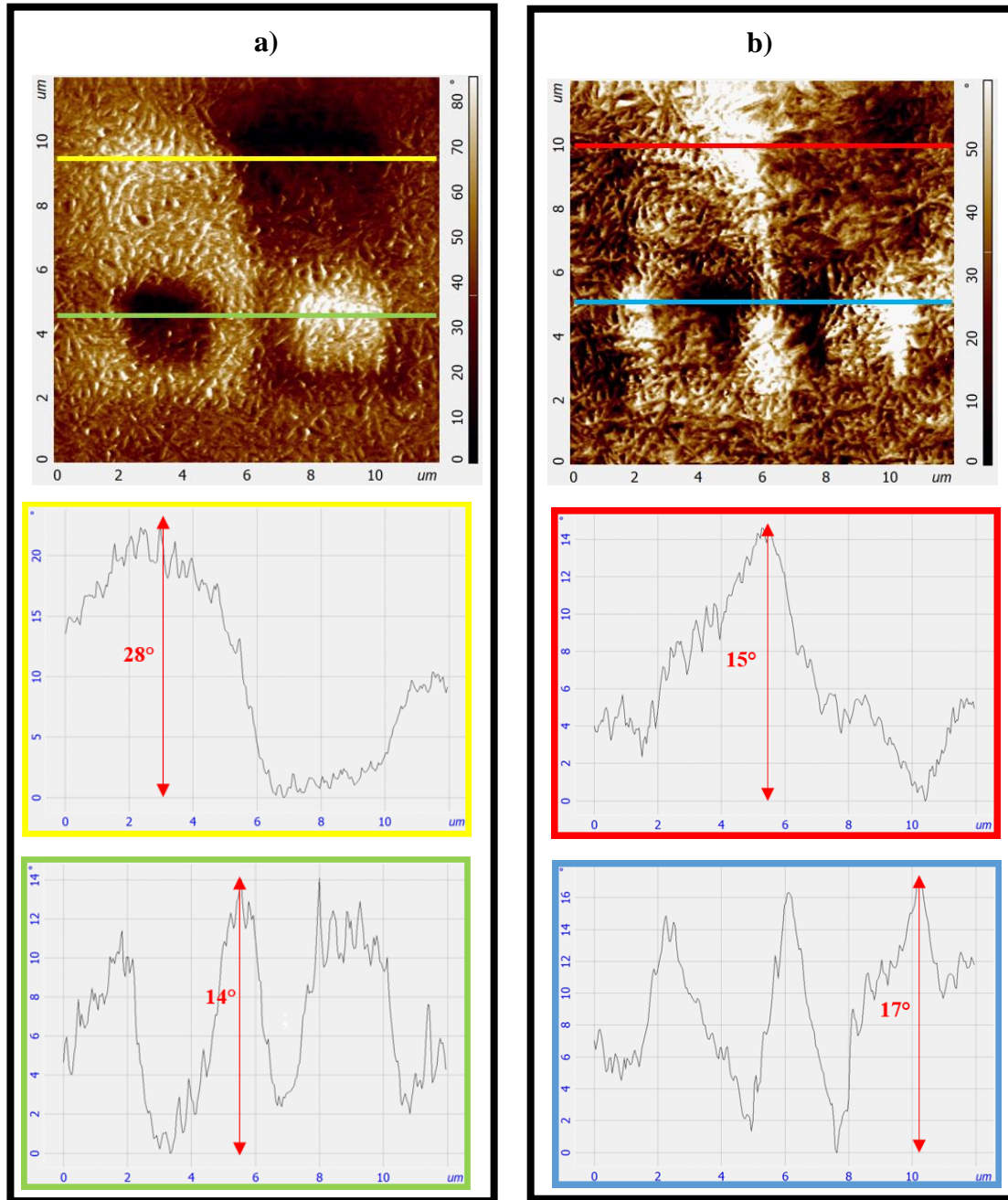


Figure 54. Cross-sections of PFM (a) out-of-plane and (b) in-plane phase images.

The PFM responses of spin-coated PLLA films, 5 wt % poly (L-lactic) acid in 1,4-dioxane solution, covering Pt/TiO₂/SiO₂/Si substrate, were studied by Barroca, N. *et al.* [140]. The films, with 7 μm of thickness, were melted for 30 min at 190 $^{\circ}\text{C}$ and crystallized for 30 min at 80 $^{\circ}\text{C}$. The poling was made with ± 5 V, ± 20 V, and ± 40 V. When ± 5 V was applied, no piezoresponse was detected, but, for ± 20 V and ± 40 V, phase differences of 172 $^{\circ}$ and 180 $^{\circ}$ were achieved, between the domains poled with opposite polarity, respectively.

4.10 Cytocompatibility

The Presto Blue™ viability and the osteogenic differentiation assay were performed in SS316L TT/SIL and SS316L TT/SIL/PLLA samples. A positive control group with cells and without biomaterial (CONTROL) was also studied. SEM micrographs after osteogenic differentiation assay verified the presence of cells on both samples.

Statistical analysis was performed using GraphPad Prism version 6.00 for Mac OS x, GraphPad Software (La Jolla California, USA). The experiments were performed in quadruplicates and the results are presented as Mean \pm Standard Error of the Mean. The analysis was performed by One-Way ANOVA analysis with Tukey multi comparison test. Differences were considered statistically significant at $p \leq 0.05$. Results significance are presented through the symbol (*), according to the p-value, with one, two, three or four symbols, corresponding to $0.01 < p \leq 0.05$; $0.001 < p \leq 0.01$; $0.0001 < p \leq 0.001$, and $p \leq 0.0001$, respectively.

Presto Blue™ viability assay

The cytocompatibility of the SS316L TT/SIL, the SS316L TT/SIL/PLLA, and the CONTROL group was evaluated by Presto Blue™ assay. Corrected absorbance was collected at every time-point (24, 72, 120, and 168 hours). The results and their deviation values are presented in Figure 55.

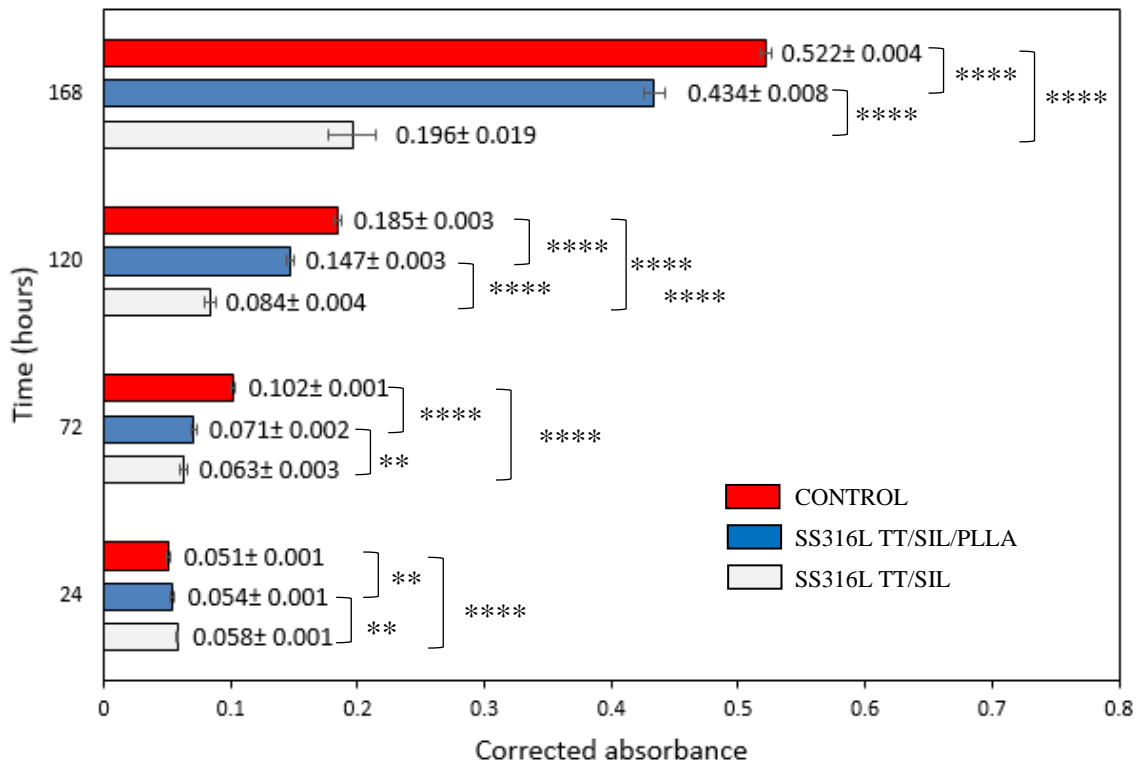


Figure 55. Corrected absorbance for different groups at every time-point (Mean ± Standard Error). Differences were considered statistically significant at $p \leq 0.05$, and expressed by * ($0.01 < p \leq 0.05$), ** ($0.001 < p \leq 0.01$), *** ($0.0001 < p \leq 0.001$) and **** ($p \leq 0.0001$).

The Presto Blue™ viability assay confirmed the biomaterials cytocompatibility. The viability of the SS316L TT/SIL/PLLA group, after 168 h, was 121.43 % higher than the SS316L TT/SIL group, proving that the PLLA film increases the cytocompatibility of the substrates. However, the control group, with no biomaterial, presented the best compatibility results. Its viability, after 168 h, was 166.33 % and 20.28 % higher than the SS316L TT/SIL and the SS316L TT/SIL/PLLA samples, respectively.

Osteogenic differentiation assay

The calcium deposition (mineralization) on the SS316L TT/SIL, the SS316L TT/SIL/PLLA, and the CONTROL group was evaluated by osteogenic differentiation and Alizarin Red S (ARS) assay after 21 days. The results and their deviation values are presented in Figure 56.

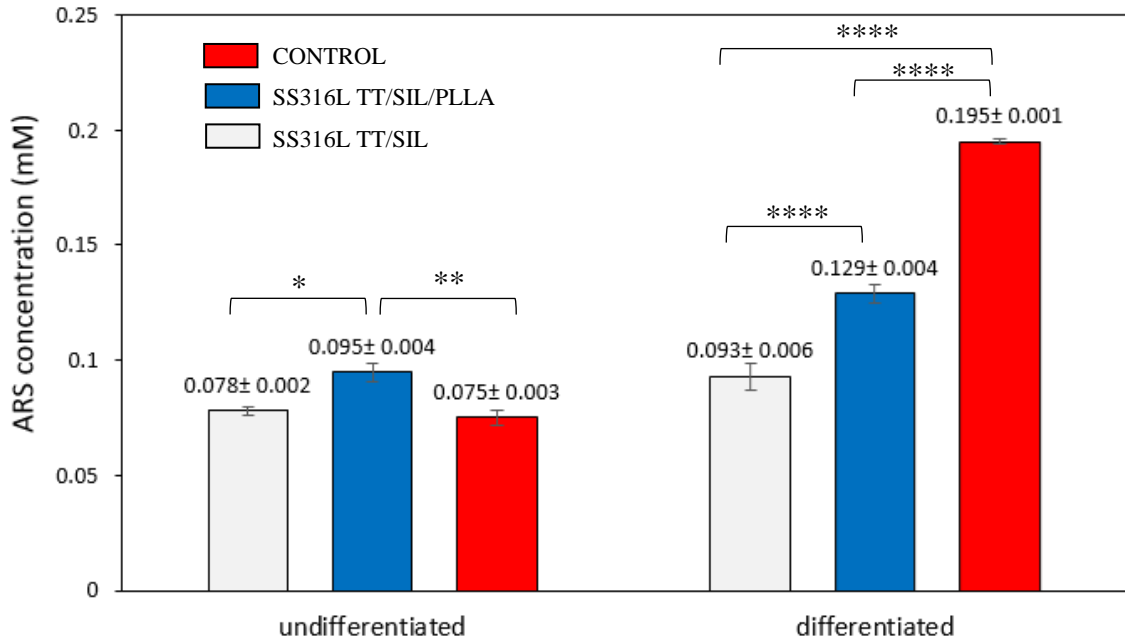


Figure 56. ARS concentration (mM) for undifferentiated and differentiated groups after 21 days (Mean \pm Standard Error). Differences were considered statistically significant at $p \leq 0.05$, and expressed by * ($0.01 < p \leq 0.05$), ** ($0.001 < p \leq 0.01$), *** ($0.0001 < p \leq 0.001$) and **** ($p \leq 0.0001$).

The calcium deposition of the undifferentiated and differentiated SS316L TT/SIL/PLLA group, after 21 days, was 21.79 % and 38.71 % higher than the SS316L TT/SIL group, respectively. It proves that PLLA film enhances the innate osteogenic potential of the cells and the osteogenic differentiation. However, the control group also presented the best mineralization results. Its calcium deposition, after 21 days, was 109.68 % and 51.16 % higher than the SS316L TT/SIL and the SS316L TT/SIL/PLLA samples, respectively.

Scanning Electronic Microscopy (SEM)

The SS316L TT/SIL and SS316L TT/SIL/PLLA samples without (unseeded) and with undifferentiated and differentiated cells were observed by SEM on different magnifications. The results are presented in Figure 57 and Figure 58.

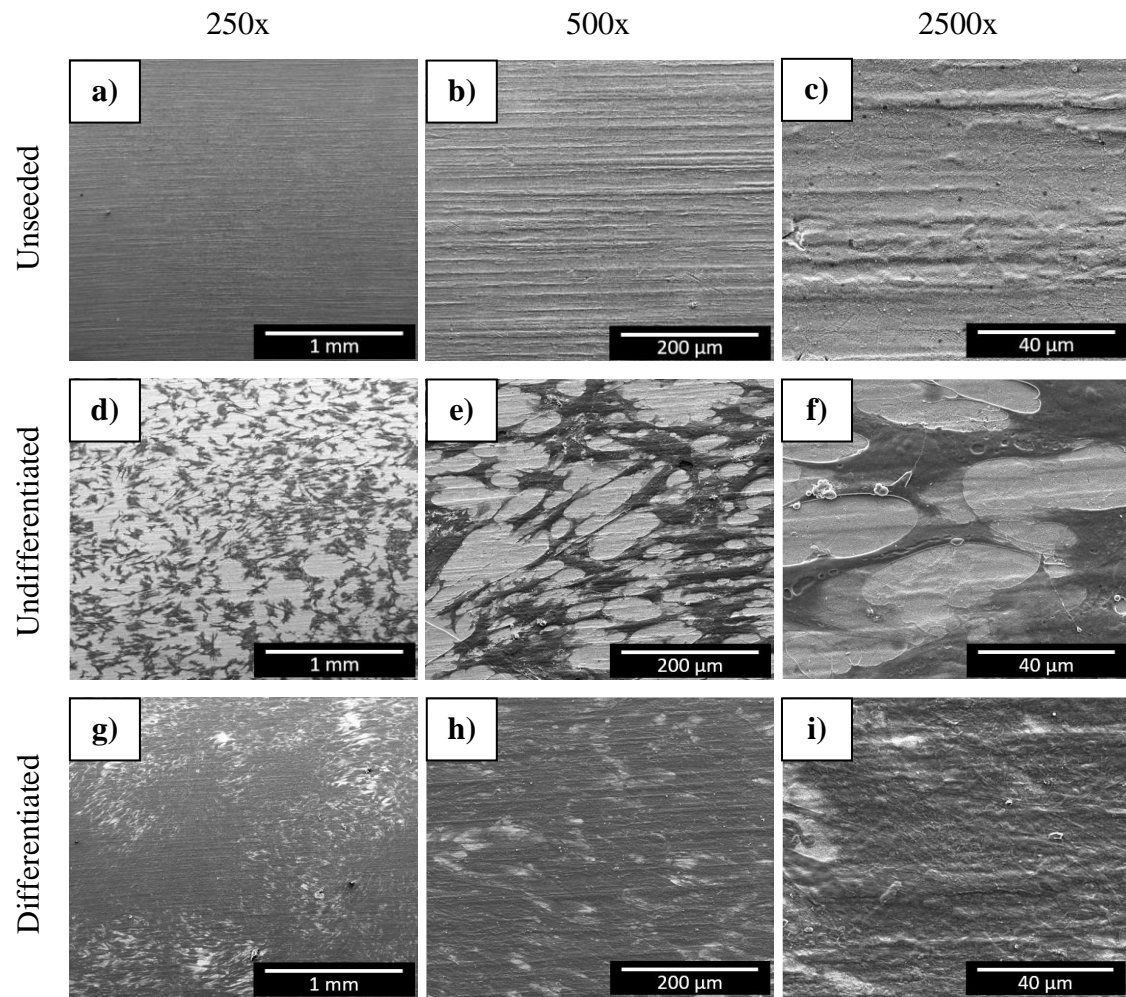


Figure 57. SEM images for the SS316L TT/SIL samples. a-c) unseeded group (no cells), d-f) seeded undifferentiated cells group, and g-i) seeded differentiated cells group. All groups were observed on different magnifications (250x, 500x, and 2500x).

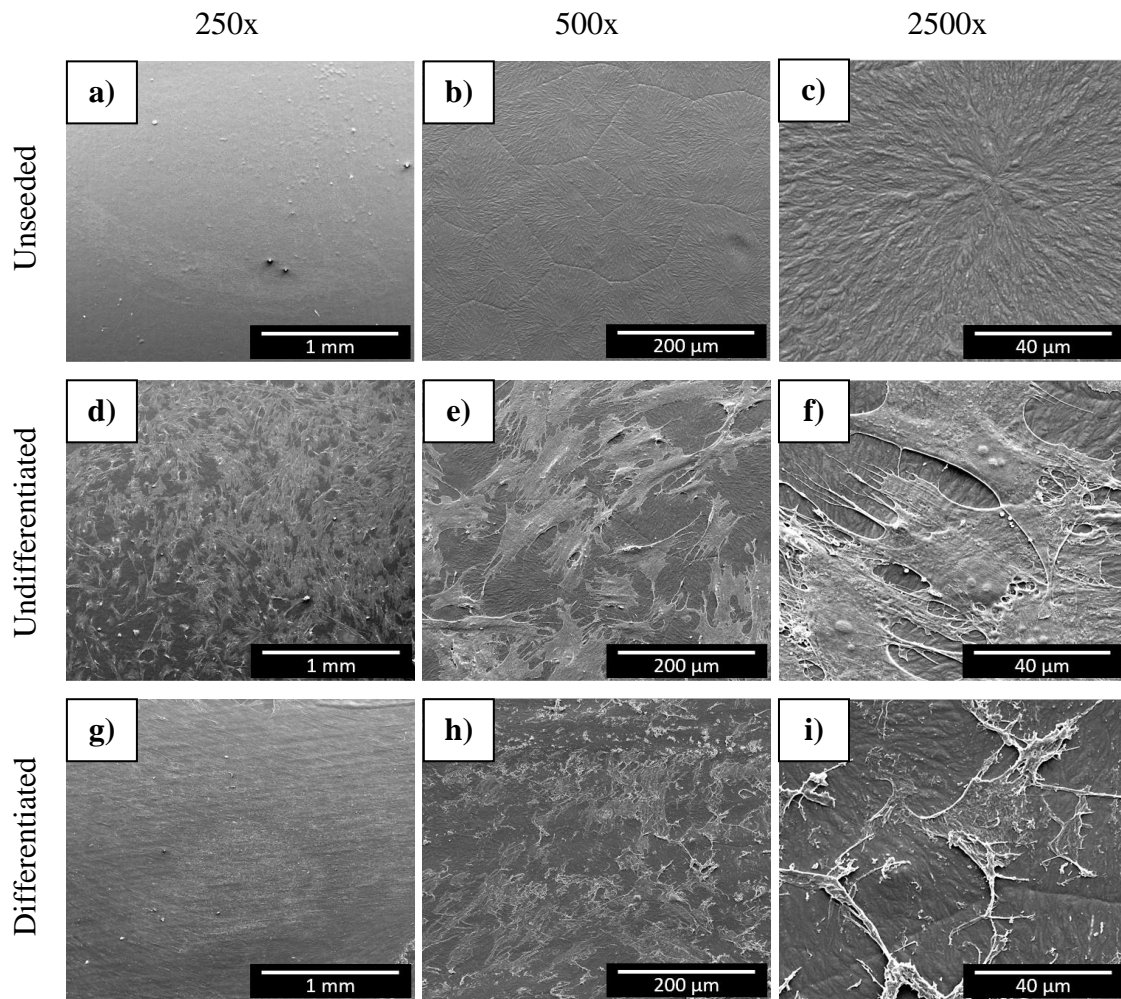


Figure 58. SEM images for the SS316L TT/SIL/PLLA samples. a-c) unseeded group (no cells), d-f) seeded undifferentiated cells group, and g-i) seeded differentiated cells group. All groups were observed on different magnifications (250x, 500x, and 2500x).

The SEM images allowed seeing the presence of fibroblast cells on both biomaterials. The differences in cell appearance in SS316L TT/SIL and SS316L TT/SIL/PLLA samples are due to the differences in the topography of these materials. These cells presented normal morphology and layer formation. Besides, differentiated cells show a tendency to form aggregates, which is expected in the osteogenic lineage.

The cytocompatibility of extruded magnesium rod coated with PLLA films of 5 wt % poly (L-lactic) acid in chloroform solution was studied by Xu, L. and Yamamoto, A. [148]. The polymer films with 3 layers were prepared by spin-coating. The attachment and proliferation of human osteosarcoma cells (Saos-2) on the polymer-coated

magnesium rod is higher than on the uncoated rod, proving that the PLLA films can maintain the biological functions of the cultured cells and had a good cytocompatibility.

The cytocompatibility and the mineralization of spin-coated PLLA films with 5 wt % poly (L-lactic) acid in 1,4-dioxane solution and 6 μm thickness were evaluated by Barroca, N. [140]. The films were melted for 30 min at 190 °C and crystallized for 30 min at 80 °C. Cell viability/proliferation was performed after 1, 4, 9, and 12 days of HUVEC cell culture. The results demonstrate cytocompatibility in non-poled and poled PLLA films, but cell growth is higher on poled samples. MC3T3 cells were seeded on the films and the mineralization was induced by the addition of osteogenic supplements. After 7, 14, and 21 days of cell culture exposure to differentiation medium, the culture was tested for calcium deposition using Alizarin Red S (ARS). The results showed that all PLLA films, poled and non-poled, induce a noticeable formation of calcium nodules comparing to the control group (with cells and without biomaterial), suggesting that PLLA films favor the differentiation of osteoblasts.

CHAPTER V
CONCLUSIONS AND FUTURE WORK

CHAPTER V - CONCLUSIONS AND FUTURE WORK

5.1 Conclusions

The FTIR, XRD, and tape test results proved that the production of stainless steel 316L covered with PLLA films had been carried out effectively, using the methodologies from Magueta, A [18]. As expected, chromium oxide was identified in SS316L TT samples, siloxanes in SS316L TT/SIL samples, and organic molecules in SS316L TT/SIL/PLLA samples using FTIR. The XRD analyses confirmed that the thermal treatment did not change the crystal structure of the substrates and the crystallographic plans of PLLA films correspond to α form. The efficiency of the silanization process in promoting the adhesion of PLLA film and SS316L substrate was proved using the tape test. The percentage of the area removed was 0 % and the spherulite morphology did not change after the test.

The influence of all steps from the production of SS316L TT/SIL/PLLA sample on surface roughness was studied. Based on the statistical analysis, the thermal treatment increased the arithmetic mean roughness (R_A) and mean roughness depth (R_Z) of the SS316L substrates by 93.75 % and 59.83 %, respectively, suggesting that the temperature used in this treatment permitted the intergranular corrosion. However, the silanization process did not change significantly the roughness and the PLLA films decreased the R_A and R_Z of the SS316L SIL sample by 59.38 % and 52.79 %, respectively. This technique also allowed calculating the PLLA film thickness of $4.78 \pm 1.21 \mu\text{m}$, based on maximum roughness depth (R_{MAX}).

The PLLA films were also studied using SEM, contact angle, and DSC techniques. Big spherulites with heterogeneous size distribution were observed using SEM. The mean size of 628 spherulites diameters was $88.86 \pm 1.72 \mu\text{m}$. PLLA film surface was considered little hydrophilic due to the high contact angle with water ($83.48 \pm 1.94^\circ$) and its surface energy, determined with OWRK-model, was 39.70 mJ/m^2 . Also, the glass transition (T_g), the melting temperature (T_m), and the crystallization (T_c) temperatures were determined using DSC analyses, being their values 60.4°C , 179.4°C , and 73.0°C , respectively. The degree of crystallization was 48.81 %.

The dielectric response of PLLA films under an applied electric field was studied as a function of temperature and frequency using impedance spectroscopy. The

temperature rise increased the relative permittivity (ϵ_r)/polarization (P). The α segmental relaxation in PLLA films occurred between 60 °C and 100 °C and was presented as a significant increase in ϵ_r and a peak in dielectric loss tangent ($\tan(\delta)$). The rise in frequency decreased ϵ_r but increased $\tan(\delta)$. The resistivity (ρ) results showed that the higher the temperature and the higher the frequency, the lower the resistivity.

Using the AFM approach, the distinct difference between the SS316L substrate and the PLLA film was measured. The PLLA film with a thickness of 4.4 μm , consisting of the spherulites with the fibril structure, was studied. The fibril structure stack up in a uniform form factor with a roughness of about 200 nm thus composing the spherulites with a diameter of about 60 μm , a high roughness of about 2 μm , and a grain boundary width of about 2-5 μm .

The EFM response reveals phase separation associated with the morphological properties of the fibril structure. The potential differences observed in the fibril structure, correspond to the meaningful influence of electrostatic forces and the electrostatic charges that can be rearranged in different ways according to the applied voltage. The KPFM response reveals the surface potential distribution (i.e., work function) is homogeneous under the fibril structure (i.e., inside the spherulites) while demonstrates a distinct difference between spherulites and the grain boundaries.

In order to confirm the piezo- and ferroelectric activities of the PLLA films, the PFM mode was utilized. The response of intrinsic-related PFM out-of-plane and in-plane signals of the non-poled area were measured thus indicating the ferroelectric nature of the samples at the local scale level. The application of *dc* BV voltage shown the polarization following the sign of the electric field for both signals thus indicating the piezoelectric nature of the PLLA film at the macroscopic scale level. This piezoelectric behavior of the sample was verified when a rotation procedure was applied, indicating out-of-plane and in-plane PFM responses to be changed for 90° and 180° scan angles but shown resumption to the initial polarization state for 360°.

The Presto Blue™ viability assay showed that the viability of the SS316L TT/SIL/PLLA group, after 168 h, was 121.43 % higher than the SS316L TT/SIL group, proving that the PLLA films increased the cytocompatibility of the substrates. Osteogenic differentiation assay showed that the calcium deposition on the undifferentiated and differentiated SS316L TT/SIL/PLLA group, after 21 days, was 21.79 % and 38.71 % higher than the SS316L TT/SIL group, respectively, proving that PLLA films enhance

the innate osteogenic potential of the cells and the osteogenic differentiation. In addition, the SEM images allowed seeing the presence of fibroblast cells with normal morphology and layer formation on both biomaterials. As expected, the differentiated cells formed aggregates. Analyzing the cytocompatibility test results, it was possible to conclude that the functional device developed in this work has a good potential for bone tissue engineering application.

5.2 Future work

The biocompatibility test is under development by the University of Porto (UP), in collaboration with the project “Advanced BioMEMs for Tissue Engineering: Applications in Hard Tissues (BioMEMs)”. The coated substrates will be implanted subcutaneously in adult male rats and the biocompatibility will be subsequently analyzed for inflammatory events, presence or absence of foreign body reaction and fibrosis, and tissue ingrowth after 3, 7, and 14 days.

The study of the cytocompatibility and biocompatibility of stainless steel 316L substrates covered with poled PLLA films is interesting. Barroca, N observed that negatively and positively poled PLLA films promote larger mineralization of the human bone marrow cells than non-poled PLLA films [140]. The adhesion and proliferation of osteoblast cells can be increased changing the spherulite size, crystallinity, surface roughness, wettability, and surface free energy. Thus, the improvement of these properties in stainless steel 316L substrates covered with PLLA films is also crucial in future works.

BIBLIOGRAPHY

BIBLIOGRAPHY

- [1] M. M. Stevens, “Biomaterials for bone tissue engineering,” *Mater. Today*, vol. 11, no. 5, pp. 18–25, 2008.
- [2] M. Gutierrez, M. Ascensão Lopes, N. Sooraj Hussain, A. Trigo Cabral, L. Almeida, and J. Domingos Santos, “Substitutos ósseos: Conceitos gerais e estado actual,” *Arq. Med.*, vol. 19, no. 4, pp. 153–162, 2005.
- [3] W. Wang, Y. Ouyang, and C. K. Poh, “Orthopaedic implant technology: Biomaterials from past to future,” *Ann. Acad. Med. Singapore*, vol. 40, no. 5, pp. 237–243, 2011.
- [4] S. B. Goodman, Z. Yao, M. Keeney, and F. Yang, “The future of biologic coatings for orthopaedic implants,” *Biomaterials*, vol. 34, no. 13, pp. 3174–3183, 2013.
- [5] M. M. Saleh, M. M. Saleh, A. H. Touny, and M. A. Al-Omair, “Biodegradable/biocompatible coated metal implants for orthopedic applications,” *Biomed. Mater. Eng.*, vol. 27, no. 1, pp. 87–99, 2016.
- [6] S. A. Omar, J. Ballarre, and S. M. Ceré, “Protection and functionalization of AISI 316 L stainless steel for orthopedic implants: hybrid coating and sol gel glasses by spray to promote bioactivity,” *Electrochim. Acta*, vol. 203, no. 2015, pp. 309–315, 2016.
- [7] E. Salahinejad, M. J. Hadianfard, D. D. Macdonald, S. Sharifi, M. Mozafari, K. J. Walker, A. Tahmasbi Rad, S. V. Madihally, D. Vashaei, and L. Tayebi, “Surface modification of stainless steel orthopedic implants by sol-gel ZrTiO₄ and ZrTiO₄-PMMA coatings,” *J. Biomed. Nanotechnol.*, vol. 9, no. 8, pp. 1327–1335, 2013.
- [8] A. Das and M. Shukla, “Surface morphology, bioactivity, and antibacterial studies of pulsed laser deposited hydroxyapatite coatings on Stainless Steel 254 for orthopedic implant applications,” *Proc. Inst. Mech. Eng. Part L J. Mater. Des. Appl.*, vol. 233, no. 2, pp. 120–127, 2019.
- [9] E. Fukada and I. Yasuda, “On the Piezoelectric Effect of Bone,” *J. Phys. Soc. Japan*, vol. 12, no. 10, 1957.
- [10] M. Pawlikowski, “Biomaterial Investigation of Apatite Piezoelectricity,” *Traumatol. Orthop. Russ.*, vol. 22, no. 2, pp. 57–63, 2016.
- [11] M. Pawlikowski, “Electric Phenomenon in Bones as a Result of Piezoelectricity of Hydroxyapatite,” *Arch. Clin. Biomed. Res.*, vol. 01, no. 03, pp. 132–139, 2017.
- [12] M. Ecol, “Biomaterial strategies for engineering implants for enhanced osseointegration and bone repair Rachit,” vol. 25, no. 5, pp. 1032–1057, 2017.
- [13] S. D. Yoon, Y. S. Kwon, and K. S. Lee, “Biodegradation and biocompatibility of poly L-lactic acid implantable mesh,” *Int. Neurolog. J.*, vol. 21, pp. 48–54, 2017.
- [14] N. B. Barroca, A. L. Daniel-Da-Silva, P. S. Gomes, M. H. R. Fernandes, S. Lanceros-Méndez, P. Sharma, A. Gruverman, M. H. V. Fernandes, and P. M. Vilarinho, “Suitability of PLLA as piezoelectric substrates for tissue

- engineering evidenced by microscopy techniques,” *Microsc. Microanal.*, vol. 18, no. SUPPL.5, pp. 63–64, 2012.
- [15] J. D. Venables, “Adhesion and durability of metal-polymer bonds,” *J. Mater. Sci.*, vol. 19, no. 8, pp. 2431–2453, 1984.
- [16] G. Ramathnam, M. Libertucci, M. Sadowski, and T. North, “Joining of polymers to metal,” *Weld. J.*, vol. 71, no. 12, p. 483, 1992.
- [17] G. Da Ponte, A. K. Ghosh, A. Kakaroglou, D. Van Hemelrijck, B. Van Mele, and B. Verheyde, “Adhesion improvement between epoxy and stainless steel using a silane coupling agent in an atmospheric plasma process,” *Plasma Process. Polym.*, vol. 12, no. 4, pp. 347–361, 2015.
- [18] A. Magueta, “Biomedical microelectromechanical (BioMEMs) systems to tissue engineering: applications in hard tissues,” Master's thesis, Universidade de Aveiro, 2018.
- [19] M. Honkanen *et al.*, “Characterization of silane layers on modified stainless steel surfaces and related stainless steel-plastic hybrids,” *Appl. Surf. Sci.*, vol. 257, no. 22, pp. 9335–9346, 2011.
- [20] J. Betts, K. Young, and J. A. Wise, “Chapter 6: Bone Tissue and the Skeletal System,” in *Anatomy & Physiology*, Texas (EUA): OpenStax College, pp. 203–238, 2013.
- [21] C. VanPutte, J. Regan, and A. Russo, “Chapter 6: Skeletal System: Bones and Joints,” in *Seeley's Essential of Anatomy & Physiology*, 9th ed., New York (EUA): McGraw-Hill Education, pp. 110–149, 2016.
- [22] D. J. Hadjidakis and I. I. Androulakis, “Bone remodeling,” *Ann. N. Y. Acad. Sci.*, vol. 1092, pp. 385–396, 2006.
- [23] H. M. Frost, “Wolff's Law and bone's structural adaptations to mechanical usage: an overview for clinicians.,” *Angle Orthodontist*, vol. 64, no. 3, pp. 175–188, 1994.
- [24] O. M. Pearson and D. E. Lieberman, “The aging of Wolff's 'law': Ontogeny and responses to mechanical loading in cortical bone,” *Yearb. Phys. Anthropol.*, vol. 47, pp. 63–99, 2004.
- [25] J. Singh, S. Rani, Rohini, and A. Parida, “Generation of piezoelectricity from the human body,” *2014 Annu. Int. Conf. Emerg. Res. Areas Magn. Mach. Drives, AICERA/iCMMMD 2014 - Proc.*, pp. 1–5, 2014.
- [26] P. M. Vilarinho, “Functional Materials: Properties, Processing and Applications,” *Scanning Probe Microsc. Charact. Nanofabrication Device Appl. Funct. Mater.*, pp. 3–33, 2005.
- [27] R. S. Dahiya and M. Valle, “Appendix A: Fundamentals of Piezoelectricity,” in *Robotic Tactile Sensing*, 1st ed., Dordrecht: Springer Netherlands, pp. 195–210, 2013.
- [28] S. Moheimani and A. Fleming, “Fundamentals of Piezoelectricity,” in *Piezoelectric Transducers for Vibration Control and Damping*, London: Springer-Verlag, pp. 9–35, 2006.
- [29] A. International, “Piezoelectric constants,” 2016. [Online]. Available:

www.americanpiezo.com. [Accessed: 07-Nov-2020].

- [30] K. S. Ramadan, D. Sameoto, and S. Evoy, “A review of piezoelectric polymers as functional materials for electromechanical transducers,” *Smart Mater. Struct.*, vol. 23, no. 3, p. 033001, 2014.
- [31] H. Kaczmarek, B. Królikowski, E. Klimiec, M. Chylińska, and D. Bajer, “Advances in the study of piezoelectric polymers,” *Russ. Chem. Rev.*, vol. 88, no. 7, pp. 749–774, 2019.
- [32] S. V Canevarolo, *Ciência dos Polímeros—Um Texto Básico Para Tecnólogos e Engenheiros*, 3rd ed. São Paulo, 2010.
- [33] E. J. Curry, K. Ke, M. T. Chorsi, K. S. Wrobel, A. N. Miller, A. Patel, I. Kim, J. Feng, L. Yue, Q. Wu, C.-L. Kuo, K. W.-H. Lo, C. T. Laurencin, H. Ilies, P. K. Purohit, and T. D. Nguyen, “Biodegradable Piezoelectric Force Sensor,” *Proc. Natl. Acad. Sci.*, vol. 115, no. 5, pp. 909–914, 2018.
- [34] P. Sarazin, X. Roy, and B. D. Favis, “Controlled preparation and properties of porous poly(l-lactide) obtained from a co-continuous blend of two biodegradable polymers,” *Biomaterials*, vol. 25, no. 28, pp. 5965–5978, 2004.
- [35] M. Honda, K. Hayashi, K. Morii, S. Kawai, Y. Morimoto, and Y. Tajitsu, “Piezoelectricity of Chiral Polymeric Fibers,” *Jpn. J. Appl. Phys.*, vol. 46, no. 10B, pp. 7122–7124, 2007.
- [36] K. Madhavan Nampoothiri, N. R. Nair, and R. P. John, “An overview of the recent developments in polylactide (PLA) research,” *Bioresour. Technol.*, vol. 101, no. 22, pp. 8493–8501, 2010.
- [37] S. Technologies, “Lactic acid.” [Online]. Available: www.sielc.com. [Accessed: 05-Nov-2020].
- [38] J. Gu and J. M. Catchmark, “Polylactic acid composites incorporating casein functionalized cellulose nanowhiskers,” *J. Biol. Eng.*, vol. 7, no. 1, p. 31, 2013.
- [39] P. P. Database, “Effect of morphology and chain polarity on dielectric properties.” [Online]. Available: polymerdatabase.com. [Accessed: 05-Nov-2020].
- [40] E. Castro-Aguirre, F. Iñiguez-Franco, H. Samsudin, X. Fang, and R. Auras, “Poly(lactic acid)—Mass production, processing, industrial applications, and end of life,” *Adv. Drug Deliv. Rev.*, vol. 107, pp. 333–366, 2016.
- [41] P. P. Database, “Electrical conductivity of conjugated polymers.” [Online]. Available: polymerdatabase.com. [Accessed: 05-Nov-2020].
- [42] D. E. Mihaiescu, A. M. Grumezescu, P. C. Balaure, D. E. Mogosanu, and V. Traistaru, “A review on giant piezoelectric coefficient, materials and applications,” *Biointerface Res. Appl. Chem.*, vol. 9, no. 5, pp. 4205–4216, 2019.
- [43] V. Sharapov, *Piezoceramic Sensors*. Berlin, Heidelberg: Springer Berlin Heidelberg, 2011.
- [44] A. Ehterami, M. Kazemi, B. Nazari, P. Saraeian, and M. Azami, “Fabrication and characterization of highly porous barium titanate based scaffold coated by Gel/HA nanocomposite with high piezoelectric coefficient for bone tissue engineering applications,” *J. Mech. Behav. Biomed. Mater.*, vol. 79, pp. 195–202, 2018.

- [45] P. Kaufmann, S. Röhrig, P. Supancic, and M. Deluca, "Influence of ferroelectric domain texture on the performance of multilayer piezoelectric actuators," *J. Eur. Ceram. Soc.*, vol. 37, no. 5, pp. 2039–2046, 2017.
- [46] X. Gao, J. Yang, J. Wu, X. Xin, Z. Li, X. Yuan, X. Shen, and S. Dong, "Piezoelectric Actuators and Motors: Materials, Designs, and Applications," *Adv. Mater. Technol.*, p. 1900716, 2019.
- [47] V. L. Stuber, D. B. Deutz, J. Bennett, D. Cannel, D. M. de Leeuw, S. van der Zwaag, and P. Groen, "Flexible Lead-Free Piezoelectric Composite Materials for Energy Harvesting Applications," *Energy Technol.*, vol. 7, no. 1, pp. 177–185, 2019.
- [48] C. Wu, Y. Tang, B. Mao, K. Zhao, S. Cao, and Z. Wu, "Rapid apatite induction of polarized hydrophilic HA/PVDF bio-piezoelectric coating on titanium surface," *Surf. Coatings Technol.*, vol. 405, p. 126510, 2021.
- [49] C. Wu, Y. Tang, K. Zhao, B. Mao, and X. Ru, "In situ synthesis of TiO₂/BaTiO₃ coaxial nanotubes coating on the titanium surface," *J. Alloys Compd.*, vol. 845, p. 156301, 2020.
- [50] W. Liu, X. Li, Y. Jiao, C. Wu, S. Guo, X. Xiao, X. Wei, J. Wu, P. Gao, N. Wang, Y. Lu, Z. Tang, Q. Zhao, J. Zhang, Y. Tang, L. Shi, and Z. Guo, "Biological Effects of a Three-Dimensionally Printed Ti6Al4V Scaffold Coated with Piezoelectric BaTiO₃ Nanoparticles on Bone Formation," *ACS Appl. Mater. Interfaces*, vol. 12, no. 46, pp. 51885–51903, 2020.
- [51] Y. Tang, C. Wu, P. Tian, K. Zhao, and Z. Wu, "Fabrication and induced mineralization of bio-piezoelectric ceramic coating on titanium alloys," *Ceram. Int.*, vol. 46, no. 3, pp. 4006–4014, 2020.
- [52] S. Rahmati, S; Basiriani, MB; Rafienia, M; Yaghini, J; Raeissi, K; Hosseini, S; Kabiri, "Characterization and in vitro evaluation of nanostructure barium titanate coating on Ti6Al4V," *J. Ceram. Process. Res.*, vol. 17, no. 5, pp. 434–438, 2016.
- [53] C. M. Lin and S. K. Yen, "Promotion of Bioactive and Corrosion Resistance by Electrolytic Piezoelectric Ceramic," *Key Eng. Mater.*, vol. 330–332, pp. 95–98, 2007.
- [54] R. Langer and J. Vacanti, "Tissue engineering," *Science (80-.)*, vol. 260, no. 5110, pp. 920–926, 1993.
- [55] D. Williams, J. Black, and P. Doherty, "Second consensus conference on definitions in biomaterials," in *Advances in Biomaterials*, vol. 10, 1992.
- [56] S. H. Kim and Y. Jung, "Resorbable polymers for medical applications," in *Biotextiles as Medical Implants*, Elsevier, pp. 91–112, 2013.
- [57] B. Ratner, A. Hoffman, F. Schoen, and J. Lemons, *Biomaterials Science: An Introduction to Materials in Medicine*, 2nd ed. London(UK): Elsevier Academic Press, 2004.
- [58] L. G. Griffith, "Tissue Engineering--Current Challenges and Expanding Opportunities," *Science (80-.)*, vol. 295, no. 5557, pp. 1009–1014, 2002.
- [59] J. Hubbell, "Bioactive biomaterials," *Curr. Opin. Biotechnol.*, vol. 10, no. 2, pp.

- 123–129, 1999.
- [60] D. W. Hutmacher, “Scaffolds in tissue engineering bone and cartilage,” *Biomaterials*, vol. 21, no. 24, pp. 2529–2543, 2000.
- [61] M. A. Woodruff, C. Lange, J. Reichert, A. Berner, F. Chen, P. Fratzl, J.-T. Schantz, and D. W. Hutmacher, “Bone tissue engineering: from bench to bedside,” *Mater. Today*, vol. 15, no. 10, pp. 430–435, 2012.
- [62] R. K. Schenk and D. Buser, “Osseointegration: a reality,” *Periodontol. 2000*, vol. 17, no. 1, pp. 22–35, 1998.
- [63] E. M. Bueno and J. Glowacki, *Biologic Foundations for Skeletal Tissue Engineering*, vol. 3, no. 1, 2011.
- [64] P. Fattahi, G. Yang, G. Kim, and M. R. Abidian, “A Review of Organic and Inorganic Biomaterials for Neural Interfaces,” *Adv. Mater.*, vol. 26, no. 12, pp. 1846–1885, 2014.
- [65] C. Wang, H. Hu, Z. Li, Y. Shen, Y. Xu, G. Zhang, X. Zeng, J. Deng, S. Zhao, T. Ren, and Y. Zhang, “Enhanced Osseointegration of Titanium Alloy Implants with Laser Microgrooved Surfaces and Graphene Oxide Coating,” *ACS Appl. Mater. Interfaces*, vol. 11, no. 43, pp. 39470–39483, 2019.
- [66] B. Ratner, A. Hoffman, F. Schoen, and J. Lemons, *Biomaterials Science*, 2nd ed. London(UK): Elsevier Academic Press, 2004.
- [67] B. Dhandayuthapani, Y. Yoshida, T. Maekawa, and D. S. Kumar, “Polymeric Scaffolds in Tissue Engineering Application: A Review,” *Int. J. Polym. Sci.*, vol. 2011, pp. 1–19, 2011.
- [68] P. Gunatillake, R. Mayadunne, and R. Adhikari, “Recent developments in biodegradable synthetic polymers,” *Biotechnol. Annu. Rev.*, vol. 12, pp. 301–347, 2006.
- [69] P. X. Ma, “Scaffolds for tissue fabrication,” *Mater. Today*, vol. 7, no. 5, pp. 30–40, 2004.
- [70] L. J. Chen and M. Wang, “Production and evaluation of biodegradable composites based on PHB–PHV copolymer,” *Biomaterials*, vol. 23, no. 13, pp. 2631–2639, 2002.
- [71] R. Ravichandran, S. Sundarrajan, J. R. Venugopal, S. Mukherjee, and S. Ramakrishna, “Advances in Polymeric Systems for Tissue Engineering and Biomedical Applications,” *Macromol. Biosci.*, vol. 12, no. 3, pp. 286–311, 2012.
- [72] C. Ribeiro, V. Sencadas, D. M. Correia, and S. Lanceros-Méndez, “Piezoelectric polymers as biomaterials for tissue engineering applications,” *Colloids Surfaces B Biointerfaces*, vol. 136, pp. 46–55, 2015.
- [73] K. Lee and S. B. Goodman, “Current state and future of joint replacements in the hip and knee,” *Expert Rev. Med. Devices*, vol. 5, no. 3, pp. 383–393, 2008.
- [74] A. Goharian and M. R. Abdullah, “Bioinert Metals (Stainless Steel, Titanium, Cobalt Chromium),” in *Trauma Plating Systems*, Elsevier, pp. 115–142, 2017.
- [75] A. S. Corporation, “Data Sheet 316/316L Stainless Steel,” 2018. [Online].

Available: www.aksteel.com. [Accessed: 01-Jul-2020].

- [76] Arcam, “Data Sheet Ti6Al4V Titanium Alloy.” [Online]. Available: www.arcam.com. [Accessed: 01-Jul-2020].
- [77] Arcam, “Data Sheet ASTM F75 CoCr Alloy.” [Online]. Available: www.arcam.com. [Accessed: 01-Jul-2020].
- [78] M. Fazel, H. R. Salimijazi, M. Shamanian, I. Apachitei, and A. A. Zadpoor, “Influence of hydrothermal treatment on the surface characteristics and electrochemical behavior of Ti-6Al-4V bio-functionalized through plasma electrolytic oxidation,” *Surf. Coatings Technol.*, vol. 374, pp. 222–231, Sep. 2019.
- [79] D. Ujino, H. Nishizaki, S. Higuchi, S. Komasa, and J. Okazaki, “Effect of Plasma Treatment of Titanium Surface on Biocompatibility,” *Appl. Sci.*, vol. 9, no. 11, p. 2257, 2019.
- [80] L. Jiang, S. Jin, S. Geng, C. Deng, Z. Lin, and B. Zhao, “Maintenance and Restoration Effect of the Surface Hydrophilicity of Pure Titanium by Sodium Hydroxide Treatment and its Effect on the Bioactivity of Osteoblasts,” *Coatings*, vol. 9, no. 4, p. 222, 2019.
- [81] T. Hanawa, “Titanium–Tissue Interface Reaction and Its Control With Surface Treatment,” *Front. Bioeng. Biotechnol.*, vol. 7, 2019.
- [82] A. Sobolev, A. Valkov, A. Kossenko, I. Wolicki, M. Zinigrad, and K. Borodianskiy, “Bioactive Coating on Ti Alloy with High Osseointegration and Antibacterial Ag Nanoparticles,” *ACS Appl. Mater. Interfaces*, vol. 11, no. 43, pp. 39534–39544, 2019.
- [83] L. Jia, F. Han, H. Wang, C. Zhu, Q. Guo, J. Li, Z. Zhao, Q. Zhang, X. Zhu, and B. Li, “Polydopamine-assisted surface modification for orthopaedic implants,” *J. Orthop. Transl.*, vol. 17, pp. 82–95, 2019.
- [84] G. Brunello, H. Elsayed, and L. Biasetto, “Bioactive Glass and Silicate-Based Ceramic Coatings on Metallic Implants: Open Challenge or Outdated Topic?,” *Materials (Basel)*, vol. 12, no. 18, p. 2929, 2019.
- [85] Y. Guo, J. Guan, H. Peng, X. Shu, L. Chen, and H. Guo, “Tightly adhered silk fibroin coatings on Ti6Al4V biometals for improved wettability and compatible mechanical properties,” *Mater. Des.*, vol. 175, p. 107825, 2019.
- [86] J. Ju, X. Peng, K. Huang, L. Li, X. Liu, C. Chitrakar, L. Chang, Z. Gu, and T. Kuang, “High-performance porous PLLA-based scaffolds for bone tissue engineering: Preparation, characterization, and in vitro and in vivo evaluation,” *Polymer (Guildf)*, vol. 180, p. 121707, 2019.
- [87] M. Degli Esposti, F. Chiellini, F. Bondioli, D. Morselli, and P. Fabbri, “Highly porous PHB-based bioactive scaffolds for bone tissue engineering by in situ synthesis of hydroxyapatite,” *Mater. Sci. Eng. C*, vol. 100, pp. 286–296, 2019.
- [88] P. K. Szewczyk, S. Metwally, Z. J. Krysiak, Ł. Kaniuk, J. E. Karbowniczek, and U. Stachewicz, “Enhanced osteoblasts adhesion and collagen formation on biomimetic polyvinylidene fluoride (PVDF) films for bone regeneration,” *Biomed. Mater.*, vol. 14, no. 6, p. 065006, 2019.

- [89] M. H. Nabavi, M. Salehi, A. Ehterami, F. Bastami, H. Semyari, M. Tehranchi, M. A. Nabavi, and H. Semyari, "A collagen-based hydrogel containing tacrolimus for bone tissue engineering," *Drug Deliv. Transl. Res.*, 2019.
- [90] G. Bracco and B. Holst, Eds., *Surface Science Techniques*, vol. 51. Berlin, Heidelberg: Springer Berlin Heidelberg, 2013.
- [91] K. Mittal, Ed., *Adhesion Measurement of Thin Films, Thick Films, and Bulk Coatings*. 100 Barr Harbor Drive, PO Box C700, West Conshohocken, PA 19428-2959: ASTM International, 1978.
- [92] V. Do, S.-W. Kim, M.-S. Kim, S. H. Lee, J. M. Ko, and W. I. Cho, "Combined Treatment on an Al Surface to Improve the Metal-Polymer Adhesion Strength," *J. Nanosci. Nanotechnol.*, vol. 20, no. 1, pp. 270–277, 2020.
- [93] A. Barrios, "Interfacial Adhesion of Polymer-Metal Composites," Bachelor's thesis, Worcester Polytechnic Institute, 2020.
- [94] S. Chanthapan, P. Wattanapornphan, C. Phongphisutthinan, Y. Kawahito, and T. Suga, "Effects of oxide layer on adhesion and durability of titanium and transparent polyamide joint by laser joining," *J. Laser Appl.*, vol. 30, no. 4, p. 042005, 2018.
- [95] L.-H. Lee, "Molecular Bonding and Adhesion at Polymer-Metal Interphases," *J. Adhes.*, vol. 46, no. 1–4, pp. 15–38, 1994.
- [96] C.-H. Lu, Y.-T. Kho, C.-P. Chen, B.-L. Tsai, and K.-N. Chen, "Adhesion and Material Properties Between Polyimide and Passivation Layers for Polymer/Metal Hybrid Bonding in 3-D Integration," *IEEE Trans. Components, Packag. Manuf. Technol.*, vol. 9, no. 3, pp. 412–418, 2019.
- [97] C. Song, Y. Yang, Y. Zhou, L. Wang, S. Zhu, J. Wang, R. Zeng, Y. Zheng, and S. Guan, "Electrochemical polymerization of dopamine with/without subsequent PLLA coating on Mg-Zn-Y-Nd alloy," *Mater. Lett.*, vol. 252, pp. 202–206, 2019.
- [98] Y. Sheng, L. Tian, C. Wu, L. Qin, and T. Ngai, "Biodegradable Poly(L-lactic acid) (PLLA) Coatings Fabricated from Nonsolvent Induced Phase Separation for Improving Corrosion Resistance of Magnesium Rods in Biological Fluids," *Langmuir*, vol. 34, no. 36, pp. 10684–10693, 2018.
- [99] D. Zhang, Z. Qi, H. Shen, B. Wei, Y. Zhang, and Z. Wang, "In vitro degradation and cytocompatibility of magnesium alloy coated with Hf/PLLA duplex coating," *Mater. Lett.*, vol. 213, pp. 249–252, 2018.
- [100] A. A. Shomali, R. J. Guillory, D. Seguin, J. Goldman, and J. W. Drelich, "Effect of PLLA coating on corrosion and biocompatibility of zinc in vascular environment," *Surf. Innov.*, vol. 5, no. 4, pp. 211–220, 2017.
- [101] M. Diez, M.-H. Kang, S.-M. Kim, H.-E. Kim, and J. Song, "Hydroxyapatite (HA)/poly-l-lactic acid (PLLA) dual coating on magnesium alloy under deformation for biomedical applications," *J. Mater. Sci. Mater. Med.*, vol. 27, no. 2, p. 34, 2016.
- [102] P. Boodagh, D.-J. Guo, N. Nagiah, and W. Tan, "Evaluation of electrospun PLLA/PEGDMA polymer coatings for vascular stent material," *J. Biomater. Sci. Polym. Ed.*, vol. 27, no. 11, pp. 1086–1099, 2016.

- [103] W. Kowalski, M. Dammer, F. Bakczewitz, K.-P. Schmitz, N. Grabow, and O. Kessler, "In-situ investigation of stress conditions during expansion of bare metal stents and PLLA-coated stents using the XRD $\sin 2\psi$ -technique," *J. Mech. Behav. Biomed. Mater.*, vol. 49, pp. 23–29, 2015.
- [104] M. Guo, D. Huang, Z. Dai, X. Xu, and W. Chen, "PLGA(PTX)/PLLA/MAO Coating on the Surface of AZ81 Magnesium Alloy Stent Materials," *Rare Met. Mater. Eng.*, vol. 44(2), pp. 412–418, 2015.
- [105] Z. Wei, P. Tian, X. Liu, and B. Zhou, "In vitro degradation, hemolysis, and cytocompatibility of PEO/PLLA composite coating on biodegradable AZ31 alloy," *J. Biomed. Mater. Res. Part B Appl. Biomater.*, vol. 103, no. 2, pp. 342–354, 2015.
- [106] Z. Wei, P. Tian, X. Liu, and B. Zhou, "Hemocompatibility and selective cell fate of polydopamine-assisted heparinized PEO/PLLA composite coating on biodegradable AZ31 alloy," *Colloids Surfaces B Biointerfaces*, vol. 121, pp. 451–460, 2014.
- [107] P. Lu, M. Fang, L. Cao, and X. Xu, "Research of MAO/PLLA Composite Coating on Different Magnesium Alloy Stent Materials," *Rare Met. Mater. Eng.*, vol. 40(12), pp. 2232–2235, 2011.
- [108] M. Guo, L. Cao, P. Lu, Y. Liu, and X. Xu, "Anticorrosion and cytocompatibility behavior of MAO/PLLA modified magnesium alloy WE42," *J. Mater. Sci. Mater. Med.*, vol. 22, no. 7, pp. 1735–1740, 2011.
- [109] P. Lu, L. Cao, Y. Liu, X. Xu, and X. Wu, "Evaluation of magnesium ions release, biocorrosion, and hemocompatibility of MAO/PLLA-modified magnesium alloy WE42," *J. Biomed. Mater. Res. Part B Appl. Biomater.*, vol. 96B, no. 1, pp. 101–109, 2011.
- [110] S. K. Sudheer, S. Prathibha, D. Kothwala, C. Engineer, A. Raval, A. B. Jerriwala, and H. Kotadia, "Laser Raman spectroscopic investigations of biodegradable vehicle of active agents eluting LVM 316 stainless steel cardiovascular stents for in vivo degradation characteristics," *J. Raman Spectrosc.*, 2009.
- [111] G.-X. Wang, T.-Y. Yin, L.-L. Luo, Y.-B. Hou, Y.-Z. Wang, C.-G. Ruan, R. P. Guzman, and R. Guidoin, "Eluting characteristics of a platelet glycoprotein receptor antibody using a PLLA-coated stent," *J. Biomater. Sci. Polym. Ed.*, vol. 19, no. 3, pp. 359–371, 2008.
- [112] F. Boccafoschi, L. Fusaro, and M. Cannas, "Immobilization of peptides on cardiovascular stent," in *Functionalised Cardiovascular Stents*, Elsevier, pp. 305–318, 2018.
- [113] K. Subramani and W. Ahmed, "Fabrication of PEG Hydrogel Micropatterns by Soft-Photolithography and PEG Hydrogel as Guided Bone Regeneration Membrane in Dental Implantology," in *Emerging Nanotechnologies in Dentistry*, Elsevier, pp. 171–187, 2012.
- [114] S. J. P. McInnes and N. H. Voelcker, "Porous silicon–polymer composites for cell culture and tissue engineering applications," in *Porous Silicon for Biomedical Applications*, Elsevier, pp. 420–469, 2014.

- [115] T. Van Schaftingen, C. Le Pen, H. Terryn, and F. Hörzenberger, "Investigation of the barrier properties of silanes on cold rolled steel," *Electrochim. Acta*, vol. 49, no. 17–18, pp. 2997–3004, 2004.
- [116] B. D. Ratner and A. S. Hoffman, "Physicochemical Surface Modification of Materials Used in Medicine," in *Biomaterials Science*, Elsevier, pp. 259–276, 2013.
- [117] W. J. van Ooij, D. Zhu, M. Stacy, A. Seth, T. Mugada, J. Gandhi, and P. Puomi, "Corrosion protection properties of organofunctional silanes — An overview," *Tsinghua Sci. Technol.*, vol. 10, no. 6, pp. 639–664, 2005.
- [118] M. D. Tyona, "A theoretical study on spin coating technique," *Adv. Mater. Res.*, vol. 2, no. 4, pp. 195–208, 2013.
- [119] S. L. Hellstrom, "Basic Models of Spin Coating," *Stanford University*, 2007. [Online]. Available: <http://large.stanford.edu/courses/2007/ph210/hellstrom1/>. [Accessed: 02-Jul-2020].
- [120] Y. Lang, *Materials Characterization - Introduction to Microscopic and Spectroscopic Methods*. Hong Kong University of Science and Technology: JohnWiley & Sons (Asia) Pte Ltd, 2008.
- [121] "ISO 4287- Geometrical Product Specifications (GPS). Surface texture: Profile method. Terms, definitions and surface texture parameters," 1997.
- [122] B. Bhushan, "Surface Roughness Analysis and Measurement Techniques," in *Modern Tribology Handbook*, ch. 2, 1 st. ed., 2001.
- [123] Mitutoyo America Corporation, "Quick guide to surface roughness measurement," vol. 2229. USA, 2016.
- [124] E. S. Gadelmawla, M. M. Koura, T. M. A. Maksoud, I. M. Elewa, and H. H. Soliman, "Roughness parameters," *J. Mater. Process. Technol.*, vol. 123, no. 1, pp. 133–145, 2002.
- [125] A. International, "ASTM D3359: Standard Test Methods for Rating Adhesion by Tape Test." West Conshohocken, PA, 2017.
- [126] K. Tsujii, "Wetting and Surface Characterization," in *Cosmetic Science and Technology*, Elsevier, , pp. 373–388, 2017.
- [127] DataPhysics Instruments GmbH, "Determination of the surface energy of a solid." [Online]. Available: www.dataphysics-instruments.com. [Accessed: 27-Aug-2020].
- [128] P. Gabbott, "A Practical Introduction to Differential Scanning Calorimetry," in *Principles and Applications of Thermal Analysis*, Oxford, UK: Blackwell Publishing Ltd, pp. 1–50, 2008.
- [129] Hitachi High-Tech Corporation, "Principle of Differential Scanning Calorimetry (DSC)," 2020. [Online]. Available: www.hitachi-hightech.com. [Accessed: 22-Oct-2020].
- [130] B. Schumacher, H.-G. Bach, P. Spitzer, and J. Obrzut, "Electrical Properties," in *Springer Handbook of Materials Measurement Methods*, Berlin, Heidelberg: Springer Berlin Heidelberg, pp. 431–484, 2006.

- [131] NanoScience, “Atomic Force Microscopy.” [Online]. Available: <https://www.nanoscience.com/techniques/atomic-force-microscopy/>. [Accessed: 10-Jul-2020].
- [132] Park Systems, “Park AFM Modes and Techniques.” [Online]. Available: <https://parksystems.com/park-afm-modes>. [Accessed: 10-Jul-2020].
- [133] E. Soergel, “Piezoresponse force microscopy (PFM),” *J. Phys. D. Appl. Phys.*, vol. 44, no. 46, p. 464003, 2011.
- [134] T. F. Scientific, “PrestoBlue™ Cell Viability Reagent,” *Prod. Inf. sheet*, no. Pub. No. MAN0018370 Rev. B.0, 2019.
- [135] Thermo Fisher Scientific, “StemPro® Osteogenesis Differentiation Kit,” *Prod. Inf. sheet*, 2014.
- [136] C. A. Gregory, W. Grady Gunn, A. Peister, and D. J. Prockop, “An Alizarin red-based assay of mineralization by adherent cells in culture: comparison with cetylpyridinium chloride extraction,” *Anal. Biochem.*, vol. 329, no. 1, pp. 77–84, 2004.
- [137] Utah State University, “Biological Sample Fixation for SEM,” 2019.
- [138] P. A. Gerakines, W. A. Schutte, J. M. Greenberg, and E. F. van Dishoeck, “The infrared band strengths of H₂O, CO and CO₂ in laboratory simulations of astrophysical ice mixtures,” *Astron. Astrophys.*, vol. 295, pp. 810–818, 1995.
- [139] E. Thangaraju, N. T. Srinivasan, R. Kumar, P. K. Sehgal, and S. Rajiv, “Fabrication of electrospun Poly L-lactide and Curcumin loaded Poly L-lactide nanofibers for drug delivery,” *Fibers Polym.*, vol. 13, no. 7, pp. 823–830, Sep. 2012.
- [140] N. B. Barroca, “Electromechanically active Poly (L-lactic) acid based structures for regenerative medicine,” Doctoral thesis, Universidade de Aveiro, 2014.
- [141] “PDF Card - Fe - 04-014-0264.”
- [142] “PDF Card - (C₃ H₅ O₃)n - 00-054-1917.”
- [143] M. C. Righetti, M. Gazzano, N. Delpouve, and A. Saiter, “Contribution of the rigid amorphous fraction to physical ageing of semi-crystalline PLLA,” *Polymer (Guildf.)*, vol. 125, pp. 241–253, 2017.
- [144] F. Zou, F. Z. Lu, X. S. Ma, D. W. He, T. T. Tang, X. L. Xia, J. Y. Jiang, and Y. F. Niu, “Cell orientation, proliferation, and differentiation on poly(L-lactide) spherulites,” *RSC Adv.*, vol. 6, no. 62, pp. 57396–57402, 2016.
- [145] SACOME, “How to avoid intergranular corrosion?,” 2017. [Online]. Available: www.sacome.com. [Accessed: 15-Oct-2020].
- [146] M. Tomanik, M. Kobielarz, J. Filipiak, M. Szymonowicz, A. Rusak, K. Mroczkowska, A. Antończak, and C. Pezowicz, “Laser Texturing as a Way of Influencing the Micromechanical and Biological Properties of the Poly(L-Lactide) Surface,” *Materials (Basel)*, vol. 13, no. 17, p. 3786, 2020.
- [147] C. Ribeiro, V. Sencadas, A. C. Areias, F. M. Gama, and S. Lanceros-Méndez, “Surface roughness dependent osteoblast and fibroblast response on poly(L-lactide) films and electrospun membranes,” *J. Biomed. Mater. Res. Part A*, vol. 103, no. 7,

- pp. 2260–2268, 2015.
- [148] L. Xu and A. Yamamoto, “Characteristics and cytocompatibility of biodegradable polymer film on magnesium by spin coating,” *Colloids Surfaces B Biointerfaces*, vol. 93, pp. 67–74, 2012.
- [149] Y.-Q. Wang and J.-Y. Cai, “Enhanced cell affinity of poly(l-lactic acid) modified by base hydrolysis: Wettability and surface roughness at nanometer scale,” *Curr. Appl. Phys.*, vol. 7, pp. e108–e111, 2007.
- [150] A. J. Kinloch, *Adhesion and Adhesives*. Dordrecht: Springer Netherlands, 1987.
- [151] M. H. Gutierrez-Villarreal, F. J. Rodríguez-Gonzalez, and Y. Perera-Mercado, “Estimation of Surface Free Energy of Poly(lactic acid) During UV-Grafting with N-Vinylpyrrolidone,” *Macromol. Symp.*, vol. 374, no. 1, p. 1600130, 2017.
- [152] M. M. Gentleman and E. Gentleman, “The role of surface free energy in osteoblast–biomaterial interactions,” *Int. Mater. Rev.*, vol. 59, no. 8, pp. 417–429, 2014.
- [153] M. C. Righetti, M. Gazzano, M. L. Di Lorenzo, and R. Androsch, “Enthalpy of melting of α' - and α -crystals of poly(l-lactic acid),” *Eur. Polym. J.*, vol. 70, pp. 215–220, 2015.
- [154] P. Melo, “Electromechanical Poly(L-lactic acid) (PLLA) platforms for regenerative medicine,” Master's thesis, Universidade de Aveiro, 2014.
- [155] T.-W. Shyr, H.-C. Ko, T.-M. Wu, and T.-M. Wu, “Crystallisation and spherulite morphology of polylactide stereocomplex,” *Polym. Int.*, vol. 68, no. 1, pp. 141–150, 2019.
- [156] H. Cui and P. J. Sinko, “The role of crystallinity on differential attachment/proliferation of osteoblasts and fibroblasts on poly (caprolactone-co-glycolide) polymeric surfaces,” *Front. Mater. Sci.*, vol. 6, no. 1, pp. 47–59, 2012.
- [157] Z. Ahmad, “Polymer Dielectric Materials,” in *Dielectric Material*, InTech, 2012.
- [158] D. J. Bhagat and G. R. Dhokane, “Ac conductivity investigation of polyindole/poly(vinyl acetate) composites,” *J. Mater. Sci. Mater. Electron.*, vol. 27, no. 11, pp. 11790–11797, 2016.
- [159] C. Dichtl, P. Sippel, and S. Krohns, “Dielectric Properties of 3D Printed Polylactic Acid,” *Adv. Mater. Sci. Eng.*, vol. 2017, pp. 1–10, 2017.
- [160] S. Hikosaka, H. Ishikawa, and Y. Ohki, “Effects of crystallinity on dielectric properties of poly(L-lactide),” *Electron. Commun. Japan*, vol. 94, no. 7, pp. 1–8, 2011.
- [161] Y. Kikkawa, H. Abe, M. Fujita, T. Iwata, Y. Inoue, and Y. Doi, “Crystal Growth in Poly(L-lactide) Thin Film Revealed by in situ Atomic Force Microscopy,” *Macromol. Chem. Phys.*, vol. 204, no. 15, pp. 1822–1831, 2003.
- [162] L.-Z. Cheong, W. Zhao, S. Song, and C. Shen, “Lab on a tip: Applications of functional atomic force microscopy for the study of electrical properties in biology,” *Acta Biomater.*, vol. 99, pp. 33–52, 2019.
- [163] F. Bernard, L. Gimeno, B. Viala, B. Gusarov, and O. Cugat, “Direct Piezoelectric

Coefficient Measurements of PVDF and PLLA under Controlled Strain and Stress,” *Proceedings*, vol. 1, no. 4, p. 335, 2017.

APPENDICES

APPENDICES

Appendix A: Citocompatibility test protocols

Cell culture and maintenance

Human Dental Pulp stem/stromal cells (hDPSCs) obtained from AllCells, LLC (Cat. DP0037F, Lot N° DPSC090411-01) are maintained in MEM α , GlutaMAX™ Supplement, no nucleosides (Gibco, 32561029), supplemented with 10 % (v/v) fetal bovine serum (FBS) (Gibco, A3160802), 100 IU/ml penicillin, 0.1 mg/ml streptomycin (Gibco, 15140122), 2.05 μ m/ml amphotericin B (Gibco, 15290026) and 10 mM HEPES buffer solution (Gibco, 15630122).

Presto Blue™ viability assay

Cells were seeded over the biomaterials at a density of 7000 cells per cm² in a non-adherent 24 well plate, in a low volume suspension (50-100 μ L), allowing them to adhere to the biomaterial and not to the well bottom. After 60 minutes of incubation, seeded wells were concealed with complete medium and incubated overnight at 37 °C, 80 % humidified atmosphere and 5 % CO₂ environment. An adherent 24 well plate was considered for the positive control group.

The culture medium was removed from each well at every time-point (24, 72, 120, and 168 hours) and replaced by fresh complete medium, with 10 % (v/v) of 10x Presto Blue™ cell viability reagent (Invitrogen, A13262). Cells were incubated for 60 minutes at 37°C, 80 % humidified atmosphere, and 5 % CO₂ environment. The supernatant medium was collected and transferred to a 96 well plate and absorbance was read at 570 and 595 nm, which are the excitation and emission wavelength of the Presto Blue™ reagent, respectively. Wells were washed with Dulbecco's phosphate-buffered saline solution (DPBS, Gibco, 14190169) until Presto Blue™ residues were removed and fresh culture medium was added to each well. Absorbance values were measured in triplicate, using a Multiskan™ FC Microplate Photometer (Thermo Scientific™, 51119000). For each well, it was subtracted the absorbance at 595 nm from the absorbance at 570 nm. The average of control well values was calculated. Corrected absorbance was obtained by subtracting the average of the control wells to each experimental well.

Osteogenic differentiation assay

Cells were seeded over the biomaterials and incubated same to the viability assay. After 3 days, the cell wells reached 80 % confluency and, at this point, differentiated wells cells were transitioned to a formulated Osteogenesis media (StemPro™ Osteogenesis Differentiation Kit, Gibco A1007201). Undifferentiated wells were maintained in culture media absent on osteogenic supplements. Media was changed every 3 days, after 21 days, the culture medium from each well was removed and the Alizarin Red S (ARS) assay was employed.

The cells were washed with 1 x PBS, fixed in 4 % formaldehyde, and washed with diH₂O. After diH₂O remotion, the ARS dye was added into the wells and incubated at room temperature for 20 - 30 min with shaking. The dye was removed and the cells were washed with diH₂O again. A 10 % acid acetic solution was added to each well and incubated at room temperature for 30 minutes with shaking. The cells were collected and transferred to a microcentrifuge tube. After vortexing for 30 s, the slurry was overlaid with mineral oil, heated to 85 °C for 10 min, and transferred to the ice for 5 min. The slurry was centrifuged for 15min and the supernatant was removed to a new microcentrifuge tube. A solution of 10 % (v/v) ammonium hydroxide was added to neutralize the acid. Solutions with different concentration of ARS was prepared and the absorbance was read in triplicate at 405 nm with a plate reader. The average of replicate wells was calculated and the blank value was subtracted from the others. A standard curve was created by plotting absorbance (405 nm) as a function of ARS concentration and the ARS concentration in the samples was calculated according to the equation of the trend line.

Biological Sample Fixation for SEM

The samples were fixed with 2 % buffered glutaraldehyde overnight, later, they were rinsed with 0.1 M HEPES buffer 3 times for 5 min each with agitation. They were dehydrated with 50 %, 70 %, 95 %, and 100 % ethanol solution twice for 10 min with agitation, except for the 100 % solution that was realized 3 times for 15 minutes. Then the samples were dried using a critical point dryer or chemical drying, and let in a fume hood overnight to evaporate the HMDS. Finally, the samples were sputter-coated with Au/Pd and imaging.

Appendix B: Surface roughness results

Table: Surface roughness results.

Sample	Measure	Ra (μm)	Rz (μm)
SS316L	X ₁	0.13	1.00
	X ₂	0.15	1.20
	X ₃	0.20	1.30
	μ (μm)	0.16	1.17
	σ (μm)	0.04	0.15
SS316L TT	X ₁	0.32	1.90
	X ₂	0.30	1.90
	X ₃	0.30	1.80
	μ (μm)	0.31	1.87
	σ (μm)	0.01	0.06
SS316L TT/SIL	X ₁	0.32	1.90
	X ₂	0.32	2.10
	X ₃	0.31	1.90
	μ (μm)	0.32	1.97
	σ (μm)	0.01	0.12
SS316L TT/SIL/PLLA	X ₁	0.13	0.90
	X ₂	0.12	1.00
	X ₃	0.14	0.90
	μ (μm)	0.13	0.93
	σ (μm)	0.01	0.06

Table: Film thickness measures.

Sample	Measure	Rmax(μm)
SS316L TT/SIL/PLLA without a piece of film	1	4.20
	2	3.70
	3	5.20
	4	6.70
	5	4.10
	μ (μm)	4.78
	σ (μm)	1.21

Appendix C: Contact angles results

Table: Contact angles of the SS316L TT/SIL/PLLA samples with water and diiodomethane drops.

Liquid	Contact angle (°)	Mean (°)	Deviation (°)
Water	86.73	83.48	1.94
	85.81		
	84.72		
	81.67		
	81.59		
	83.37		
	82.03		
	84.54		
	83.33		
	81.00		
Diiodomethane	33.73	40.03	6.43
	51.16		
	50.88		
	41.39		
	41.74		
	34.53		
	37.11		
	38.94		
	34.08		
	36.73		